Multi-Scale Design and Optimization of Microstructures under Uncertainties

by

Pınar Acar

A dissertation submitted in partial fulfillment
of the requirements for the degree of
Doctor of Philosophy
(Aerospace Engineering)
in The University of Michigan
2017

Doctoral Committee:

Professor Veera Sundararaghavan, Chair
Professor John E. Allison
Professor Daniel J. Inman
Professor Anthony M. Waas

Pınar Acar

acarp@umich.edu

ORCID iD: 0000-0002-5911-0410

To my family

ACKNOWLEDGEMENTS

Receiving my doctoral degree is for sure one of the top most important milestones in my career and life, and it is a great pleasure to express my sincere appreciation to the people who make this accomplishment possible with their continuous support. I am very grateful to have had the opportunity to work with Professor Veera Sundararaghavan, who is an inspiring research advisor not only because of his academic excellence but also because of his patience, positiveness, support, and humbleness. He always encourages new research ideas and his guidance plays a key role to make them happen since he provides you all the means to improve and enjoy your work.

I have been very privileged to have Professor Anthony M. Waas, Professor Daniel J. Inman and Professor John E. Allison on my dissertation committee. I am endlessly grateful for their invaluable advice and support on my dissertation work and career. I cannot thank Professor Anthony M. Waas enough for his academic encouragement, insight and guidance. I am very thankful to Professor Daniel J. Inman for his patience, wisdom and understanding. My work benefitted a lot from my collaboration with Professor John E. Allison and his research group on the ONR project. I owe a lot to his leadership and vision. This journey would not have been the same without my advisor and committee members. Last but not least, I would like to express my deep appreciation to Professor Melike Nikbay, who was my M.Sc. advisor in Istanbul Technical University, for encouraging me to chase my dream of an academic career.

I cannot think of an achievement without the endless love and support of my family: my mother, my father, my sister, my nephew and my baby niece. I dedicate

my dissertation to them in appreciation for all their love. I am perfectly fortunate to have friends who have been my family here and back in Turkey. Words are not enough to thank my roomie-dodi, Doğa, with all my heart for her boundless sacrifice, sincerity, love, support, and companionship over the years. This whole experience would definitely have not been as pleasant as today if I was not lucky enough to come here with her. One of my greatest privileges in life is to have my high school friends, Hazal, Selin, Tuğçe, Halime, Gözde, Hilal, who have continuously been touching my life with their true friendship over 15 years. I deeply appreciate the love, support and the positive energy they have been sending me everyday no matter what the physical distances are.

Life has given me the opportunity to make true friends at different time stages and different places. What is good here is to be able to maintain these solid friendships despite the years and despite the distances. I am very thankful to my friends, Elgiz and Memot, for their devotion. Ann Arbor is also the place where I have made friends for life. I would like to sincerely thank these friends, Avin and Setsuko, for their cordiality and whole hearted support. It is a pleasure to express my gratitude to my dear friends, Devina, Kyle, Merve, Emre, Katie, Doreen, Ece, Söğüt, Remzican, Büke, Yuki and Gamze, for all the good memories we have had together. I am also thankful to my friends and teammates, Adam, Nick, Jiangyi, Arunabha, Aaditya, Sriram, Siddhartha, Ali and Shardul, and to my past/current officemates, Abhishek, Moritz and Gustavo.

I really appreciate the financial support I received through AFOSR MURI and ONR projects I have worked on. Owing to these projects, I had the opportunity of collaborating with many talented researchers. Some portion of the presented work in this dissertation is a product of these fruitful collaborations. I would like to thank Dr. Anna Trump and Dr. Zhe Chen for providing me experimental data, Dr. Sriram Ganesan for performing the crystal plasticity finite element simulations, and Dr.

Arunabha M. Roy for performing the phase field simulations. I also thank University of Michigan Rackham Graduate School for providing me Rackham Fellowship during the first year of my doctoral studies, and TUBITAK (The Scientific and Technological Research Council of Turkey) for providing me financial support during my graduate studies in Turkey. Moreover, I would like to express my sincere gratitude to Zonta International for awarding me with the prestigious Amelia Earhart Fellowship, and to Zonta International District 15 and Zonta Club of Ann Arbor-Washtenaw members for their support. I feel dignified for having such a role to represent the female scientists/engineers in academia.

TABLE OF CONTENTS

DEDICATION ii

ACKNOWLEDGEMENTS iii

LIST OF FIGURES ix

LIST OF TABLES xii

ABSTRACT xiii

CHAPTER

1. Introduction 1

1.1 Multi-scale design and optimization of materials and deformation processes 4
1.2 Quantification of microstructural uncertainties and stochastic design optimization of materials 7

2. Microstructure Modeling with Orientation Distribution Function 13

2.1 Multi-scale modeling of microstructures 14
2.1.1 Introduction to the ODF approach 16
2.1.2 Probability update 19
2.1.3 Constitutive model 21
2.2 Optimization for slip system parameters identification of Ti-Al alloys 22
2.2.1 Optimization of slip system parameters for Ti-0Al . 23
2.2.2 Optimization of slip system parameters for Ti-7Al . 27
2.2.3 CPFE analysis for Ti-7Al 30
2.3 Conclusion 32

3. Multi-Scale Design and Optimization of Microstructures . . 34

3.1 Multi-scale design optimization methodology 36
3.1.1 Design optimization problem 36
3.1.2 Generation of property closure 38
3.1.3 Utilization of a direct linear solver to identify infinite solutions 40
3.2 Applications 41
3.2.1 Thermal buckling of Titanium aircraft panels 41
3.2.2 Vibration tuning for Galfenol beam 48
3.3 Conclusion 52

4. Uncertainty Quantification for Microstructural Variations . . 56

4.1 Quantification of experimental uncertainties 57
4.1.1 Uncertainties in PF data 58
4.1.2 Uncertainties in EBSD data 62
4.2 Analytical modeling for UQ 65
4.2.1 General features of Gaussian distributed correlated random variables 67
4.2.2 UQ in ODF values using Gaussian distributed correlated variables 68
4.2.3 UQ in linear properties using Gaussian distributed correlated variables 70
4.2.4 UQ in nonlinear properties using transformation of random variables 70
4.3 UQ in microstructural parameters and material properties . . 72
4.3.1 Quantification and propagation of experimental uncertainties using PF data 72
4.3.2 Quantification and propagation of experimental uncertainties using EBSD data 76
4.4 Conclusion 79

5. Stochastic Design Optimization of Microstructures 82

5.1 Stochastic design optimization for the Galfenol beam with uncorrelated ODFs 85
5.1.1 LP approach for inverse design 85
5.1.2 Definition of the stochastic optimization problem . . 89
5.1.3 Results 90
5.2 Stochastic design optimization with correlated ODFs 94
5.2.1 LP problem derivation 95
5.2.2 Optimization problem and results 99
5.3 Conclusion 101

6. Process-Texture-Property Identification 104

6.1 Reduced order model of the ODF . . . 105
6.2 LP problem formulation for optimum deformation process identification . . . 110
6.2.1 Identification of the ODFs closest to an optimum ODF in the material plane . . . 110
6.2.2 Identification of the ODFs to obtain material properties closest to a desired set of properties . . . 114
6.3 Results . . . 117
6.3.1 Results for the closest ODF identification problem . 117
6.3.2 Results for the closest material properties identification problem . . . 120
6.4 Conclusion . . . 121

7. Future Directions on Multi-Scale Modeling of Microstructures 124

7.1 Higher order probabilistic features and multi-fidelity design approach . . . 127
7.1.1 Cylindirical grains . . . 130
7.1.2 Discussion . . . 130
7.2 Multi-scale modeling of composite materials . . . 134

BIBLIOGRAPHY . . . 136

LIST OF FIGURES

FIGURE

2.1 ODF representation in the Rodrigues fundamental region for hexagonal crystal symmetry showing the location of the k=50 independent nodes of the ODF in red color . . . 17
2.2 True strain-true stress curve comparison of experimental data and optimum design for Ti-0Al . . . 24
2.3 $< 002 >$ and $< 100 >$ PFs at 9% compressive strain (Experimental data is given by Fitzner [50]) . . . 25
2.4 Sensitivity analysis results for optimum design parameters of Ti-0Al 26
2.5 True strain-true stress curve comparison of experimental data and optimum design for Ti-7Al . . . 28
2.6 Comparison of Ti-7Al microstructures at 20% compressive strain . . 28
2.7 $< 001 >$, $< 100 >$ and $< 101 >$ PFs at 20% compressive strain . . . 29
2.8 Sensitivity analysis results for optimum design parameters of Ti-7Al 30
2.9 CPFE simulation and DIC data comparison for e_{xx} strain field . . . 31
2.10 CPFE simulation and DIC data comparison for e_{yy} strain field . . . 31
2.11 CPFE simulation and DIC data comparison for e_{xy} strain field . . . 32
2.12 Single crystal properties for stiffness, thermal expansion and yield stress of α-Ti . . . 33
3.1 Flowchart for multi-scale design optimization of materials . . . 35
3.2 Microstructure of high temperature materials . . . 42
3.3 Representation of the analytical buckling problem . . . 43
3.4 Property closures of HCP α-Ti thermal buckling problem . . . 46
3.5 Optimum ODF representation for the thermal buckling problem . . 47
3.6 Geometric representation of Galfenol beam vibration problem . . . 49
3.7 Property closure for E_1 and G_{12} . . . 53
3.8 Some of the multiple optimum designs for the vibration tuning problem 54
4.1 Representative $< 001 >$, $< 100 >$ and $< 101 >$ PF samples . . . 59
4.2 Probability histograms of a few representative pole density values ($P(\boldsymbol{h}, y_i)$). The labels for PF1, PF2 and PF3 indicate the PFs $\boldsymbol{h} =< 001 >, < 010 >$ and $< 101 >$ respectively from which these densities are obtained. . . . 60
4.3 Mean values of the PFs . . . 60

4.4 Coefficient of variations for the PFs . . . 61
4.5 Some example EBSD samples . . . 64
4.6 The ODFs at the integration points agree with the Gaussian distribution . . . 65
4.7 The skewness of the integration point ODF variations. . . . 65
4.8 The P-P and Q-Q plots of the experimental samples and Gaussian assumption . . . 66
4.9 The solution procedure for UQ using EBSD sample data . . . 66
4.10 Probability histograms of the ODFs . . . 73
4.11 Statistical features of the ODF probability distributions . . . 74
4.12 Probability histograms of S_{11} and S_{66} . . . 75
4.13 Probability histograms of E_1 and G_{12} . . . 75
4.14 Probability histograms of the ODFs . . . 77
4.15 Statistical features of the ODF probability distributions . . . 78
4.16 Probability histograms of S_{11}, S_{66}, E_1, G_{12}, ω_{1t} and ω_{1b} . . . 79
5.1 The stochastic optimization scheme for the Galfenol beam vibration tuning problem . . . 83
5.2 The variations of yield stress and vibration frequencies of the stochastic optimum designs . . . 92
5.3 Examples for multiple optimum microstructures of the stochastic optimization problem . . . 93
5.4 Yield stress distributions of the optimum microstructure design with varying z values in the analytical solution . . . 94
5.5 Comparison of ODF mean values with random texture . . . 100
5.6 Yield stress distributions of the optimum microstructure design with varying z values in the analytical solution . . . 100
6.1 Optimum deformation process identification as an LP problem . . . 106
6.2 Basis functions of different deformation processes . . . 108
6.3 Property closures of different deformation processes . . . 109
6.4 Optimum microstructures on process planes identified with ODF matching approach . . . 119
6.5 Optimum microstructures on process planes identified with property matching approach . . . 122
7.1 A representative EBSD plot for the LENS microstructure [98] . . . 128
7.2 The NNOCF sampling from a microstructure (color coded based on grain orientation). The FE mesh M_g represents the volume density of each orientation (color). The volume density of each orientation (color) is represented by the NNOCF mesh $M_{g'|gr}$ attached to a node g in mesh M_g for the nearest neighbor pixels of g [99] . . . 129
7.3 The ODF representation for the texture evolution of a microstructure with cylindrical grains during phase field simulation . . . 131
7.4 The NNOCF representation for the texture evolution of a microstructure with cylindrical grains during phase field simulation (only the cross-diagonal terms in the NNOCF matrix) . . . 131

7.5 The stress-strain curves predicted using the ODF, NNOCF and FE representations 132
7.6 Multi-scale design of nano-composites 135

LIST OF TABLES

TABLE

2.1 Optimum slip system parameters of Ti-0Al 24
2.2 Optimum slip system parameters of Ti-7Al 27
2.3 CRSS values of different slip systems in Ti-7Al 28
3.1 Results for a simply supported rectangular HCP α-Ti plate 47
3.2 Computational time comparison for linear solver and global optimization approaches 48
3.3 Optimization results of vibration tuning problem for the Galfenol beam 53
5.1 Stochastic optimization results for vibration tuning of the Galfenol beam 91
6.1 LP problem results for ODF matching on material and process planes 118
6.2 LP Problem results for desired properties matching on material and process planes 120

ABSTRACT

Research on computational modeling and multi-scale design of materials has been garnering a lot of interest due to the demand for high performance materials in electronics, energy and structural applications. The primary goal of the present study is to develop a new computational approach for microstructure design for achieving a set of material properties within a designated level of uncertainty. This thesis combines the methods of uncertainty quantification (UQ) and materials design, using a unique linearization approach that is well-suited for metallic materials modeled using probabilistic descriptors such as the orientation distribution function. An analytical UQ formulation is proposed to model the uncertainties in microstructural features from experimental (electron diffraction) data as well as for inverse modeling the uncertainties in optimal microstructural features from property data. Compared to the widely preferred computational UQ algorithms the analytical model reduces the required computational time significantly as well as capturing the effect of stochasticity in microstructure design accurately. The optimal processing route, which produces materials with optimized texture and/or properties, is identified by developing reduced order models to represent the texture evolution. Examples presented include the performance improvement of Titanium aircraft panels for thermal buckling, and optimization of Fe-Ga alloys for vibration response and identification of optimal processing route for Fe-Ga alloy microstructures.

CHAPTER 1

Introduction

Material selection has been traditionally used by engineers for engineering design, as exemplified by property cross-plots (popularized by Ashby [1]), a graphical representation of material–property–performance relationships. For example, density versus strength plot of different materials can be used by an aircraft engineer to find that for the same strength requirement, a titanium alloy weighs much less than a steel alloy. However, even within the selected alloy system, it is common knowledge that microstructural variability leads to a large range of material properties. Microstructure has a substantial effect on the performance of critical components in numerous aerospace applications. Example applications that benefit from microstructure design include high temperature panels in airframes, turbine disks and active materials for vibration sensing. We are currently moving towards a new paradigm of Integrated Computational Materials Engineering (ICME), where microstructure optimization will become an integral part of engineering design.

Microstructure–sensitive design of polycrystalline alloys can be performed by tailoring the distribution of various crystal orientations ('the orientation distribution function (ODF)') in the microstructure. In general, engineering properties attain extremal properties along different crystallographic directions. For example, in rolled sheets of magnetoelastic alloy Galfenol ($Fe_{100-x}Ga_x$), the highest yield strength oc-

curs in the (111)[110] orientation, highest elastic modulus occurs in the (110)[111] orientation while both magnetization and magnetostriction are highest in the (100)[001] orientation. Sensors or actuators in the form of compliant beams of Galfenol give the highest energy density if magnetostriction and strength are maximized while minimizing the elastic modulus. Thus, to optimize a composite measure of these properties, one may need to design a polycrystal with different volume fractions of critical crystal orientations.

This task is challenging due to the high dimensionality of the space of all possible crystal orientation distributions. Very few published works in literature discuss such design problems. Significant contributions in this area include [2] where the authors design an ODF that maximizes the deflection of a beam without plastically deforming it. In [3], the authors design a plate with a circular hole subjected to an in-plane tensile load so as to maximize the load carrying capacity while avoiding plastic deformation. These analyses employ a reduced spectral series representation of the texture that significantly reduces the dimensionality of the search space. Spectral representations are global approximations of the ODF and are not optimal for capturing sharp features (e.g. single crystals). In this thesis, we employ a reduced order model (ROM) representation based on finite element (FE) discretization of the orientation space, that is able to capture sharp features due to the use of a local basis. The ROM representations are integrated to an optimizer, and the numerical framework is capable of identifying the optimum ODFs which satisfy the design criteria for engineering properties.

Traditional optimization techniques such as gradient methods lead to a unique or a small set of microstructural solutions rather than the complete space of optimal microstructures. Multiple solutions are favored in the sense that traditional low–cost manufacturing processes such as forming and heat treatment can only generate a limited set of microstructures, and the identified optimal microstructure(s)

may not be economically feasible to manufacture. In this study, a novel computational methodology is developed that better addresses the issues of non–uniqueness of microstructure–property relationships.

Robust engineering designs take into account property variability that naturally occurs due to microstructural stochasticity and processing–related uncertainties. Another aspect of this study is to investigate the effect of microstructural uncertainties on uncertainty in material properties by using an uncertainty quantification (UQ) framework. An analytical formulation of multivariate probability distributions is developed for modeling the quantification and propagation of microstructural uncertainties on the microstructure-sensitive properties. Moreover, a stochastic optimization algorithm is implemented that addresses the inverse UQ problem of computing microstructural uncertainties if the property objectives are given in the form of a mean value and a distribution. Such a model can be readily commercialized for the material processing industry.

In summary, this study has contributed to the multi-scale modeling and design of materials literature in the following aspects:

- Development of microstructure–property models using ODF representation for Titanium alloys.
- A multi-scale design methodology to optimize microstructures and enhance the engineering material properties and system performance.
- Identification of multiple optimum microstructure solutions using null space of a linear solver.
- Identification of optimal processing route(s) to manufacture materials with desired texture and/or properties through the implementation of a reduced order modeling scheme.

- Quantification of microstructural uncertainties and modeling their propagation to the material properties.

- Multi-scale design optimization of materials under uncertainties.

The organization of the present study is as follows: Chapter 2 discusses the modeling of microstructures using the probabilistic descriptor based approach to identify the slip system parameters of Ti-Al alloys using the available experimental data. Chapter 3 addresses a multi-scale design optimization methodology for microstructures to enhance the macro engineering material properties. The experimental uncertainties are quantified, and their propagation to the microstructure design and material properties is modeled with an analytical UQ algorithm in Chapter 4. This analytical UQ algorithm is implemented to the multi-scale design optimization framework to identify the optimum microstructure designs under the effect of uncertainties in Chapter 5. Chapter 6 focuses on the identification of optimal processing route to manufacture materials with desired texture and/or properties. The future directions on multi-scale design of materials are discussed in Chapter 7. The multi-scale modeling approach of this study is based on a one-point probability descriptor, ODF. Future work in this area should focus on modeling of microstructures and process design with higher order probabilistic descriptors, such as Nearest Neighbor Orientation Correlation Function (NNOCF), that additionally captures grain neighborhood information, as discussed in Chapter 7.

1.1 Multi-scale design and optimization of materials and deformation processes

Recent developments in materials-by-design have allowed a more advanced systems approach that integrates processing, structure and property through multi-scale computational material models [4]. In the area of composites, techniques that enable

tailoring of microstructure topology have allowed design of structures with interesting extremal properties such as negative thermal expansion [5] and negative Poisson's ratio [6]. In contrast to composites, techniques that allow tailoring of properties of polycrystalline alloys involve tailoring of preferred orientation of crystals manifested as the crystallographic texture. During forming processes, mechanisms such as crystallographic slip and lattice rotation drive the formation of texture and variability in property distributions in such materials. A useful method for designing materials is through control of deformation processes leading to the formation of textures that yield desired property distributions.

The microstructure modeling of the present work is based on the quantification of the microstructure using the ODF. The ODF represents the volume fractions of the crystals of different orientations in the microstructure. The ODF is defined based on a parameterization of the crystal lattice rotation. Popular representations include Euler-angles [7, 8] and classes of angle-axis representations, with the most popular being the Rodrigues parameterization [9]. Conversion of continuous orientation space to finite degrees of freedom for material property optimization requires discretization techniques. Discretization schemes either focus on a global basis (e.g. Fourier space or spherical harmonics [10, 11]) or a local basis using an FE discretized Rodrigues space with polynomial shape functions defined locally over each element [12, 13]. Step one of microstructure optimization problem involves computation of the discretized ODF values that satisfy a given set of desired properties. Liu et. al [14] achieved this by directly sampling the ODF space using a data mining methodology. However, the space of all possible ODFs is high dimensional and sampling in the property space is favorable since the number of design variables is significantly lesser. Kalidindi and coworkers [10, 11, 15] employ sampling within the property hull similar to this work, but employ a Fourier basis for discretizing the ODF. As explained before, Fourier/spectral methods cannot represent sharp textures due to the use of a

global basis. Chapter 2 introduces the ODF based methodology using a local basis [16], and focuses on an inverse problem for crystal plasticity modeling of Ti-Al alloys (Ti-0wt%Al (Ti-0Al) and Ti-7wt%Al (Ti-7Al)) using the technique. The single crystal constitutive model presented by Anand and Kothari [17] is used to model the crystal plasticity of the microstructure, and the ODF evolution is modeled using a conservation equation. The crystal plasticity parameters are computed using an inverse problem. The objective of this design problem is to match the global tensile and compression stress-strain curve behavior, which is known through experiments and the model is validated by comparing against experimentally measured ODFs after compression. Chapter 3 addresses different engineering design problems with various design objectives and constraints. The fundamental goal of this chapter is to identify the best microstructure design, represented by the ODF, to optimize a macro engineering material property. The material properties are computed using the volume averaged equations, which are defined in terms of the ODF values. The optimum ODF solution corresponds to the solution of an optimization problem in a very high-dimensional design space. To increase computational time efficiency the solution space is reduced to a new space, property closure, which is the space of the important material properties of the design problem. The optimization problem can be solved in the property closure since it includes all possible microstructure designs. The optimization problems, which are discussed in Chapter 3, are solved in the property closures to maximize the critical buckling temperature of a Titanium aircraft panel, and maximize the yield stress of a Galfenol (Fe-Ga alloy) cantilever beam while satisfying the design constraints defined for vibration tuning through the first bending and torsion natural frequencies of the beam. After identifying the optimum microstructure design a direct linear solution scheme is also implemented to find the infinite solution directions and multiple optimum designs. The optimization methodology is first applied to the aircraft thermal buckling problem, where the optimum

design corresponds to a unique solution. The multiple optimum designs are identified for the Galfenol beam vibration tuning application. The motivation of Chapter 6 is to find out which of the multiple ODFs identified in Chapter 3 can be manufactured using a deformation process or a set of sequential deformation processes. Li et. al [18] addressed this problem by representing processing paths as streamline functions in the space of spectral coefficients. This allows inversion of processing paths by tracking streamlines connecting the initial and optimal textures. The complexity of the model depends on the number of spectral coefficients used to represent the texture. Since a large number of spectral terms are needed to capture sharp textural features, complexity of the models used to describe processing paths increases accordingly. In this work, textures from a given process are represented by using basis functions that are derived using Proper Orthogonal Decomposition (POD) [19, 20]. The multiple optimum ODFs from step one are projected onto the basis functions of various deformation processes and the optimal process is identified as the one that minimizes the distance between any one of the optimal ODFs and the ODF that can be achieved from a process. A second approach where the optimal property values are projected onto the process basis is also presented.

1.2 Quantification of microstructural uncertainties and stochastic design optimization of materials

The microstructure problems, which are discussed in Chapter 2, Chapter 3 and Chapter 6, model the ODFs as deterministic variables. However, the microstructures are inherently stochastic and therefore it is important to model the effect of uncertainties to the microstructure design and material properties. One of the pillars of ICME (Allison et al. [21]) is UQ, and it involves the development of mathematical tools to quantify the effect of microstructural stochasticity on the predicted engineering prop-

erties. Various sources of the uncertainties in ICME are observed as: variabilities due to processing, operating conditions, randomness of the microstructure, incomplete knowledge of model parameters, inaccurate data, insufficient knowledge about physical process such as process-structure or structure-property relations [22]. In the present study, the aleatoric uncertainties, which stem from the stochastic nature of the microstructures, are quantified using the available experimental data. The microstructural uncertainties arise from imperfections in the manufacturing processes, such as variations in the stress or temperature gradients during forming processes, which are used to make aircraft components such as turbine disks. These imperfections lead to stochasticity both point–to–point within a specimen as well as across multiple specimens that originate from the same manufacturing process. In the UQ parlance, these uncertainties are classified as aleatoric. Electron backscatter diffraction (EBSD) and pole figure (PF) representations are important experimental methods to quantify such microstructural variations. The PF data and multiple EBSD scans on alloy specimens made from the same manufacturing process are employed to sample the various microstructures. The goal in Chapter 4 is to model the propagation of these uncertainties to engineering properties using an analytical approach. The UQ studies in literature in the area of multi-scale structural modeling are sparse [23]. Current state of the art to model the uncertainties in materials involves the use of expensive numerical simulations such as Monte Carlo simulation (MCS), collocation and spectral decomposition methods. Creuziger et. al [24] examined the uncertainties in the ODF values of a microstructure due to the variations in the PF values by using MCS. Juan et. al [25] used MCS to study effects of sampling strategy on the determination of various characteristic microstructure parameters such as grain size distribution and grain topology distribution. Hiriyur et. al [26] studied an extended FE approach, XFEM, coupled with an MCS approach to quantify the uncertainties in the homogenized effective elastic properties of multiphase materials. Saves

and Stefanou [27] modeled the microstructural uncertainties as random variations using the MCS technique. These uncertainties were then linked to the macro-scale parameters through a stochastic FE approach. Kouchmeshky and Zabaras [28] presented propagation of initial texture and deformation process uncertainties on the final product properties using a stochastic collocation approach. The authors addressed an uncertainty problem for a multi-scale closed-die forging deformation process using Karhunen-Loeve expansion and Bezier splines to represent the variations in the initial geometry and texture [29]. Madrid et. al [30] examined the variability and sensitivity of in-plane Young's modulus of thin nickel polycrystalline films due to uncertainties in microstructure geometry, crystallographic texture, and numerical values of single crystal elastic constants by using a numerical spectral technique. Niezgoda et. al [31] computed the variances of the microstructure properties by defining a stochastic process to represent the microstructure. Cai and Mahadevan [32] analyzed the uncertainties in manufacturing processes and their propagation to the microstructure using a Gaussian process surrogate model. Some authors have also focused on the computational techniques to study the uncertainties on microstructural homogenization approaches. Huyse and Maes [33] studied the effect of microstructural uncertainties on homogenized parameters by using random windows from the real microstructure, and performed MCS to identify the stochasticity in material parameters such as Young's modulus and Poisson's ratio. Sakata et. al [34] also showed the variations in Young's modulus and Poisson's ratio due to microscopic uncertainties. They validated the results of their perturbation-based homogenization method with MCS. In another paper, Sakata et. al [35] implemented a Kriging approach to calculate the probability density functions of the material properties, and used MCS to study the uncertainties in geometry and material properties of a microstructure through the same perturbation-based homogenization method. A computational stochastic modeling approach for random microstructure geometry was presented by Clement

et. al [36, 37]. The authors presented a high dimensional problem due to the high number of stochastic variables to represent the microstructure geometry. This high dimensionality was reduced with the implementation of Polynomial Chaos Expansion (PCE). These computational methods presented in literature involve using a numerical algorithm for quantification and propagation of uncertainties. They represent the joint probability distributions of random variables either using interpolation functions or sampling for random points. These techniques are not computationally efficient as the problem complexity or the number of variables increases the number of interpolation terms or sampling points has to increase to maintain the accuracy level. This is especially true for the ODFs, which are discretized using the FE nodes or spectral basis, and contain large number of free parameters whose joint distribution needs to be sampled. Another drawback is the difficulty of satisfying design constraints (such as volume fraction normalization) when using numerical approaches. All these disadvantages imply the necessity of developing analytical solutions as a first step in UQ. Recently, the Gaussian characteristic functions are employed to stochastically model the PF inversion [38]. The approach is fully analytical and significantly faster than the numerical approaches. However, the PF inversion is non-unique, and it leads to the 'epistemic' uncertainty, which stems from the modeling errors or inaccuracies, due to lack of an exact solution. Chapter 4 focuses on the PF to ODF and EBSD to ODF conversions, which are one–to–one maps only constrained by the level of discretization of the ODF, and thus, aleatoric uncertainties can be better quantified. The Gaussian model is employed and the uncertainties in the ODF are analytically propagated to the linear and non-linear properties derived from the ODF. Chapter 5 aims to investigate the effect of aleatoric uncertainties in microstructure modeling and inverse design of stochastic microstructural features to achieve a prescribed statistical range of engineering properties. Current state of the art only addresses the direct UQ problem (effect of uncertain microstructures on properties) and the stochastic inverse

problem has only been addressed in a previous paper of the author [39]. In Chapter 5, the same analytical formulation based on the Gaussian distribution approach presented in Chapter 4 is used to represent the variations of the random parameters. The vibration tuning problem of the Galfenol beam introduced in Chapter 3 is exercised. The variations of in-plane Young's modulus (E_1) and shear modulus (G_{12}) parameters are assumed to be provided by the manufacturer, and consistent with the Gaussian distribution. Then the probability distributions of the ODFs are computed by solving an inverse problem. The variations in the compliance parameters, S_{11} and S_{66}, are found first with the transformation of random variables rule using the input variations in E_1 and G_{12}. The compliance parameters are calculated first since they can be represented with linear equations in terms of the ODFs. The probability distributions of the compliance parameters are also assumed to be modeled with a Gaussian approach despite their nonlinear relation to E_1 and G_{12} since the input uncertainties are very small. Then the inverse problem to find the statistical properties of the ODFs is defined as an LP problem. A global stochastic optimization approach is implemented to this analytical solution framework to maximize the yield stress under vibration tuning constraints defined for the first bending and torsion natural frequencies of the cantilever beam. The optimization variables are defined as the in-plane Young's modulus (E_1) and shear modulus (G_{12}) of the Galfenol material, and each design sample is assumed to have the same level of uncertainty. To the best of the author's knowledge this is the first analytical effort in literature for quantification of microstructural stochasticity given the desired statistical range in properties, in effect, a stochastic inverse problem for microstructure design [39, 40]. The optimization results are also compared to the results of the computational technique, which employs MCS to quantify the uncertainties. The analytical algorithm is able to compute the same optimum values of the variables and a very close objective function value to the MCS solution. It can also decrease the computational time by almost

two orders of magnitude. Once the optimum ODFs are achieved, then the multiple solution directions are identified using the direct linear solver, which is presented in Chapter 3. The effect of uncertainties on the design objective is also discussed at the end by comparing the optimum results with the deterministic solution for maximum yield stress objective.

CHAPTER 2

Microstructure Modeling with Orientation Distribution Function

A multi-scale modeling approach which can link the microstructural features to the macro-scale engineering properties is addressed through the use of a one-point probability descriptor, ODF. Using the ODF model the averaged material properties are computed with a volume averaging approach which implements the linearized equations of the property matrices derived from the single crystal solutions, and the corresponding ODF values. The ODF model is used in this chapter for property prediction of the Titanium-Aluminum (Ti-Al) alloys, Ti-0 weight (wt)%Al (Ti-0Al) and Ti-7wt%Al (Ti-7Al), which are in demand for many aerospace applications. The property studied is the tension and compression response of the materials using crystal plasticity. A rate-independent single-crystal plasticity model developed in Anand and Kothari [17] is used to compute the effect of macroscopic strain on the polycrystal. The optimization problem is defined for calibrating the slip system parameters using the available tension and compression experimental data. Compared to the other alloys, such as Ti-6Al-4V [41, 42, 43], the parameters of Ti-7Al are not studied extensively in literature. Therefore the optimization results for the crystal plasticity model realization produce unique data, which will be beneficial to future studies in the field. The sensitivities of the optimum variables to the design objectives are

also investigated to identify the most critical slip system parameters. The crystal plasticity simulations input a randomly oriented initial texture. Using the optimum design parameters the microstructural textures during the compression test are predicted by the crystal plasticity finite element (CPFE) simulations, and compared to the available experimental texture and digital image correlation (DIC) data.

The organization of Chapter 2 is as follows: Section 2.1 introduces the ODF approach, and presents the crystal plasticity modeling, which implements the ODF approach and rate-independent single crystal constitutive model. The optimization problem defined for the slip system parameters identification of Ti-0Al and Ti-7Al, and the optimum results are discussed in Section 2.2. A sensitivity analysis is performed to analyze the optimum design variables. The results of this sensitivity study is also presented in Section 2.2. Next, the optimum parameters are used to predict the microstructural texture during the compression test, and the additional CPFE and DIC comparison is performed with the optimum design parameters of Ti-7Al. A summary of the chapter is given in Section 2.3.

2.1 Multi-scale modeling of microstructures

One important aspect in modeling is to determine which slip systems are active during tension and compression tests. The number of the slip systems also determines the design variables here since the optimization is performed for the parameters of all active slip systems. Metals having a hexagonal close-packed (HCP) crystal structure, such as Titanium, are expected to display easy $< a >$ slip, either on the prismatic or basal plane [44]. The observed slip systems in pure HCP Titanium are the three equivalent basal $0001 < 11\bar{2}0 >$, three equivalent prismatic $10\bar{1}0 < 11\bar{2}0 >$ and six equivalent pyramidal $10\bar{1}1 < 11\bar{2}0 >$ slip systems [45]. All these three slip systems share a common slip direction, $< 11\bar{2}0 >$, or, $< a >$. The slip on these basal, prismatic and pyramidal slip systems is denoted as $< a >$-slip. In order to accommodate a

strain that is parallel to the c-axis of the hexagonal system other slip or twinning deformation modes are required. One of these additional modes slips on pyramidal planes with $< 11\bar{2}3 >$, or $< c + a >$ slip directions [45]. In addition, twinning is commonly observed in Ti and other metals with an HCP crystal structure, and it has a strong effect on the overall behavior of a polycrystal material [45].

The deformation behavior of HCP-Ti and Ti alloys has been studied in literature extensively [44, 45, 46, 47, 48, 49, 50, 51]. These studies revealed that the Ti alloys have complex slip and twinning modes. These complexities are mostly because of the crystallographic nature of the alpha (α) phase and addition of alloying elements such as Aluminum (Al) [46]. The effect of Al is not fully understood yet since there is still an ongoing debate in literature about the effect of Al to twinning [46, 47, 48, 49, 50, 51]. Some references claim that Al addition is effective in suppressing twinning [46, 47, 48]. Williams et. al [46] observed that the frequency of twinning rapidly decreases when the Al content increases to 5 % and 6.6 % from 1.4 % and 2.9 % respectively. They found the compression twins to be very difficult to nucleate in Ti-Al single crystals when the Al content is more than 5wt%. Paton et al. [49] discuss that the Ti-Al alloy with 6wt% Al does not twin even at temperatures as low as 100 K. On the other hand, some references [44, 50, 51] claim that Al addition has an increasing effect up to a peak level and then after this point the further Al addition suppresses the twinning effect. Fitzner et. al [51] performed a detailed experimental study to investigate the effect of Al addition to twinning activity in Ti-Al alloys, and they found that at around 7 atomic (at)%Al there is a turning point in twinning activity and a further increase in Al reduced the twinning activity because of short range ordering and signs of Ti_3Al formation in case of the highest Al content they observed (13at%). They discussed the $10\bar{1}2 < \bar{1}011 >$ tensile twin, and concluded that it provides a near 90 degrees rotation of the c-axis from a tensile to a compressive stress condition, and increases the intensity of basal texture during

compression loading. The authors also analyzed the EBSD data and observed an increasing fraction of $10\bar{1}2 < \bar{1}011 >$ twins until 7 at%Al, which then drops suddenly with further Al addition. As a secondary twinning mode 4% of $11\bar{2}2 < 11\bar{2}\bar{3} >$ compression twins were observed only in Ti-0Al case. Due to the small effect of the secondary twinning mode, only the $10\bar{1}2 < \bar{1}011 >$ twin mechanism is considered in this study when modeling the Ti-Al alloys.

This section discusses the crystal plasticity modeling framework which is based on the ODF approach. The details of the ODF model, and probability update are given in Section 2.1.1 and Section 2.1.2. The rate-independent single crystal plasticity model is explained in Section 2.1.3.

2.1.1 Introduction to the ODF approach

Crystal plasticity modeling with the ODF approach is an efficient alternative to computationally expensive FE methods. The ODF, denoted by $\boldsymbol{A(r)}$, is a one-point probability measure, which quantifies the volume fractions of the crystals in the orientation space, $\boldsymbol{r}$. The ODF is defined based on a parameterization of the crystal lattice rotation. In this study, an FE technique was implemented to discretize the ODFs over the Rodrigues space. This is based on the unique association of an orientation with a rotation axis, and an angle of rotation about the axis. The Rodrigues parameterization is created by scaling the axis of rotation, $\boldsymbol{n}$, as $\boldsymbol{r} = \boldsymbol{n}tan(\frac{\theta}{2})$, where θ is the rotation angle. A proper rotation, $\boldsymbol{R}$, relates the lattice orientation to a reference orientation. Given the Rodrigues parameterization, $\boldsymbol{r}$, the rotation, $\boldsymbol{R}$, can be obtained as:

$$\boldsymbol{R} = \frac{1}{1 + \boldsymbol{r}.\boldsymbol{r}}(\boldsymbol{I}(1 - \boldsymbol{r}.\boldsymbol{r}) + 2(\boldsymbol{r} \otimes \boldsymbol{r} + \boldsymbol{I} \times \boldsymbol{r})) \tag{2.1}$$

The complete orientation space of a polycrystal can be reduced to a smaller subset, called the fundamental region (Fig. 2.1), as a consequence of crystal symmetries. Within the fundamental region, each crystal orientation is represented uniquely by a coordinate, $\boldsymbol{r}$, the parameterization for the rotation (e.g. Euler angles, Rodrigues vector, etc.). The fundamental region, which is shown in Fig. 2.1, is discretized into N independent nodes with N_{elem} FEs (and N_{int} integration points per element).

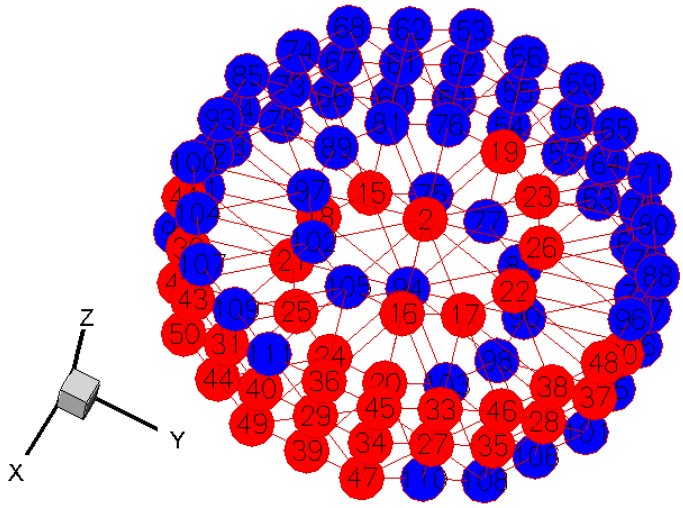

Figure 2.1: ODF representation in the Rodrigues fundamental region for hexagonal crystal symmetry showing the location of the k=50 independent nodes of the ODF in red color

The ODF is normalized to unity over the fundamental region as:

$$\int_{\mathcal{R}} \boldsymbol{A} dv = \sum_{n=1}^{N_{elem}} \sum_{m=1}^{N_{int}} A(\boldsymbol{r_m}) w_m |J_n| \frac{1}{(1 + \boldsymbol{r_m} \cdot \boldsymbol{r_m})^2} = 1 \tag{2.2}$$

where $A(\boldsymbol{r}_m)$ is the value of the ODF at the m^{th} integration point with global coordinate $\boldsymbol{r}_m$ of the n^{th} element, $|J_n|$ is the Jacobian determinant of the n^{th} element and w_m is the integration weight associated with the m^{th} integration point. This is equivalent to the linear constraint: $\boldsymbol{q}^{int^T} \boldsymbol{A}^{int} = 1$, where $q_i^{int} = w_i |J_i| \frac{1}{(1+r_i \cdot r_i)^2}$ and $A_i^{int} = A(\boldsymbol{r}_i)$, where $i = 1, \ldots, N_{int} \times N_{elem}$. Here, $dv = \sqrt{det \boldsymbol{g}}\ dr_1 dr_2 dr_3$. Since the orientation

space is non-Euclidean, the volume element is scaled by the term $\sqrt{det\boldsymbol{g}} = cos^4(\theta/2)$ where $\boldsymbol{g}$ is the metric for the space. If the orientation-dependent property for single crystals, $\chi(\boldsymbol{r})$, is known, any polycrystal property can be expressed as an expected value, or average, over the ODF as follows:

$$< \chi >= \int \chi(\boldsymbol{r}) A(\boldsymbol{r}) dv \tag{2.3}$$

This equation can be expressed in a linear form using an FE discretization as follows:

$$< \chi >= \int_{\mathcal{R}} \chi(\boldsymbol{r}) A(\boldsymbol{r}) dv = \sum_{n=1}^{nel} \sum_{m=1}^{nint} \chi(\boldsymbol{r}_m) A(\boldsymbol{r}_m) w_m |J_n| \frac{1}{(1 + \boldsymbol{r}_m \cdot \boldsymbol{r}_m)^2} \tag{2.4}$$

This is again equivalent to an equation linear in the ODF: $< \chi >= \boldsymbol{p}^{int^T} \boldsymbol{A}^{int}$, where $p_i^{int} = \chi(r_i) w_i |J_i| \frac{1}{(1+r_i \cdot r_i)^2}$ and $A_i^{int} = A(r_i)$, $i = 1, \ldots, N_{int} \times N_{elem}$.

Using reduced integration with one integration point per element at local coordinate of $(0.25, 0.25, 0.25)$ and an integration weight of $w = \frac{1}{6}$, the simplified property matrix $\boldsymbol{p}^{int}$ corresponding to polycrystal average properties $[< \chi_1 >, \ldots, < \chi_{n_p} >]$ and the normalization constraint vector ($\boldsymbol{q}^{int}$) are given as:

$$\boldsymbol{p}^{int} = \begin{bmatrix} \frac{1}{6}\chi_1(\boldsymbol{r}_1)|J_1|\frac{1}{(1+r_1 \cdot r_1)^2} & \cdots & \frac{1}{6}\chi_{n_p}(\boldsymbol{r}_1)|J_1|\frac{1}{(1+r_1 \cdot r_1)^2} \\ \frac{1}{6}\chi_1(\boldsymbol{r}_2)|J_2|\frac{1}{(1+r_2 \cdot r_2)^2} & \cdots & \frac{1}{6}\chi_{n_p}(\boldsymbol{r}_2)|J_2|\frac{1}{(1+r_2 \cdot r_2)^2} \\ \cdots & & \\ \frac{1}{6}\chi_1(\boldsymbol{r}_{N_{el}})|J_{N_{el}}|\frac{1}{(1+r_{N_{el}} \cdot r_{N_{el}})^2} & \cdots & \frac{1}{6}\chi_{n_p}(\boldsymbol{r}_{N_{el}})|J_{N_{el}}|\frac{1}{(1+r_{N_{el}} \cdot r_{N_{el}})^2} \end{bmatrix} \tag{2.5}$$

$$\boldsymbol{q}^{int} = \begin{bmatrix} \frac{1}{6}|J_1|\frac{1}{(1+r_1\cdot r_1)^2} \\ \frac{1}{6}|J_2|\frac{1}{(1+r_2\cdot r_2)^2} \\ \cdots \\ \frac{1}{6}|J_{N_{el}}|\frac{1}{(1+r_{N_{el}}\cdot r_{N_{el}})^2} \end{bmatrix} \tag{2.6}$$

The $\boldsymbol{H}$ matrix can be defined from the equation $A_e^{int} = 0.25\sum_{i=1}^{4} A_e^i$ where A_e^{int} is the integration point ODF value at element e and $A_e^i, i = 1, \ldots, 4$ refers to the ODF values at the four nodes of the tetrahedral element e. The $\boldsymbol{p}$ matrix is formed as $\boldsymbol{p} = \boldsymbol{H}^T\boldsymbol{p}^{int}$ so that any property $\boldsymbol{d}$ can be represented as the scalar product $\boldsymbol{p}^T\boldsymbol{A}$ with the ODF values ($\boldsymbol{A}$) at the independent nodal points.

2.1.2 Probability update

When deformed, the ODF changes due to reorienting of grains. The probabilities are evolved from time $t = 0$ corresponding an initial ODF, which is defined to represent a random texture (all the ODF values are equal to each other) in this chapter. The initial orientation $\boldsymbol{r}_o$ of a crystal reorients during deformation and maps to a new orientation $\boldsymbol{r}_t$ at time t. It is assumed that the mapping from $\boldsymbol{r}_o$ to $\boldsymbol{r}_t$ is invertible. The ODF, $A(\boldsymbol{r}_t)$, represents the volume density of crystals with orientation $\boldsymbol{r}_t$ at time t. The evolution of the ODF is given by the conservation equation (Eq. 2.7) as:

$$\int A(\boldsymbol{r}_o, t = 0)d\boldsymbol{r}_o = \int A(\boldsymbol{r}_t)d\boldsymbol{r}_t = 1 \tag{2.7}$$

where $d\boldsymbol{r}_o$ represents the volume element in the undeformed (initial) ODF mesh, which becomes volume element $d\boldsymbol{r}_t$ at time t. A Jacobian $J(\boldsymbol{r}_o, t) = \det(\boldsymbol{G})$ gives the ratio of elemental volumes, where $\boldsymbol{G}$ is the reorientation gradient given as $\boldsymbol{G}(\boldsymbol{r}_o, t) = \frac{\partial \boldsymbol{r}_t}{\partial \boldsymbol{r}_o}$. Using the Jacobian, a map of the current mesh (at time t) to the reference mesh

(at $t = 0$) can be made:

$$\int (A(\boldsymbol{r}_o, t = 0) - \hat{A}(\boldsymbol{r}_o, t) J(\boldsymbol{r}_o, t)) d\boldsymbol{r}_o = 0 \tag{2.8}$$

The quantity written as $\hat{A}(\boldsymbol{r}_o, t)$ is the volume density $A(\boldsymbol{r}_t)$ plotted over the corresponding orientation ($\boldsymbol{r}_o$) in the initial mesh. Thus, $\hat{A}(\boldsymbol{r}_o, t)$ gives the Lagrangian representation of the current ODF in the initial mesh. If the integrand is continuous, a localized relationship of the following form can be used to update the ODF at any time t:

$$\hat{A}(\boldsymbol{r}_o, t) J(\boldsymbol{r}_o, t) = A(\boldsymbol{r}_o, t = 0) \tag{2.9}$$

For computing $\boldsymbol{r}_t$, a reorientation velocity (it is computed from the constitutive model presented in Section 2.1.3.), $\boldsymbol{v} = \frac{\partial \boldsymbol{r}_t}{\partial t} = \frac{1}{2}(\boldsymbol{\omega} + (\boldsymbol{\omega} \cdot \boldsymbol{r})\boldsymbol{r} + \boldsymbol{\omega} \times \boldsymbol{r})$ is used. The reorientation velocity is computed at each nodal point in the mesh and the change in orientation $\Delta \boldsymbol{r}' = \boldsymbol{r}_t' - \boldsymbol{r}_o'$ is then stored at the nodal points in the fundamental region. Here, the Jacobian is simply the ratio of element lengths, i.e. current length divided by the initial length. If the element length decreases over time, the probability density has to increase based on Eq. 2.2 to maintain normalization of the ODF. The integrand in Eq. 2.8 needs to be continuous for the localization relationship to be valid. Thus, it is implied that $J(\boldsymbol{r}_o, t)$ needs to be continuous and consequently, $\boldsymbol{v}$ needs to be continuously differentiable (at least piecewise) in the fundamental region. The latter is rather a restriction on the constitutive model and macro-micro linking assumption that is used to compute $\boldsymbol{v}$. The differentiability of $\boldsymbol{v}$ also ensures the invertibility of the map from $\boldsymbol{r}_o$ to $\boldsymbol{r}_t$.

2.1.3 Constitutive model

In this work, a rate-independent single-crystal plasticity model developed in Anand and Kothari [17] is used to compute the effect of macroscopic strain on the polycrystal. For a material with $\alpha = 1, \ldots, N$ slip systems defined by ortho-normal vector pairs ($\boldsymbol{m}^\alpha$,$\boldsymbol{n}^\alpha$) denoting the slip direction and slip plane normal respectively, the constitutive equations relate the following basic fields: the deformation gradient $\boldsymbol{F}$ which can be decomposed into elastic and plastic parts as $\boldsymbol{F} = \boldsymbol{F}^e\boldsymbol{F}^p$, the Cauchy stress $\boldsymbol{T}$ and the slip resistances $s^\alpha > 0$. In the constitutive equations (intended to characterize small elastic strains) to be defined below, the Green elastic strain measure $\bar{\boldsymbol{E}}^e = \frac{1}{2}\left(\boldsymbol{F}^{eT}\boldsymbol{F}^e - \boldsymbol{I}\right)$ defined on the relaxed configuration (plastically deformed, unstressed configuration) is utilized. The conjugate stress measure is then defined as $\bar{\boldsymbol{T}} = \det\boldsymbol{F}^e(\boldsymbol{F}^e)^{-1}\boldsymbol{T}(\boldsymbol{F}^e)^{-T}$ where $\boldsymbol{T}$ is the Cauchy stress for the crystal.

The constitutive relation, for stress, is given by $\bar{\boldsymbol{T}} = \boldsymbol{\mathcal{L}}^e\left[\bar{\boldsymbol{E}}^e\right]$, where $\boldsymbol{\mathcal{L}}^e$ is the fourth-order anisotropic elasticity tensor. It is assumed that deformation takes place through dislocation glide, and the evolution of the plastic flow is given by:

$$\boldsymbol{L}^p = \dot{\boldsymbol{F}}^p(\boldsymbol{F}^p)^{-1} = \sum_\alpha \dot{\gamma}^\alpha \boldsymbol{S}_0^\alpha sign(\tau^\alpha) \tag{2.10}$$

where $\boldsymbol{S}_0^\alpha = \boldsymbol{m}^\alpha \otimes \boldsymbol{n}^\alpha$ is the Schmid tensor and $\dot{\gamma}^\alpha$ is the plastic shearing rate on the α^{th} slip system. The resolved stress on the α^{th} slip system is given by $\boldsymbol{\tau}^\alpha = \bar{\boldsymbol{T}} \cdot \boldsymbol{S}_0^\alpha$. The resolved shear stress $\boldsymbol{\tau}^\alpha$ attains a critical value s^α on the systems where slip occurs ($\dot{\gamma}^\alpha > 0$). Further, the resolved shear stress does not exceed s^α on the inactive systems with $\dot{\gamma}^\alpha = 0$. The hardening law for the slip resistance s^α is taken as:

$$\dot{s}^\alpha(t) = \sum_\beta h^{\alpha\beta}\dot{\gamma}^\beta,\ s^\alpha(0) = s_0^\alpha \tag{2.11}$$

The slip system hardening model used in the calibration study is given below:

$$h^{\alpha\beta} = [q + (1-q)\delta^{\alpha\beta}]h^{\beta} \quad \text{(no sum on } \beta) \tag{2.12}$$

where h^{β} is a single slip hardening rate, q is the latent-hardening ratio and $\delta^{\alpha\beta}$ is the Kronecker delta function. The parameter q is taken to be 1.0 for coplanar slip systems and 1.4 for non-coplanar slip systems. For the single-slip hardening rate, the following specific form is adopted:

$$h^{\beta} = h_o(1 - \frac{s^{\beta}}{s_s})^a \tag{2.13}$$

where h_o, a, and s_s are slip hardening parameters. The ODF model is examined for tensile and compression stress-strain behavior of Ti-0Al and Ti-7Al alloys. Basal $< a >$, prismatic $< a >$, pyramidal $< a >$ and pyramidal $< c + a >$ slip systems are modeled as well as the $10\bar{1}2 < \bar{1}011 >$ twinning mechanism. The elastic parameters are taken as [52]: $C_{11} = C_{12} = 175$ GPa, $C_{12} = 88.7$ GPa, $C_{13} = C_{23} = 62.3$ GPa, $C_{44} = C_{55} = 62.2$ GPa, and $C_{66} = (C_{11} - C_{12})/2$.

2.2 Optimization for slip system parameters identification of Ti-Al alloys

The fundamental goal of this chapter is to identify the slip system parameters of Ti-Al alloys, Ti-0Al and Ti-7Al, using the crystal plasticity modeling with the ODF approach. For this study, a genetic algorithm, Non-Dominated Sorting Genetic Algorithm (NSGA-II) [53], is implemented with a global sampling method, Incremental Space Filler (ISF) [54], to calibrate the computational model according to the available experimental data. The optimization is performed to identify 20 design variables which are 4 slip system parameters (s_0, h_0, s_s and a) of 5 different

slip systems taken into consideration. These slip systems are basal $< a >$, prismatic $< a >$, pyramidal $< a >$ and pyramidal $< c + a >$ as well as the $10\bar{1}2 < \bar{1}011 >$ twinning mechanism. The optimization problem is defined similarly for both alloys, and the objective functions are determined to minimize the L_2 norm errors between the true stress-true strain curves of the experimental data and ODF simulation for both tension and compression tests. The slip system parameters, which are obtained by Salem et. al [55] for basal $< a >$, prismatic $< a >$, pyramidal $< a >$, pyramidal $< c + a >$ slip systems and twinning, are used to define the lower bounds of the optimization variables. The initial texturing of the material is assumed to be random. The mathematical formulation of the multi-objective optimization problem is given below:

$$min \;\; \epsilon_t, \quad min \;\; \epsilon_c \tag{2.14}$$

$$\boldsymbol{s} = (s_0, h_0, s_s, a) \tag{2.15}$$

In Eq. 2.14, ϵ_t and ϵ_c show the L_2 norm errors between true stress points of the experimental data and ODF simulation for tension (denoted by t) and compression (denoted by c) tests. The experimental data is available up to 15% strain, therefore the ODF simulations are performed for the same strain level. The strain rate is defined as 2.5×10^{-4}, and a quadratic interpolation is implemented to match the experimental and computational strain points. In Eq. 2.15, $\boldsymbol{s}$ shows the vector representation of 20 optimization variables for 5 slip systems.

2.2.1 Optimization of slip system parameters for Ti-0Al

The optimization problem defined in Eq. 2.14 and 2.15 is solved using NSGA-II as the optimization algorithm, and ISF as the global sampling algorithm in Modefrontier software. The optimum slip system parameters of Ti-0Al are shown in Table 2.1. The

only information in literature [44], to the best of the author's knowledge, discusses that the s_0 value of the pyramidal $< c+a >$ slip system should be 3-5 times higher than the s_0 value of the prismatic $< a >$ slip system. This statement in Ref. [44] is supported by the optimization results reported in Table 2.1. The true stress-true strain curves, which are predicted using the optimum design parameters in the ODF based crystal plasticity model, are compared to the experimental data in Fig. 2.2 for tension and compression respectively. Another experimentally available comparison metric is the $< 002 >$ and $< 100 >$ PFs measured at 9% strain in compression test, which is presented by Fitzner [50]. The texture is also predicted by the ODF based crystal plasticity simulation using the optimum slip system parameters, and compared to the experimental data in Fig. 2.3.

Table 2.1: Optimum slip system parameters of Ti-0Al

Slip System	s_0	h_0	s_s	a
Basal $< a >$	88.11 MPa	215.58 MPa	1175.9 MPa	0.25
Prismatic $< a >$	89.49 MPa	215.58 MPa	1175.9 MPa	0.25
Pyramidal $< a >$	161.13 MPa	215.58 MPa	1175.9 MPa	0.25
Pyramidal $< c+a >$	355.17 MPa	215.58 MPa	1175.9 MPa	0.25
Twinning	507.63 MPa	200.11 MPa	1175.9 MPa	0.25

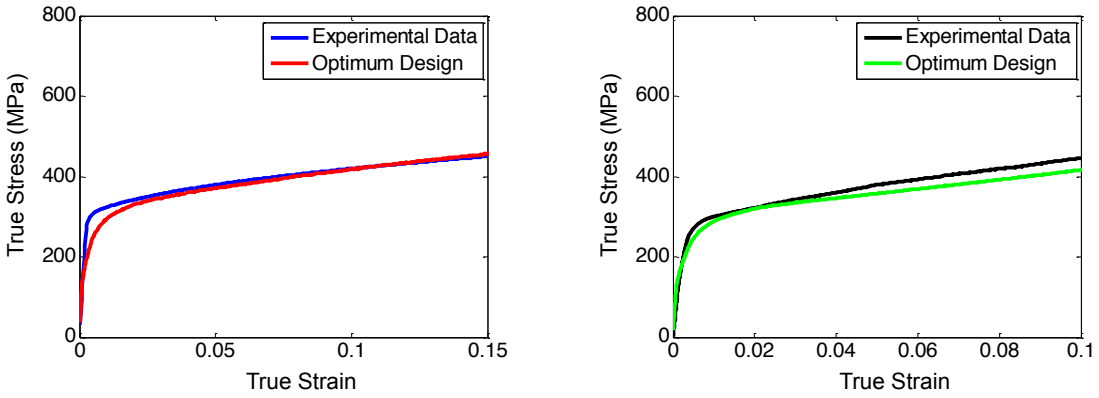

(a) Tension curve

(b) Compression curve

Figure 2.2: True strain-true stress curve comparison of experimental data and optimum design for Ti-0Al

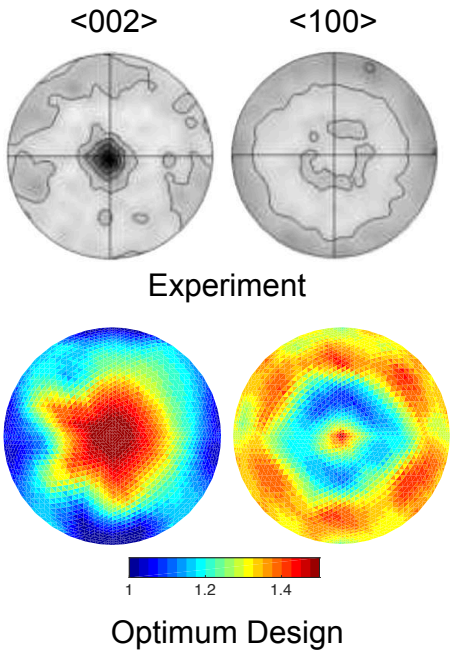

Figure 2.3: $< 002 >$ and $< 100 >$ PFs at 9% compressive strain (Experimental data is given by Fitzner [50])

As shown by the true stress-true strain curve results in Fig. 2.2, the optimum slip system parameters generate an accurate computational model according to the available tension and compression test data for Ti-0Al. The difference between the experimental and computational stresses during the small strain levels is because of the initial texture uncertainties. The crystal plasticity simulations are performed with the random texture assumption to model the initial texture. However, in reality, the experimental texture slightly varies from the random texture, and corresponds to a weakly basal texture. The important point here is that it is still possible to identify the optimum parameters under the effect of initial texture uncertainties since they are more effective when the strain is small, and then the computational model tends to converge to the experimental data when the strain is higher. The uncertainties also cause small differences in PFs as shown in Fig. 2.3.

The sensitivities of the optimum parameters to the tension and compression design objectives (min ϵ_t and min ϵ_c respectively) are investigated using sample points

generated with Latin Hypercube Sampling (LHS) [56]. 10 sample points per each variable, and therefore 200 sample points in total are generated. Each parameter is assumed to vary up to ±10 % around its optimum value with a Gaussian distribution, and the others remain constant at their optimum values. The sensitivities are represented as a percent bar graph in Fig. 2.4 which shows the average % change in the design objective given up to 10% changes around the optimum values of the variables. The sensitivity analysis is performed for both tension and compression tests.

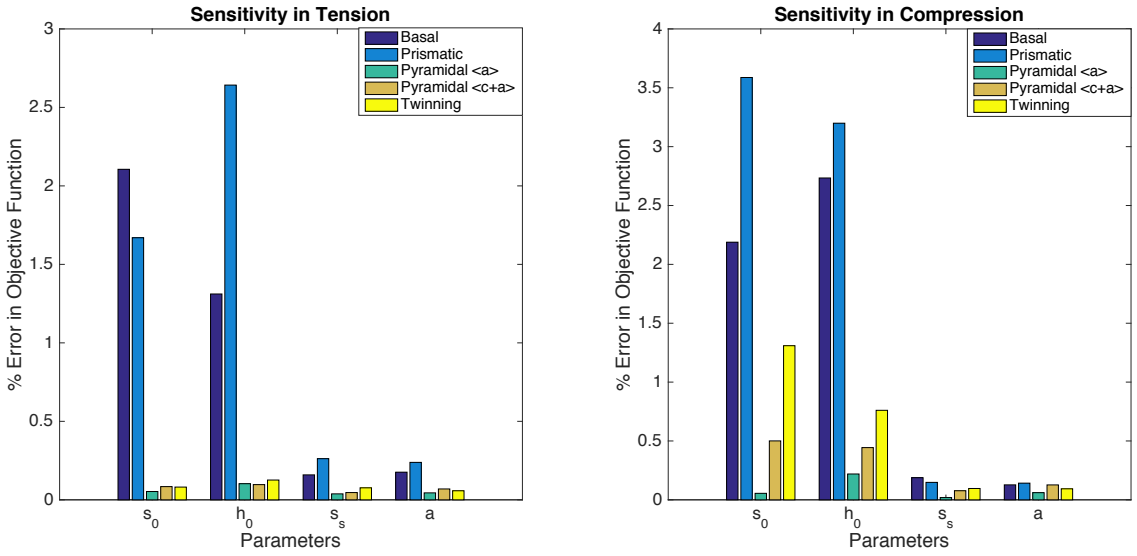

Figure 2.4: Sensitivity analysis results for optimum design parameters of Ti-0Al

According to the sensitivity results shown in Fig. 2.4, the most critical slip systems are determined as the basal and prismatic slip systems. The objective function values are also more sensitive to the changes in s_0 and h_0 parameters rather than the changes in s_s and a in both tension and compression. The tension test is sensitive to both basal and prismatic slip systems, however, in compression, the prismatic slip system is determined to be more effective. The remaining slip systems do not play a dominant role in tension and it can be assumed that they have negligible effects; however, twinning and pyramidal $< c+a >$ becomes more effective in compression compared to their negligible sensitivities in tension. This is an expected results since the twinning

was assumed to be active during compression.

2.2.2 Optimization of slip system parameters for Ti-7Al

The same optimization problem, which is defined in Eq. 2.14 and 2.15, is solved for Ti-7Al using NSGA-II as the optimization algorithm, and ISF as the global sampling method. The optimum slip system parameters of Ti-7Al are shown in Table 2.2. These parameters are also compared to the available information in literature regarding the critical resolved shear stress (CRSS) values of different slip systems of Ti-7Al in Table 2.3. The optimum CRSS results match with the information provided in literature as can be seen in Table 2.3. However, there is no information regarding the CRSS values of twinning and pyramidal $< a >$ slip system. The optimization problem in this study is unique in this sense since it is the first time all the CRSS and hardening parameters are identified. The tension and compression curves obtained through the ODF simulation using the optimum design parameters is compared to the experimental data in Fig. 2.5. The microstructural texture at 20% compressive strain is predicted by using the optimum design parameters, and compared to the experimental data in Fig. 2.6. Another texture comparison is made through comparing the $< 001 >$, $< 100 >$ and $< 101 >$ PFs at 20% compressive strain as shown in Fig. 2.7.

Table 2.2: Optimum slip system parameters of Ti-7Al

Slip System	s_0	h_0	s_s	a
Basal $< a >$	215.51 MPa	216.18 MPa	1534.20 MPa	1.38
Prismatic $< a >$	250.00 MPa	216.18 MPa	1534.20 MPa	1.38
Pyramidal $< a >$	991.40 MPa	216.18 MPa	1534.20 MPa	1.38
Pyramidal $< c + a >$	999.30 MPa	216.18 MPa	1534.20 MPa	1.38
Twinning	783.37 MPa	1049.70 MPa	1534.20 MPa	3.96

Similarly, the true stress-true strain curve results in Fig. 2.5 indicate an accurate computational representation to the available tension and compression experimental

Table 2.3: CRSS values of different slip systems in Ti-7Al

Reference	s_0^{basal}	s_0^{prism}	s_0^{pyr} $(< c+a >)$	s_0^{pyr} $(< a >)$	s_0^{twin}
Nervo et. al [44]	-	-	$3-5 \times s_0^{prism}$	-	-
Williams et. al [46]	$\approx s_0^{prism}$	$\approx s_0^{basal}$	-	-	-
Lutjering and Williams [48]	$\sim$ 200 MPa	$\sim$ 200 MPa	$\sim$ 800 MPa	-	-
Shahba and Ghosh [57]	230 MPa	205 MPa	610 MPa [1]	-	-
Present study	215.51 MPa	250.00 MPa	999.30 MPa	991.40 MPa	783.37 MPa

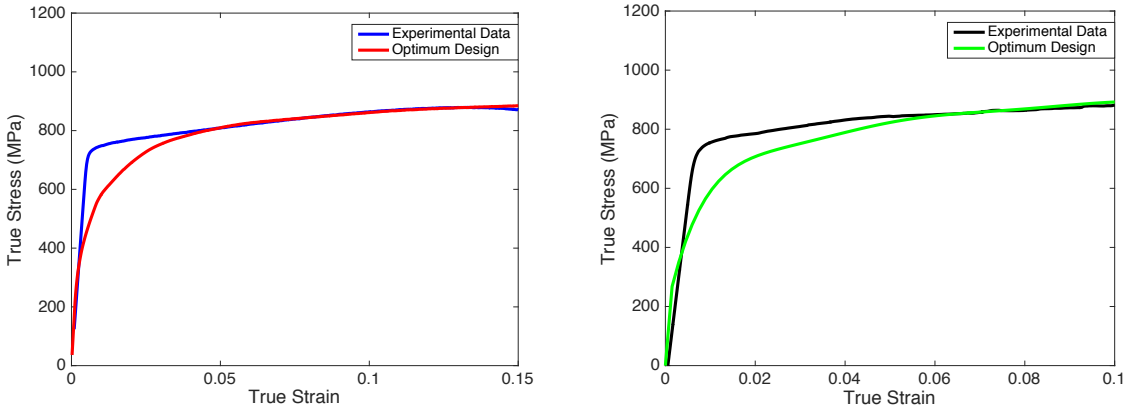

(a) Tension curve (b) Compression curve

Figure 2.5: True strain-true stress curve comparison of experimental data and optimum design for Ti-7Al

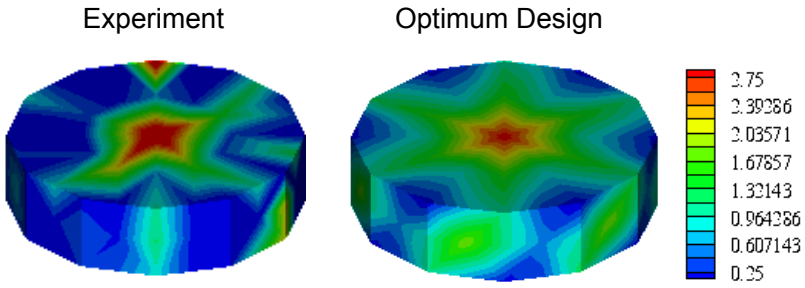

Figure 2.6: Comparison of Ti-7Al microstructures at 20% compressive strain

data. The initial texture uncertainties affect the computational result as the difference between the computational and experimental stresses is larger when the strain has smaller values. However, the effect of initial texture uncertainties is not important when the strain has higher values as shown in Fig. 2.5. The uncertainties in

[1] The CRSS value is different in this study [57] since the authors modeled two pyramidal $< c+a >$ slip systems (1^{st} and 2^{nd} order)

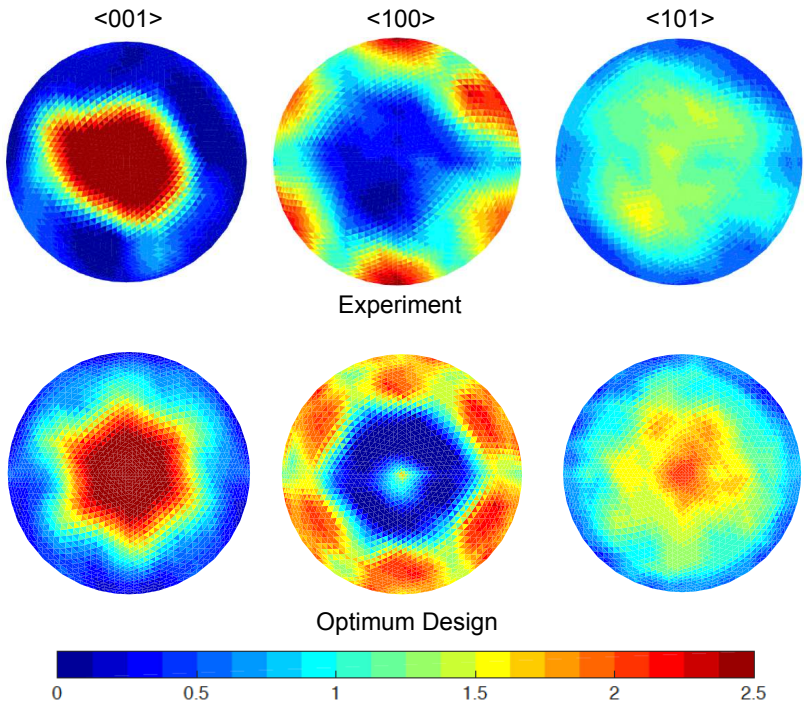

Figure 2.7: $< 001 >$, $< 100 >$ and $< 101 >$ PFs at 20% compressive strain

experimental texture can also be observed in Fig. 2.6 and Fig. 2.7.

A similar sensitivity study, which implements LHS for sampling, is performed to analyze the effect of optimum variables to design objectives using 10 samples per variable, 200 samples in total. The sensitivities are represented as a percent bar graph in Fig. 2.8 which shows the average % change in the design objective given up to 10% changes around the optimum values of the variables. The sensitivity analysis is performed for both tension and compression tests.

According to the sensitivity results shown in Fig. 2.8, the most critical slip systems are determined as the basal and prismatic slip systems. The objective function values are also more sensitive to the changes in s_0 and h_0 parameters rather than the changes in s_s and a in both tension and compression. The tension test is sensitive to both basal and prismatic slip systems, however, in compression, the prismatic slip system is determined to be more effective. Twinning was expected to be active during compression, and as the sensitivity results indicate it becomes more effective in the

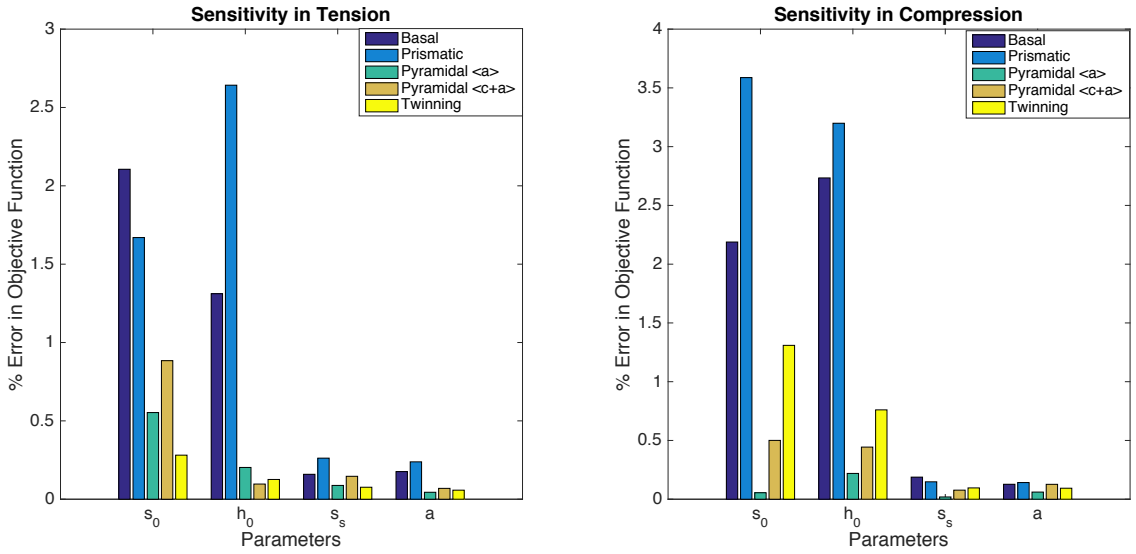

Figure 2.8: Sensitivity analysis results for optimum design parameters of Ti-7Al

compression test. After basal and prismatic slip systems, the third most dominant slip system is found to be pyramidal $< c + a >$ in tension, and it is followed by pyramidal $< a >$ and finally by twinning. However, the third most dominant system is twinning in compression. This also clearly indicates the necessity of including twinning in crystal plasticity modeling of Ti-Al alloys.

2.2.3 CPFE analysis for Ti-7Al

The optimum slip system parameters of Ti-7Al are used to perform a CPFE analysis, and the strain field results are compared to the available experimental DIC data. The simulation is performed using 10000 elements and the strain fields (e_{xx}, e_{yy} and e_{xy} strains) are computed. The DIC data is available at 13.5% tensile strain, it is compared to the CPFE results in Fig. 2.9, Fig. 2.10 and Fig. 2.11 for e_{xx}, e_{yy} and e_{xy} strain fields respectively.

The CPFE results inputting the optimum slip system parameters are sufficiently accurate compared to the available DIC data. This result is important since the DIC data provides the actual strain fields, and it is a more accurate experimental measure

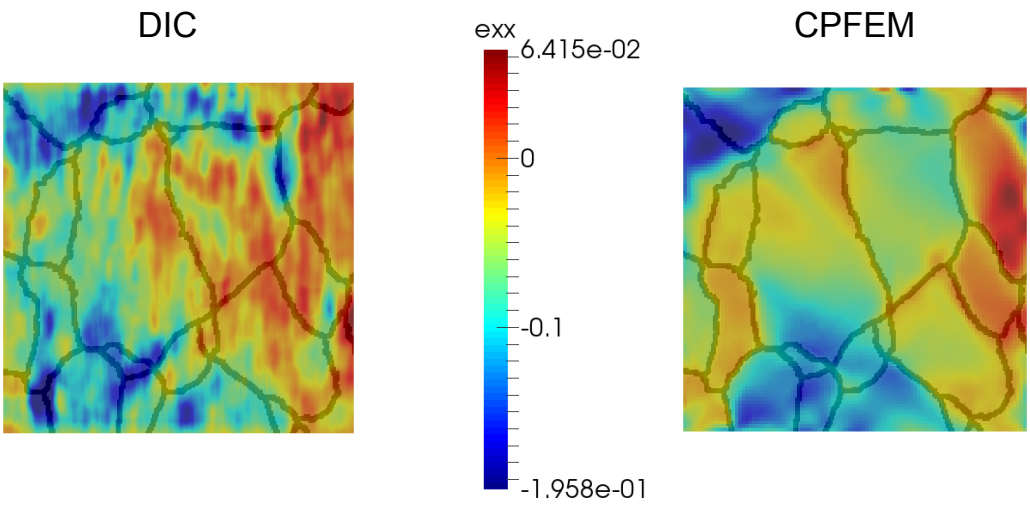

Figure 2.9: CPFE simulation and DIC data comparison for e_{xx} strain field

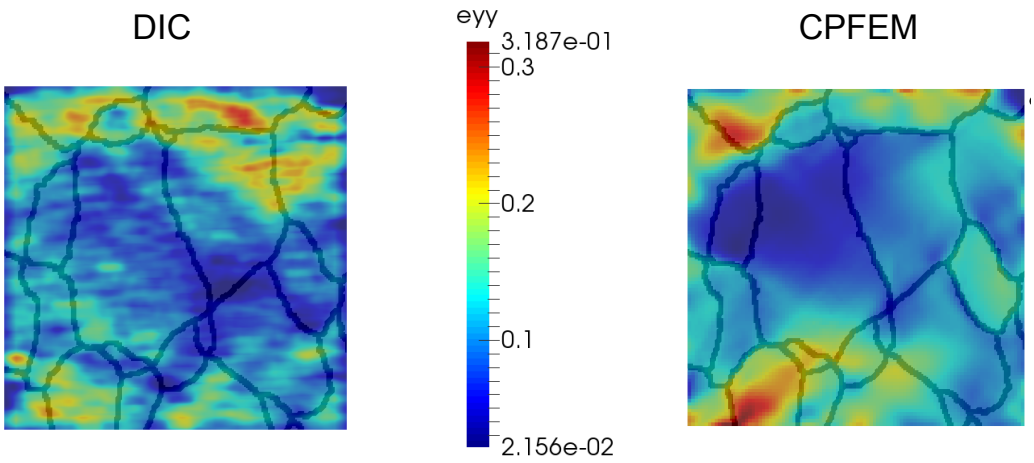

Figure 2.10: CPFE simulation and DIC data comparison for e_{yy} strain field

compared to the global stress-strain curves.

The crystal plasticity modeling based on the ODF approach is used to compute the property matrices ($\boldsymbol{p^T}$) using the single crystal designs. The example single crystal properties (stiffness, thermal expansion and yield stress) of the α-Ti material is shown in Fig. 2.12.

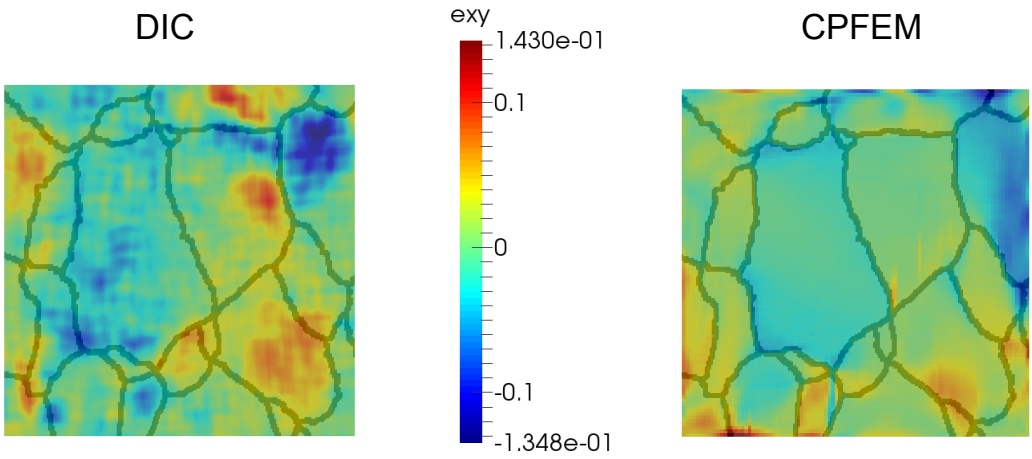

Figure 2.11: CPFE simulation and DIC data comparison for e_{xy} strain field

2.3 Conclusion

An optimization study is performed to identify the slip system parameters of Ti-Al alloys (Ti-0Al and Ti-7Al) using the available tension and compression experimental data showing the true stress-true strain curves of the alloys. The optimum results provide an accurate computational representation in comparison with the experimental data. Additional experimental data, which illustrates the microstructural texture at 9% and 20% strains in compression test, is used as an another metric for verification of the optimum design. The predicted microstructures using the optimum variables show similarities to the experimental data. The differences, which are seen in the stress-strain curves and microstructural texture, stem from the uncertainties in the measurements and initial texture. The computational model inputs a random initial texture, however, the experiments were performed with a texture, which was slightly different than the random texture, a weakly basal texture. Not only the stress-strain curves but also the microstructural texture comparisons show a good agreement. A CPFE simulation is performed to compute the strain fields of Ti-7Al in different directions, and the results are compared to the available experimental data at 13.5% tensile strain. The crystal plasticity system realization for Ti-0Al and Ti-7Al is sig-

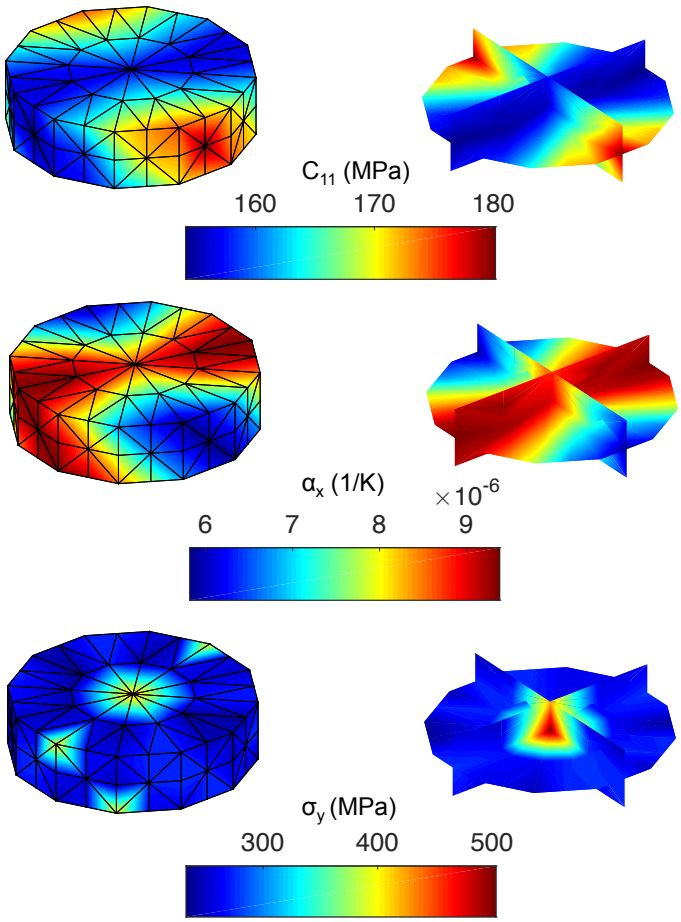

Figure 2.12: Single crystal properties for stiffness, thermal expansion and yield stress of α-Ti

nificant since these slip system parameters are not studied extensively in literature. There are studies to identify the slip system parameters of other Ti-Al alloys, such as Ti-6Al-4V, however, there has not been published any study focusing on the parameter identification for modeling Ti-7Al alloy to the best of the author's knowledge. The present work is the first attempt to identify all the slip system parameters of the Ti-Al alloys of interest.

CHAPTER 3

Multi-Scale Design and Optimization of Microstructures

The objective of this chapter is to identify the optimum microstructure design which maximizes/minimizes the value of a macro-scale material property. The microstructure is represented using the ODF values, and the optimum values of the ODFs are computed for different engineering applications. Since the ODF solution is high-dimensional, the design space is reduced to a new space, called property closure. The property closure is the space of the important material properties of an engineering problem, and it includes all possible microstructure designs. When a lower or upper bound homogenization approach is employed, the property closure is simply a convex hull with the vertices represented by single crystal properties. The optimization problem is solved in this new space to find the optimum microstructure design. In materials design problems, another important aspect is the possibility of having multiple microstructure designs which provide the same optimum material properties. The existence of independent solution directions and multiple microstructure designs is checked with the implementation of a direct linear solver, which uses the first optimum solution as well as the volume averaging equations required to compute the material properties in terms of the ODF values. The proposed flowchart for multi-scale design optimization of materials is also illustrated in Fig. 3.1.

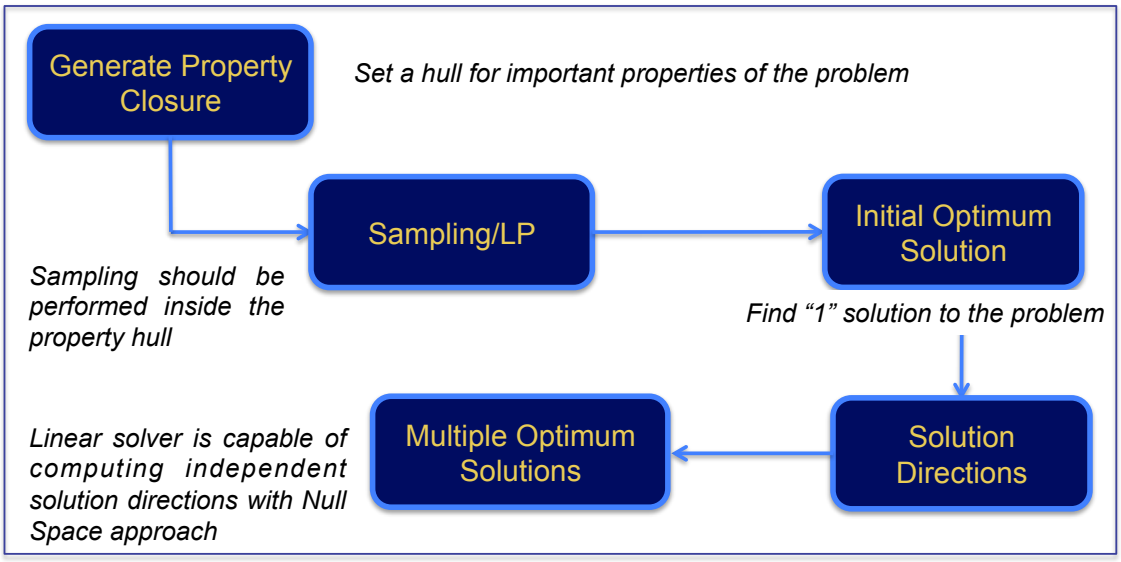

Figure 3.1: Flowchart for multi-scale design optimization of materials

The materials design optimization methodology is applied to two different engineering problems. The first problem is a thermal buckling application for a Ti aircraft panel. The design objective of the first application problem is to find the optimum microstructure design which withstands the maximum temperature change without buckling or yielding occurs. The second example is a vibration tuning problem for a cantilever beam which is made of Galfenol (Fe-Ga alloy). The design objective of the second problem is to identify the optimum microstructure design which maximizes the yield stress of the beam while satisfying design constraints which are defined for the first bending and torsion natural frequencies for vibration tuning. This application leads to multiple optimum polycrystal solutions, and these designs are computed using the direct linear solution algorithm. The organization of Chapter 3 is as follows: Section 3.1 discusses the multi-scale design optimization methodology. The applications are introduced and the results are reported in Section 3.2. A final discussion about the numerical scheme and optimization results is given in Section 3.3.

3.1 Multi-scale design optimization methodology

The multi-scale design starts from microstructural scale modeling by using the ODF approach. The ODF quantifies the volume fractions of different orientations in a microstructure. The material properties are calculated using the volume averaging equations which are linear in terms of the ODFs. The fundamental goal of the multi-scale design optimization framework is to find the optimum microstructure design to maximize/minimize a macro engineering material property. The proposed design approach is applied to two engineering problems. The definition of the optimization problems can vary depending on the application; however, there are some mathematical design constraints which are required to be satisfied when solving material design problems with the ODF approach. The generic definition of the optimization problem is discussed in Section 3.1.1. The optimization problem is solved in a reduced space, known as property closure, since the ODF solution space is high-dimensional. The generation of property closures is explained in Section 3.1.2. After identification of the first optimum solution the multiple optimum microstructure designs are also calculated by implementing a direct linear solution algorithm to find the independent solution directions. This direct linear solution scheme is described in Section 3.1.3.

3.1.1 Design optimization problem

The optimization problem enforces three separate constraints on the ODF that is desired: symmetry, normalization, and positiveness. The procedure for optimization is described here.

1. *Symmetry*

   Firstly, the symmetry of the HCP crystal structure is enforced by using only the "independent nodes" in the ODF mesh. Independent nodal points are the reduced set of nodes obtained by accounting for symmetry conditions at the

boundaries of the ODF mesh. Let $\boldsymbol{H}$ be the matrix converting the independent nodal values $\boldsymbol{A^{node}}$ to the integration point values $\boldsymbol{A^{int}}$ through the shape functions, then $\boldsymbol{A^{int}} = \boldsymbol{H}\boldsymbol{A^{node}}$. The vector containing the values of the ODF at independent nodal points $\boldsymbol{A^{node}}$ is sufficient to describe the ODF and is hereafter referred to as $\boldsymbol{A}$.

Remark : Properties are specified using the modified $\boldsymbol{p^T} = \boldsymbol{p^{intT}}\boldsymbol{H}$ as: $< \chi >= \boldsymbol{p^T}\boldsymbol{A}$. For calculating more than one property, $\boldsymbol{p}$ is written in a matrix form. Using reduced integration with one integration point per element at local coordinates of $(0.25,\ 0.25,\ 0.25)$ and an integration weight of $w = \frac{1}{6}$, the $\boldsymbol{H}$ matrix can be defined from the equation $A_e^{int} = 0.25\sum_{i=1}^{4} A_e^i$ where A_e^{int} is the integration point ODF value at element e and A_e^i, $i = 1, ..., 4$ refers to the ODF values at the four nodes of the tetrahedral element e.

2. *Normalization*

   The constraint that the volume fractions sum to one is given by the following relationship:

$$\int_R \boldsymbol{A} dv = \sum_{n=1}^{N_{elem}} \sum_{m=1}^{N_{int}} A(r_m) w_m |J_n| \frac{1}{(1 + r_m \cdot r_m)^2} = 1 \tag{3.1}$$

   This is equivalent to the linear constraint: $\boldsymbol{q^{intT}}\boldsymbol{A^{int}} = 1$ where $q_i^{int} = w_i|J_i|\frac{1}{(1+r_i \cdot r_i)^2}$ and $A_i^{int} = A(r_i)$, where each i corresponds to a combination of (n, m), $i = 1, ..., N_{int} \times N_{elem}$. This can also be written in terms of independent nodes as $\boldsymbol{q^T} = \boldsymbol{q^{intT}}\boldsymbol{H}$ as $\boldsymbol{q^T}\boldsymbol{A} = 1$.

3. *Positiveness*

   The positivity of the ODF is enforced by the constraint $\boldsymbol{A} \geq \boldsymbol{0}$, (i.e. the volume fractions are positive).

The general mathematical representation of the design optimization problem is given below:

$$min \quad f \tag{3.2}$$

$$subject\ to \quad \boldsymbol{q^T A} = 1 \ , \ \boldsymbol{A} \geq \boldsymbol{0} \tag{3.3}$$

where f shows the objective function of the design optimization problem.

3.1.2 Generation of property closure

The optimization problem is solved in property closure, a reduced space of important material properties of the design problem, instead of the ODF space. Property closures represent complete range of properties obtainable from the space of ODFs. These are approximated by the space between upper and lower bounds of the given property. Upper bound closure of material properties represents the range of properties obtainable by the upper bound homogenization relation in Eq. 3.5. The hull in Fig. 3.4, for example, maps the full range of upper bound values of a combination of material properties. The extremal textures always correspond to single crystal designs. A simple technique for constructing property closures (for the homogenization relations considered here) is by establishing the smallest convex region enveloping single crystal property points. The LP approach is although more rigorous, and more intuitive for construction of property closures, since closures are obtained as a result of property maximization or minimization. Connecting faces on the closure may contain polycrystals that are explicitly identified by the LP approach. This approach is also well-suited for other problems, such as identification of textures with desired property combinations where several properties are optimized simultaneously. Let v_1, v_2 be the set of properties for which the closure is required. The closure for property v_1 is first found by obtaining the extremal values (v_{1max}, v_{1min}). Then, property v_1 is dis-

cretized into m values $v_1^i, i = 1, .., m$ between v_{1max} and v_{1min}. The property closure of the combined set of properties (v_1, v_2) is found by executing a similar extremum LP problem at each point v_1^i with the additional constraint that $\boldsymbol{p_1^T A = v_1^i}$. In general, the closure for a combined set of n properties $(v_1, v_2, ..., v_n)$ is a n-dimensional volume found by executing an LP problem minimizing/maximizing v_n at a set of discrete points $(v_1^i, v_2^j, .., v_{n-1}^l)$ in the closure area of $(v_1, v_2, .., v_{n-1})$. The corresponding LP problem for minimizing v_n is written below:

$$\begin{aligned} \mathbf{min}_{\boldsymbol{A}}\, \boldsymbol{v_n} = \boldsymbol{p_n^T A} \text{ satisfying the constraints} \\ \boldsymbol{q^T A} &= 1 \\ \boldsymbol{A} &\geq \mathbf{0} \\ \boldsymbol{p_1^T A} &= v_1^i \\ \boldsymbol{p_2^T A} &= v_2^j \\ &... \\ \boldsymbol{p_{n-1}^T A} &= v_{n-1}^l \end{aligned} \tag{3.4}$$

To maximize v_n another similar problem is executed where the objective is changed as $\mathbf{min}_{\boldsymbol{A}}\, \boldsymbol{v_n} = \boldsymbol{-p_n^T A}$. The closure represents the range of properties obtainable when using the homogenization methodology.

The domain boundaries can be computed using both upper bound and lower bound approaches. Upper bound approach, which is based on constant strain assumption through plate thickness, computes the properties in $\boldsymbol{p}$ space (corresponds to upper bound averaging). However, the lower bound approach, which is based on constant stress assumption through plate thickness, computes the properties in $\boldsymbol{p^{-1}}$. The example computation of an averaged orientation-dependent material property, $< \chi >$, in terms of the ODF values is given in Eq. 3.5:

$$< \chi >= \int_R \chi(\boldsymbol{r}) A(\boldsymbol{r}) dv = \boldsymbol{p^T A} \tag{3.5}$$

Eq. 3.5 corresponds to a linear relation when the integral equation is discretized using FE technique with tetrahedral elements. Thus an LP approach provides exact solutions to the problem of identifying ODFs that lead to a given property.

3.1.3 Utilization of a direct linear solver to identify infinite solutions

The optimization is performed in a solution space that is reduced to the space of important material properties from the complete ODF solution space. This reduction saves a great amount of computational time for any design problem since the complete ODF space is higher dimensional compared to the property closure. After the generation of the property closure the optimization can be performed inside the closure using LP, gradient based optimization or an advanced optimization methodology which requires global sampling depending on the nature of the design problem. The optimum material properties can be identified in the closure, and the corresponding ODF solution is solved using LP. Another important challenge when solving design problems is to find if there is another design which can provide the same optimum material property values. A direct linear solver has been developed to identify these multiple optimum designs. The solver uses the initial (first) optimum solution identified in property closure and the coefficient matrix which links the optimum ODF values to the optimum material properties through volume averaging equations. It is capable of finding the multiple/infinite solutions since it uses null space of this coefficient matrix to find the directions of the solutions. The infinite solutions are defined as the sum of the initial optimum solution and solution directions represented by null space vectors. The infinite solutions can mathematically be represented as shown below:

$$\boldsymbol{A_i} = \boldsymbol{A_1} + \lambda \boldsymbol{V_i}, \text{ where } i = 1, 2, 3, 4, ..., n \tag{3.6}$$

$$\boldsymbol{V_i} = Null(\boldsymbol{C(:, i)}) \ , \tag{3.7}$$

where Eq. 3.6 defines the infinite ODF solutions, $\boldsymbol{A_i}$, using one solution (the initial optimum solution), $\boldsymbol{A_1}$, and null space vectors, $\boldsymbol{V_i}$. n is the number of null space vectors. Even though the number of null space vectors is finite, the number of solutions can be infinite since λ can be any number that satisfies the ODF positiveness constraint ($\boldsymbol{A} \geq \boldsymbol{0}$). Since the optimization problem is solved in the property closure, which is generated by the ODF values through averaging equations, any point inside this solution domain corresponds to a known set of ODF values. Therefore there is always at least one optimum ODF solution inside this domain. The solution strategy aims to find this optimum solution not only when it is unique but also when it is multiple.

3.2 Applications

3.2.1 Thermal buckling of Titanium aircraft panels

Many aerospace applications utilize materials that operate at high temperatures (Fig. 3.2). For example, Titanium panels in high speed vehicles are exposed to elevated temperatures. The microstructure of such alloys has an important effect on the performance under high thermal stresses. Thus, the optimization of the microstructure is expected to significantly improve the performance. Response of plate panels in compression, due to thermal loading and edge restraints, is a classical plate buckling problem. The stability analysis of isotropic metal plates is a general problem and can be found in textbooks [58]. However, the isotropy assumption is not justified when including microstructural effects and is in direct conflict with the trends in new

materials development, where one of the major goals is to enhance the properties of the material in certain directions while sacrificing the properties in other directions where they are not as important (e.g. development of laminated composite systems). Likewise, techniques that allow tailoring of properties of polycrystalline alloys (e.g. Ti, Al used in structural panels) involve tailoring of preferred orientations of various crystals constituting the polycrystalline alloy. This application problem concentrates on optimization of the polycrystalline HCP α-Ti material to maximize the temperature difference that the material can withstand for an aircraft panel thermal buckling problem.

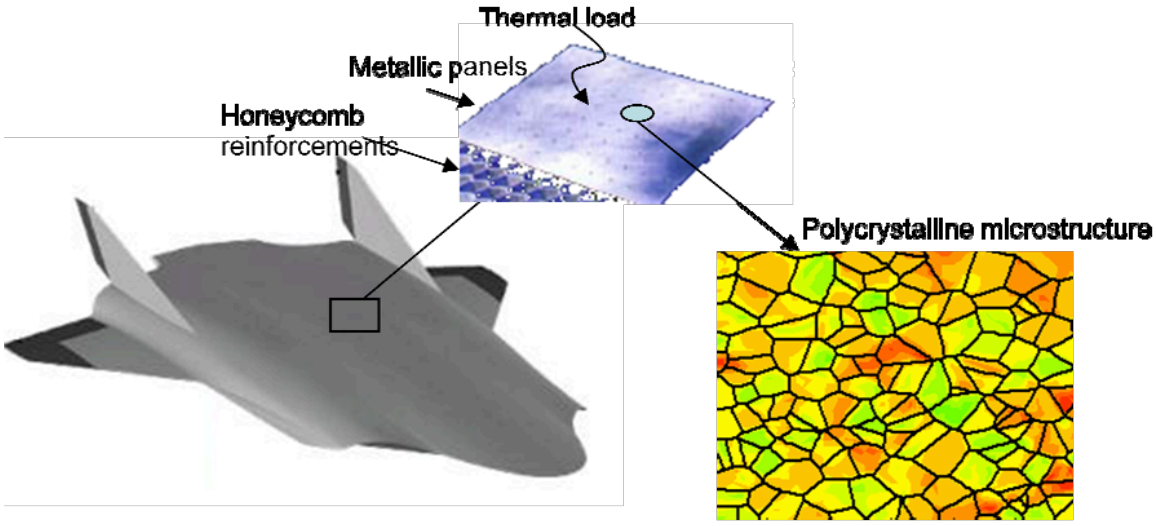

Figure 3.2: Microstructure of high temperature materials

Classical solutions of plate buckling are typically used in engineering calculations for composite plates [59]. Airframe panels made of Ti alloys can be modeled as thin, rectangular, anisotropic plates. The analytical solution, which was previously presented in [16], is available for an orthotropic plate by Lekhnitskii [60]. In this example, a fully anisotropic thermal expansion tensor is included. The analytical solution, which is presented by Lekhnitskii [60], is available for the simply supported plates with orthotropic stiffness coefficients. To implement this analytical solution the stiffness matrix of HCP α-Ti is assumed to be orthotropic since the calculated

anisotropic terms are orders of magnitude smaller than the orthotropic stiffness terms. The principal directions are taken to be parallel to the sides and the material is compressed by uniformly distributed axial load N_x (Fig. 3.3).

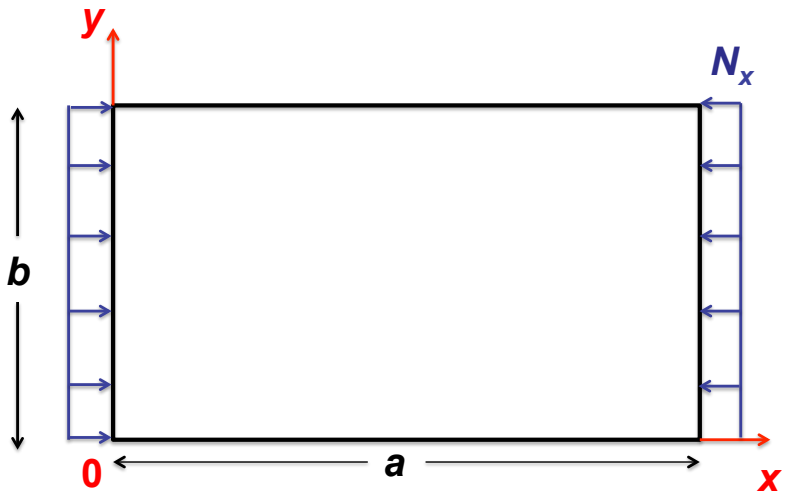

Figure 3.3: Representation of the analytical buckling problem

The deflection equation of the orthotropic plate has the form:

$$D_{11}\frac{\partial^4 w}{\partial x^4} + 2D_{33}\frac{\partial^4 w}{\partial x^2 \partial y^2} + D_{22}\frac{\partial^4 w}{\partial y^4} + N_x\frac{\partial^2 w}{\partial x^2} + N_y\frac{\partial^2 w}{\partial y^2} = 0 \ , \tag{3.8}$$

where D values are the flexural rigidities that are computed using the stiffness tensor components (C_{ij}):

$$\begin{bmatrix} D_{11} & D_{12} & D_{13} \\ D_{21} & D_{22} & D_{23} \\ D_{31} & D_{32} & D_{33} \end{bmatrix} = \frac{h^3}{12} \times \left(\begin{bmatrix} C_{11} & C_{12} & C_{16} \\ C_{21} & C_{22} & C_{26} \\ C_{61} & C_{62} & C_{66} \end{bmatrix} - \begin{bmatrix} C_{13} & C_{14} & C_{15} \\ C_{23} & C_{24} & C_{25} \\ C_{63} & C_{64} & C_{65} \end{bmatrix} \times \left(\begin{bmatrix} C_{33} & C_{34} & C_{35} \\ C_{43} & C_{44} & C_{45} \\ C_{53} & C_{54} & C_{55} \end{bmatrix} \right)^{-1} \times \begin{bmatrix} C_{31} & C_{32} & C_{36} \\ C_{41} & C_{42} & C_{46} \\ C_{51} & C_{52} & C_{56} \end{bmatrix} \right) \tag{3.9}$$

where h is the thickness of the plate. The solution series for the plate deflection in the z-direction are given below:

$$w = A_{mn} sin(\frac{m\pi x}{a}) sin(\frac{n\pi y}{b}) \ , \tag{3.10}$$

where A_{mn} are constants, m and n are integers. This case employs a simply supported orthotropic plate with the given boundary conditions:

$$\begin{aligned} w = 0, \quad & \frac{\partial w^2}{\partial x^2} + \nu_y \frac{\partial w^2}{\partial y^2} = 0 \quad at \quad x = 0, a \\ w = 0, \quad & \frac{\partial w^2}{\partial y^2} + \nu_x \frac{\partial w^2}{\partial x^2} = 0 \quad at \quad y = 0, b \end{aligned} \tag{3.11}$$

where ν_x and ν_y are the Poisson's ratios. By requiring that Eq. 3.10 be a solution of Eq. 3.8, the relation can be obtained:

$$N_x(\frac{m}{a})^4 + N_y(\frac{n}{b})^4 = \pi^2[D_{11}\frac{m}{a} + 2D_{33}\frac{mn}{ab} + D_{22}\frac{n}{b}] \tag{3.12}$$

This formulation here will be given for a general case where forces N_x and N_y may vary, but must maintain a constant ratio, β. However, the problem of interest in this study only has N_x as the axial force (Fig. 3.3), ie, $\beta = 0$.

$$N_x = \lambda, \quad N_y = \lambda\beta \tag{3.13}$$

The critical value of λ is found from the formula:

$$\lambda = \frac{\pi^2\sqrt{D_{11}D_{22}}}{b^2} \cdot \frac{\sqrt{\frac{D_{11}}{D_{22}}}(\frac{m}{c})^2 + \frac{2D_{33}}{\sqrt{D_{11}D_{22}}}n^2 + \sqrt{\frac{D_{22}}{D_{11}}}(\frac{c}{m})^2 n^4}{1 + \beta(\frac{c}{m})^2 n^2} \tag{3.14}$$

where c is the ratio between the lengths of the sides of the plate ($c = \frac{a}{b}$). The problem then consists of seeking the values of m and n which give the smallest λ and hence the critical distributed buckling load, λ_{cr}. Based on the solution of the critical distributed buckling load, the expression for the critical increase in temperature is obtained using the coefficient of thermal expansion tensor (α):

$$\Delta T_{cr} = \frac{\lambda}{\frac{12}{h^2}(D_{11} \cdot \alpha_x + D_{12} \cdot \alpha_y + D_{13} \cdot \alpha_{xy})} \tag{3.15}$$

The material properties $\boldsymbol{C}$ and $\boldsymbol{\alpha}$ are the stiffness and thermal expansion tensors respectively which are computed from the volume averaging equations. The objective of the design problem is to find the optimum values of the ODFs which maximize the critical temperature, ΔT_{cr}. Instead of solving this problem in the ODF space, it is solved in the property closure, which is generated for the important stiffness coefficients, C_{11}, C_{12} and C_{22}, which are the most sensitive to the design objective. Due to the nonlinear relation between the property closure variables, C_{11}, C_{12} and C_{22}, and design objective, ΔT_{cr}, the optimum material properties are identified with the implementation of a global sampling strategy, LHS, using 10,000 design samples, and the corresponding ODF values are solved with LP. For the sample plate dimensions of 0.25 $m \times 0.25$ $m \times 0.005$ m, the optimum material properties are identified in the property closures. The property closure is computed using both upper bound (called as $\boldsymbol{C}$ space) and lower bound (called as $\boldsymbol{C^{-1}}$ space) averaging equations for C_{11}, C_{12} and C_{22}, and the optimum solution is identified in both spaces respectively in Fig. 3.4.

After the identification of the optimum material properties in property closures the next step is to find the corresponding ODF solutions. Two different FE meshes are used to discretize the volume averaging equations to find the optimum ODF values. The first mesh uses 50 independent nodes, corresponding to 50 ODFs (called as Mesh-1) while the second one is a finer mesh with 388 ODF values (called as Mesh-2). It is observed that the problem has a unique solution, and this solution corresponds to a single crystal design. Both meshes identify the same optimum texture (single crystal optimum) for the given optimum material property values (shown in Fig. 3.5).

The optimum result provides a 23.0% increase for Mesh-1 and 28.3% increase for Mesh-2 in critical buckling temperature of the plate compared to a randomly oriented

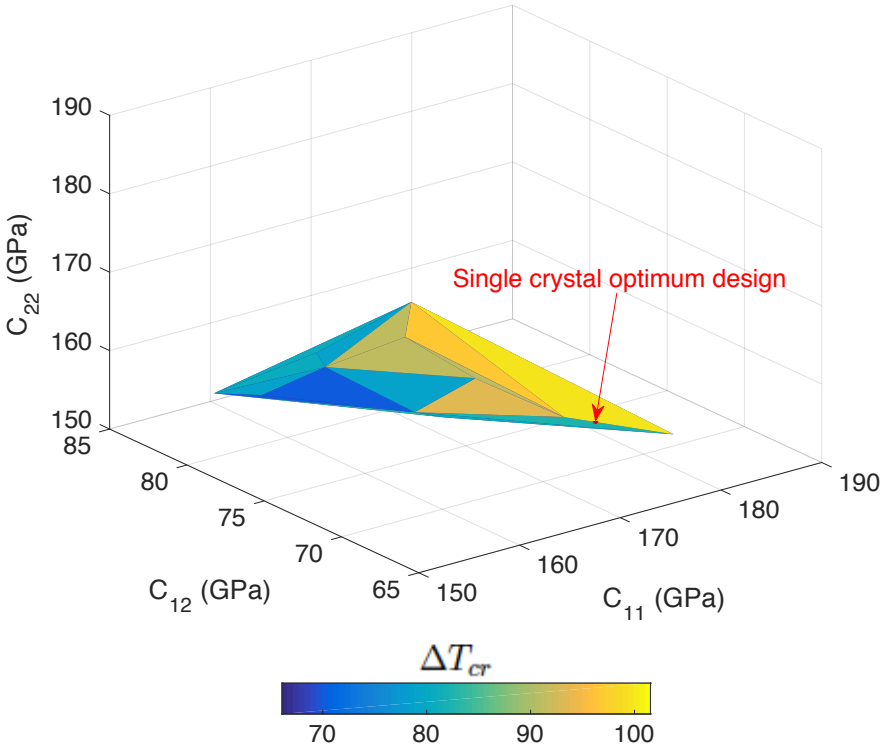

(a) C space representation

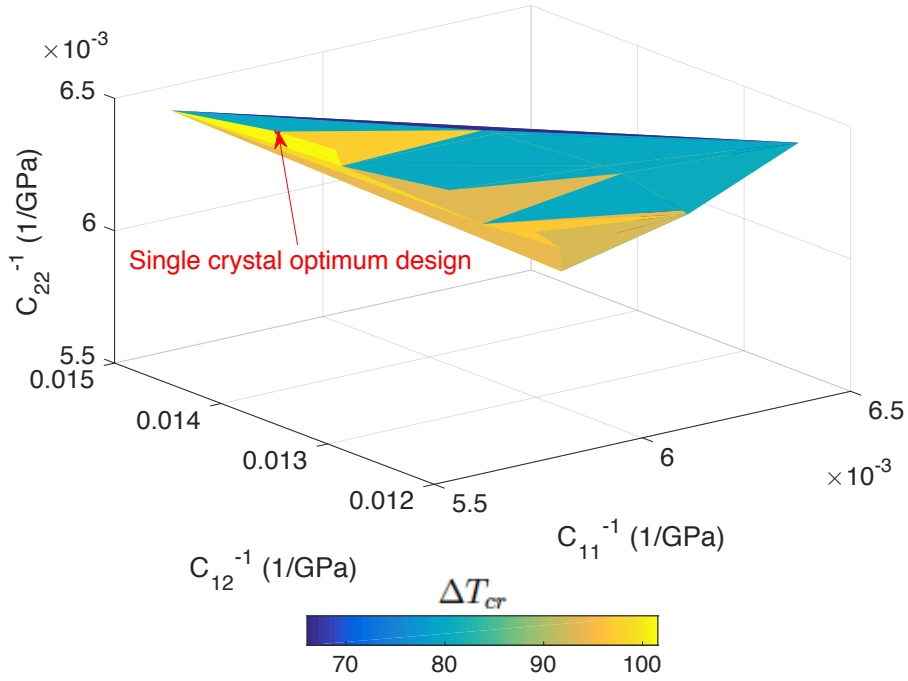

(b) C^{-1} space representation

Figure 3.4: Property closures of HCP α-Ti thermal buckling problem

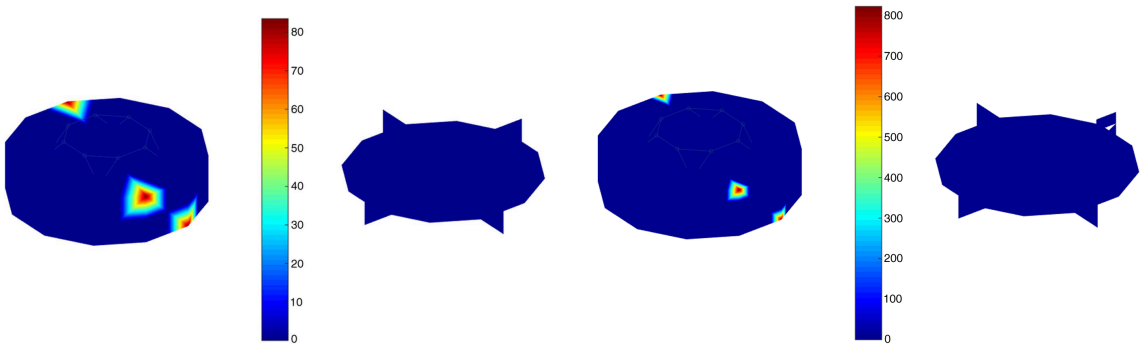

(a) Optimum ODF values (Mesh-1) (b) Optimum ODF values (Mesh-2)

Figure 3.5: Optimum ODF representation for the thermal buckling problem

design. The optimization results are shown and compared to the randomly oriented designs in Table 3.1.

Table 3.1: Results for a simply supported rectangular HCP α-Ti plate

Method	Critical temperature, ΔT_{cr}, value
average ΔT_{cr} (Mesh-1)	82.5 K
average ΔT_{cr} (Mesh-2)	82.0 K
max ΔT_{cr} (Mesh-1)	101.5 K
max ΔT_{cr} (Mesh-2)	105.2 K

The computational efficiency of the proposed optimization technique is tested with a global optimization methodology which performs a global sampling in the ODF solution space, and utilizes a genetic algorithm due to the nonlinear nature of the design problem. The genetic algorithm uses the sampling points as initial design points to start the optimization iterations. 10,000 design samples are generated with LHS, and implemented to NSGA-II. NSGA-II is selected as the optimization method since it is known as a fast and elitist genetic algorithm and it always converges to the global solution [53]. The biggest drawback of gradient based optimization algorithms is the possibility of converging to one of the local solutions instead of the global solution. Therefore they are also strictly dependent on the initialization values of the input variables. The thermal buckling design problem can potentially have many local

solutions (either single crystal solutions or combinations of polycrystal solutions) due to the highly nonlinear relation between the design criteria and variables. However, the final solution of interest should be the global optimum solution which provides the maximum ΔT_{cr} value. In order to avoid any local optimum solution, a gradient based optimization algorithm is not chosen. NSGA-II can be used for single and multi-objective optimization problems since it has the capability of finding global optimum solutions not only in single objective problems but also in multi-objective problems [61]. Thus, the same optimization framework can also be used to solve different design problems with multiple objectives. The global optimization approach identified the same single crystal optimum solution using both Mesh-1 and Mesh-2 to discretize the volume averaging relations. However, it is observed that the linear solution approach is much more efficient in terms of the computation time compared to the global approach. The computational time spent on the same platform for linear solver and global approaches are compared in Table 3.2.

Table 3.2: Computational time comparison for linear solver and global optimization approaches

Method	Mesh	Computational Time
Linear Solver	Mesh-1	$\sim$ 27 minutes
Linear Solver	Mesh-2	$\sim$ 1.5 hours
Global Optimization	Mesh-1	$\sim$ 9.5 hours
Global Optimization	Mesh-2	$\sim$ 11 hours

3.2.2 Vibration tuning for Galfenol beam

The linear solution methodology presented in the previous section is extended to the plastic properties to explore the microstructure design of a cantilevered Galfenol beam for a vibration tuning problem with yielding objective (Fig. 3.6). It is well known that thermomechanical processes (such as rolling and extrusion) may provide means to develop polycrystalline Galfenol with properties comparable to expensive

single crystals [62]. However, it has proved difficult to predict (and thus, control) the large changes in properties such as the yield strength that occurs during thermomechanical processing. For example, warm rolled and annealed specimens retain high magnetostriction but are quite brittle; whereas, cold rolled specimens have high yield strength but lose their magnetostriction [63, 64]. Consequently, it is critical to develop predictive models that can be used to optimize thermomechanical processes and control properties in the final product. Properties of Galfenol can be tailored by controlling the evolution of features of underlying polycrystalline microstructure through controlled plastic deformation. Simulation of microstructure evolution in polycrystals has been well studied in the past. The success of such approaches has allowed efficient computation of the effect of macroscopic parameters on the microstructural response. Microstructure-sensitive design methods can then employ these techniques to address inverse/optimization problems such as computation of optimal crystal orientation distributions that lead to desired elasto-plastic properties [64]. In order to control properties during processing, it is important to study the effect of mesoscale features (such as texture) on the response of these alloys.

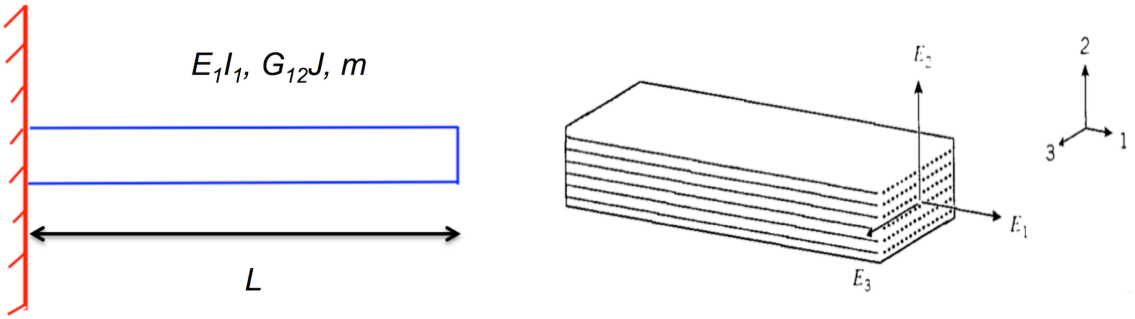

Figure 3.6: Geometric representation of Galfenol beam vibration problem

Introduction of the yielding objective to the problem provides multiple solutions, however, the vibration tuning restricts these solutions to have infinite number of directions in the solution space. The modeling of the microstructure involves the same computational operations with the previous application since the stiffness parameters

and yield stress are calculated with the volume averaging equations. The property matrix to compute the yield stress is obtained through running crystal plasticity simulations with different single crystal designs. In this problem, the number of independent ODF values is 76 at this time since Galfenol has a body centered cubic (BCC) structure. The design objective is to maximize the yield stress while the first bending and torsional natural frequencies are constrained for vibration tuning. Plastic deformation due to crystallographic slip is assumed to occur in the $< 111 >$ direction, and the possible slip planes are of the 110, 112, and 123 type. Slip hardening parameters taken to be identical for all slip systems, with values $h_0 = 500$ MPa, $s_s = 350$ MPa and $a = 2.25$ for BCC Galfenol single crystals [65, 66].

The main goal of the problem is to find the optimum microstructure design which maximizes the yield stress of the beam and satisfies the given vibration constraints for the natural frequencies. According to the coordinate system introduced in Fig. 3.6, the analytical equations of the first torsional and bending natural frequencies for an orthotropic material can be shown respectively as below:

$$\omega_{1t} = \frac{\pi}{2L}\sqrt{\frac{G_{12}J}{\rho I_p}} \tag{3.16}$$

$$\omega_{1b} = (\alpha L)^2\sqrt{\frac{E_1 I_1}{mL^4}} \quad \text{and} \quad \alpha L = 1.87510 \tag{3.17}$$

where $G_{12} = 1/S_{66}$, $E_1 = 1/S_{11}$ and $\boldsymbol{S}$ being the compliance elements ($\boldsymbol{S} = \boldsymbol{C^{-1}}$). In these formulations, J is torsion constant, ρ is density, I_p is polar inertia moment, m is unit mass, L is length of the beam and I_1 is moment of inertia along axis-1. The computation of the yield stress using upper and lower bound approaches are given in Eq. 3.18 and Eq. 3.19 respectively. The upper bound averaging is used to compute the yield stress values of the cantilever beam.

$$< \sigma_y >= \int \sigma \boldsymbol{A} dV \tag{3.18}$$

$$< \sigma_y^{-1} >= \int \sigma^{-1} \boldsymbol{A} dV \tag{3.19}$$

The mathematical formulation of the optimization problem is given below:

$$max \quad \sigma_y \tag{3.20}$$

$$subject\ to \quad \int \boldsymbol{A} dV = 1 \tag{3.21}$$

$$subject\ to \quad 21.5 \text{ Hz} \leq \omega_{1t} \leq 23.5 \text{ Hz} \tag{3.22}$$

$$subject\ to \quad 100 \text{ Hz} \leq \omega_{1b} \leq 114 \text{ Hz} \tag{3.23}$$

$$\boldsymbol{A} \geq \boldsymbol{0} \tag{3.24}$$

The optimization problem includes the unit volume constraint by definition as well as the constraints for the first natural frequencies to tune the beam vibration. To solve the problem, the length of the beam is taken as $L = 0.45$ m and the beam is considered to have a rectangular cross-section with dimensions $a = 20$ mm and $b = 3$ mm. The steps taken to optimize the microstructure are summarized below:

- The solution space is firstly reduced to a property closure which is defined for important microstructure dependent properties. The limits for microstructure dependent properties are computed using lower or upper bound approaches. In this problem, the microstructure dependent properties are E_1, G_{12} and σ_y.

- One solution of the problem should be computed to start the algorithm. The solution technique depends on either the problem is linear or not. For a linear problem, "one solution" can be computed solving an LP problem. However, sampling can be performed to find one solution of a nonlinear problem. The values of the microstructure dependent input parameters will be the same in all solutions if multiple solutions exist.

- As providing the same microstructure dependent property values, independent solution directions are computed using the null space approach of the linear solver. For a single solution problem, there is no existing solution direction since the single solution defines a point in the solution space.

- In case of having multiple solutions, these solutions are computed using "one solution" of the problem and the independent solution directions (Eq. 3.6).

The optimization problem defined for the Galfenol beam has a linear design objective but nonlinear constraints. Therefore, the one optimum solution to the problem can be found by performing a global sampling. The multiple solutions of this problem correspond to the designs having the same values for microstructure dependent input parameters (E_1 and G_{12}). The problem has 73 solution directions (76 optimization variables, 3 equations - 2 of them are for computation of E_1 and G_{12}, and 1 of them is for unit volume fraction constraint) and these solutions are polycrystal designs. The property closure graph for E_1 and G_{12} variables ($\boldsymbol{E-G}$ space) is given in Fig. 3.7. The parameters of the multiple optimum solution are given in Table 3.3. This design application is a highly constrained problem and thus neither the single crystal designs nor the random texture design can satisfy the vibration tuning design constraints. Some of the optimum microstructure designs are shown in Fig. 3.8. Since the linear solver is able to compute the independent solution directions of the Galfenol beam optimization problem, each design in Fig. 3.8 is different than the others, and has different ODF values. However, they are still providing an identical maximum yield stress value and satisfying the design constraints.

3.3 Conclusion

This chapter addresses an optimization methodology for structural problems with various macro design objectives. Optimization is performed in a reduced space, called

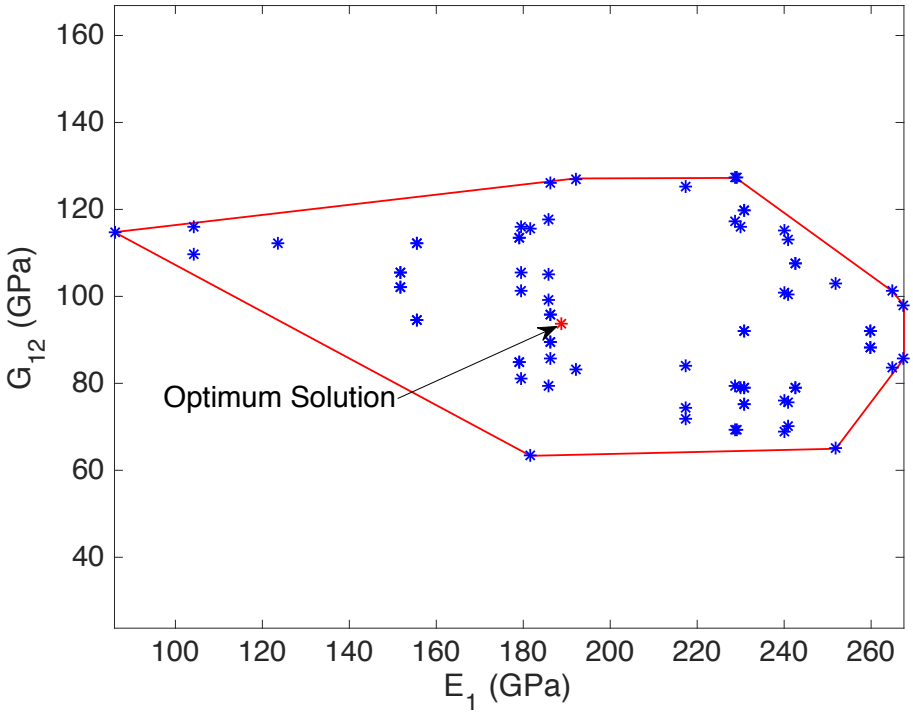

Figure 3.7: Property closure for E_1 and G_{12}

Table 3.3: Optimization results of vibration tuning problem for the Galfenol beam

Parameters	Optimum design
σ_y	308.4456 MPa
E_1	188.8229 GPa
G_{12}	93.6282 GPa

property closure, which is composed of the important material properties of the problem, and includes all possible microstructure designs. The optimum values of the material properties are identified inside the closure, and the optimum ODF values are solved with an LP solver using volume averaging equations. The multiple optimum designs are also computed with the implementation of a direct linear solver to calculate the infinite solution directions. The proposed optimization methodology is applied to two engineering design problems. The first example is a thermal buckling problem for an HCP α-Ti aircraft panel. The objective of the optimization is to maximize the critical buckling temperature. The optimization problem is solved

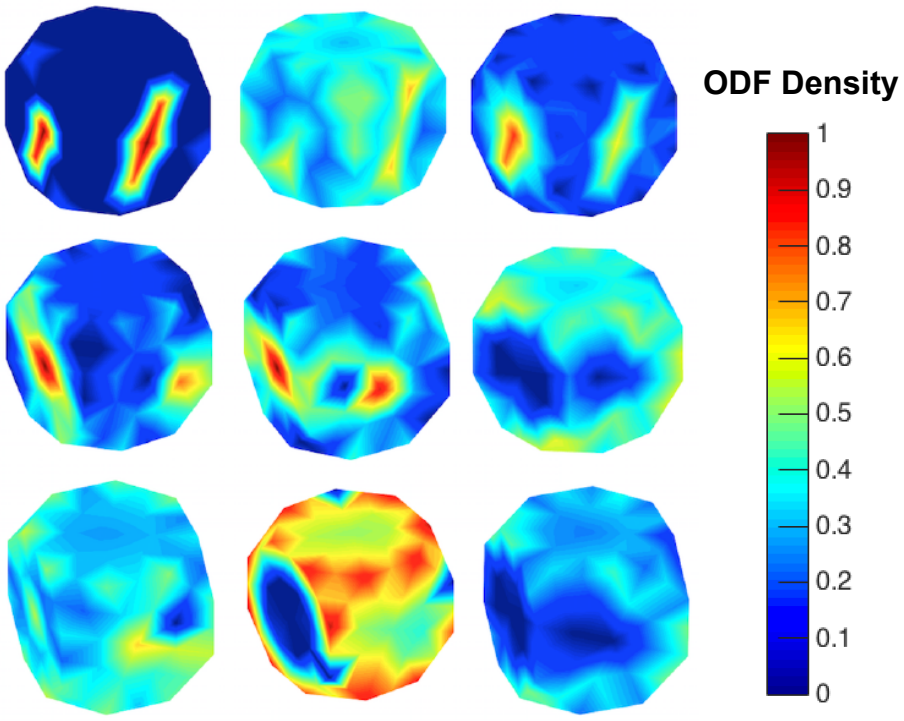

Figure 3.8: Some of the multiple optimum designs for the vibration tuning problem

in property closure which is generated for the most sensitive stiffness parameters to the objective function of the application. The optimum ODF solution is found using the LP approach, and it is observed that the thermal buckling problem has a unique solution, which is a single crystal design. The optimization is performed with two different meshes corresponding to different numbers of independent ODF variables. However, both cases provide the same optimum design. When compared to an HCP Ti plate with a randomly oriented microstructure, the optimum ODF provides a significant 23.0% and 28.3% increases with analytical solution. The numerical efficiency of the LP solution scheme is tested with a global methodology that utilizes a genetic algorithm together with a global sampling in the ODF space. The global solution is able to identify the same optimization result for both meshes, however, it is an order of magnitude slower in terms of the computational time. For the next application, the methodology is extended to plastic properties to explore design of structural problems

with a yielding objective. For this purpose, a vibration tuning problem subjected to maximum yield stress objective is optimized. Imposing a controlled vibration response to the problem leads to multiple solutions, and these solutions are computed by implementing the direct linear solution scheme in property closure. It is shown that multiple solutions can be obtained by augmenting the solutions with the null space. From among these solutions, the microstructure that can be manufactured with the most economical processing route can be identified.

CHAPTER 4

Uncertainty Quantification for Microstructural Variations

Chapter 4 focuses on quantification of experimental uncertainties and their propagation to the microstructural parameters and material properties. To this end, a set of analytical formulae that can be rapidly used to quantify uncertainties in the ODF and elastic properties is developed. The uncertainty of the X-ray PF and EBSD measurement is captured by using Ti-7Al samples, which are taken from different regions of the original ingot (the center and two sides). The probability distributions of the PFs and EBSD data are computed using the variations in the experimental samples and are found to be roughly Gaussian in nature.

The uncertainties are generally classified as aleatoric and epistemic uncertainties. The aleatoric uncertainties are irreducible variations naturally present in the system such as the uncertainties in the material properties [67]. The focus of modeling PF uncertainties is to model the aleatoric uncertainties through a probabilistic modeling approach. The uncertainties arising from the assumptions in the mathematical model are classified as epistemic uncertainty [67]. In this study, the propagation of uncertainties on the ODFs are computed using an analytical formulation taking advantage of a linear PF to ODF transformation. However, the PF inversion is non-unique and leads to 'epistemic' uncertainty due to lack of an exact solution. Therefore the un-

certainties that are introduced to the model due to the pseudo-inverse approach are not studied in this work. The microstructural variations are also modeled using the EBSD samples as a different input for uncertainties. The EBSD to ODF conversion is a one–to–one map only constrained by the level of discretization of the ODF, and thus, aleatoric uncertainties can be better quantified. The Gaussian analytical UQ model is used to compute the uncertainties in linear material properties such as the compliance parameters. An approach to identify the probability distributions of the nonlinear material properties, such as Young's modulus and shear modulus, is also proposed using the random variable transformation method. The approach is fully analytical and significantly faster than numerical approaches. The organization of the chapter is as follows. Section 4.1 addresses the experimental uncertainties quantified using the PF and EBSD samples. The mathematical formulation for the analytical UQ model is presented in Section 4.2. The results for the quantification of experimental uncertainties, and their propagation to the microstructural features and material properties are shown in Section 4.3. The summary of the chapter is given in Section 4.4.

4.1 Quantification of experimental uncertainties

The analytical UQ algorithm is first implemented to quantify the uncertainties in the experimental data using the PF and EBSD samples taken from different parts of the same Ti-7Al material during an upset-forging process. These experimental uncertainties are found to be consistent to be represented by a Gaussian distribution. The variations in the microstructure features and material properties due to the experimental uncertainties are identified by implementing the analytical UQ algorithm.

4.1.1 Uncertainties in PF data

This section discusses quantification of uncertainties introduced to the PFs due to the variations in the experimental samples. Three different samples of Ti-7Al alloy were taken from different regions of a beta forged ingot, which created variability in the resulting microstructure due to the inhomogeneity of the forging process. These samples were subject to the same thermomechanical process. All three samples were compressed to 20% height reduction at room temperature, and annealed for 72 hours at 1073K. The compression direction was also the longitudinal direction of the forging. The microstructures were fully recrystallized at these conditions. Scans were taken from different regions of the processed samples. A total of hundred PFs ($\boldsymbol{h} = < 001 >$, $< 100 >$ and $< 101 >$) were generated from these scans for statistical analysis. Representative samples for the PFs are illustrated in Fig. 4.1, and indicate a weakly basal texture. We consider $m = 221$ pole densities for each PF. Since three PFs were sampled, a total of 663 pole density values in total were used in the UQ model. The HCP fundamental region discretized with 50 independent nodes, as shown previously in Fig. 2.1, is used to model the ODF.

The variability in the pole density function $P(\boldsymbol{h}, y_i)$ at each point y_i for these three PFs are computed from 100 different samples drawn from the specimen (generated from the input samples). The histograms of these variations are plotted and it is found that the variability in $P(\boldsymbol{h}, y_i)$ can be modeled using Gaussian features as shown in Fig. 4.2. Since the experimental samples show that the variations in the PFs are consistent with Gaussian distribution, the solution approach depends on two steps. The first being to prove that the variations in the ODFs are also consistent with Gaussian distribution. The second step is to compute the mean value and standard deviation of the joint multivariate distributions for the ODFs. Once the distribution type and statistical quantities are determined the variation in the output variables can be identified.

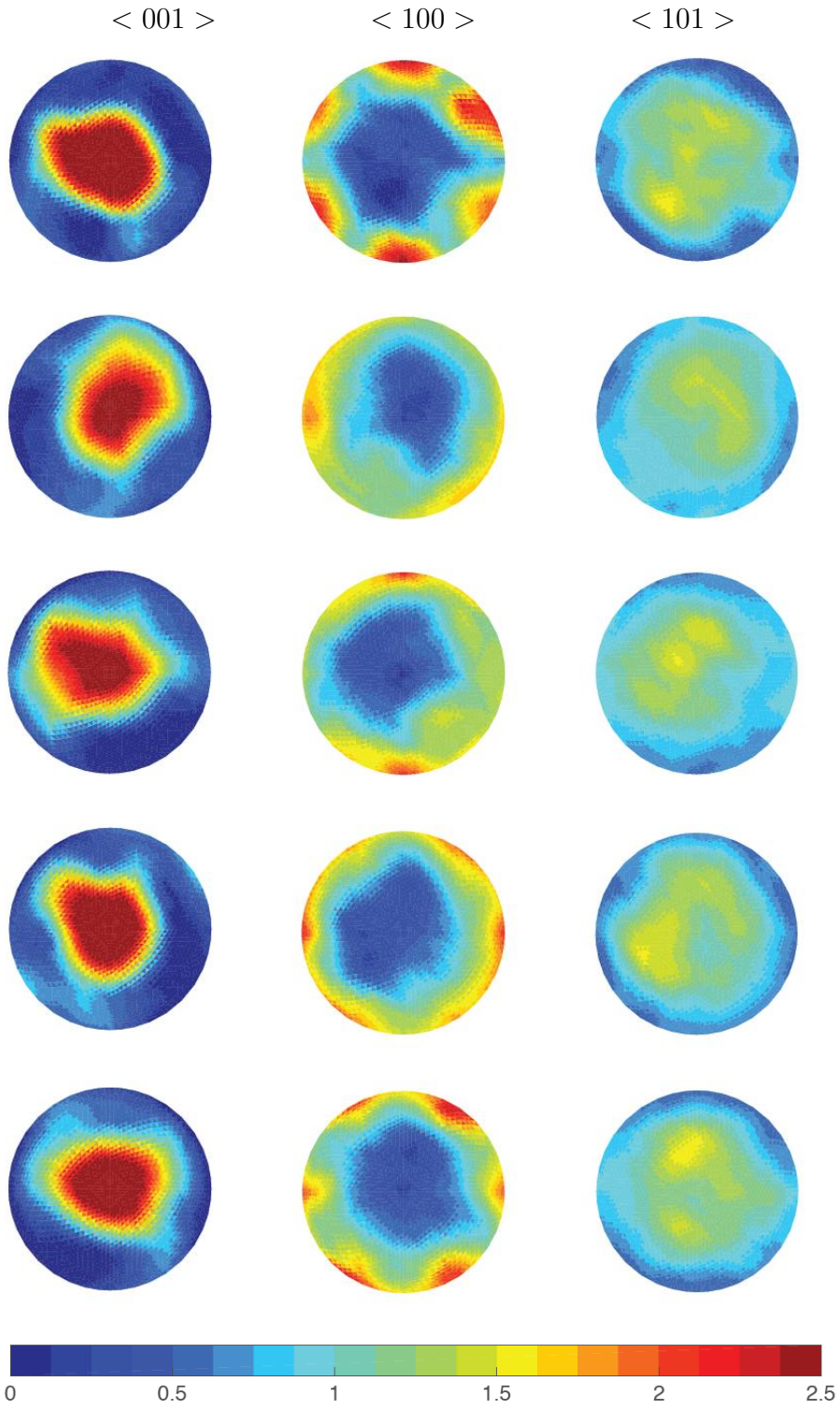

Figure 4.1: Representative $< 001 >$, $< 100 >$ and $< 101 >$ PF samples

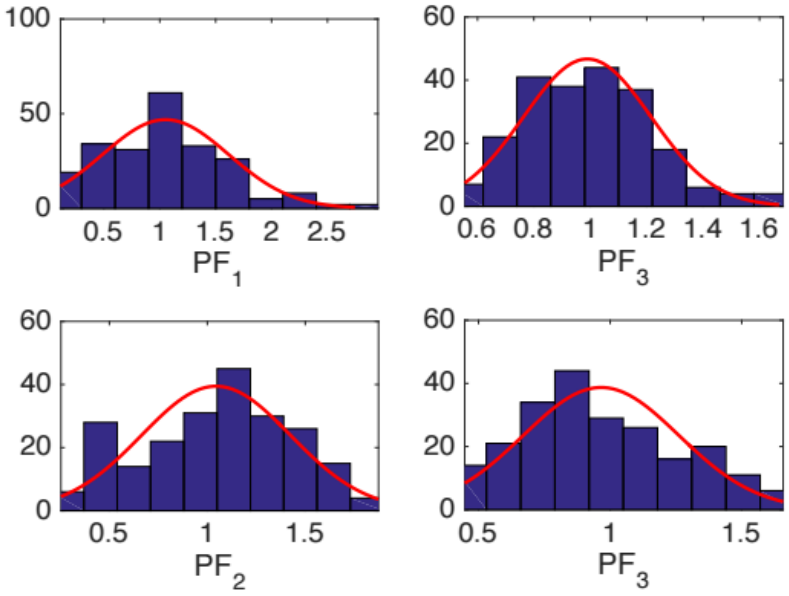

Figure 4.2: Probability histograms of a few representative pole density values ($P(\boldsymbol{h}, y_i)$). The labels for PF1, PF2 and PF3 indicate the PFs $\boldsymbol{h} =< 001 >, < 010 >$ and $< 101 >$ respectively from which these densities are obtained.

To show the statistical features, the mean values and coefficient of variations (ratio of standard deviation to the mean value) of the PFs are depicted in Fig. 4.3 and Fig. 4.4 respectively.

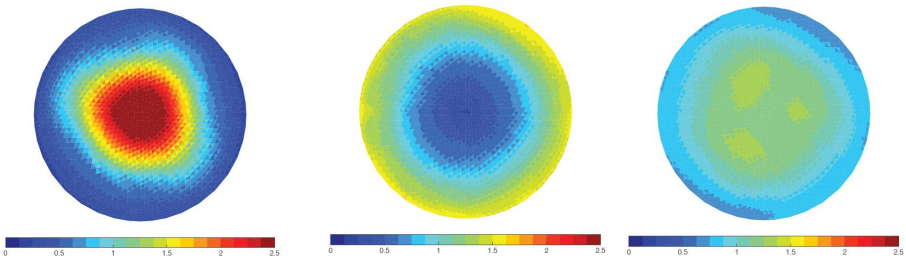

$< 001 >$ $< 100 >$ $< 101 >$

Figure 4.3: Mean values of the PFs

The experimentally obtained PF for a particular diffraction plane unit normal $\boldsymbol{h}$ contains the pole density function $P(\boldsymbol{h}, y_i)$ measured at locations $y_1, y_2, ..., y_q$ on a unit sphere. The value of $P(\boldsymbol{h}, y_i)$ at location y_i can be computed from the ODF ($\boldsymbol{A}$)

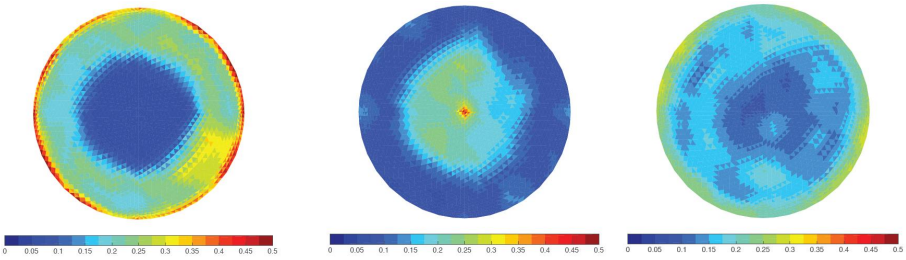

$< 001 >$ $< 100 >$ $< 101 >$

Figure 4.4: Coefficient of variations for the PFs

using a single linear equation based on the algorithm of Barton et al. [68]:

$$P(\boldsymbol{h}, y_i) = \sum_{j=1}^{k} M_{ij} A_j \tag{4.1}$$

where M_{ij} are the values from a known system matrix $\boldsymbol{M}$. One such equation can be written for each of the m points in a PF. This set of equations can be combined with a similar set of equations for n other PFs with different diffraction normals $\boldsymbol{h}$. This leads to a global system of equations $\boldsymbol{P} = \boldsymbol{MA}$. Here, $\boldsymbol{P}$ is a column vector of size $m \times n$, $\boldsymbol{M}$ is a matrix of size $(mn) \times (k)$ and the ODF, $\boldsymbol{A}$, is a column vector of size k containing the volume densities of k independent nodes. In order to account for the normalization constraint $\sum_{i=1}^{k} q_i A_i = 1$, the overall system $\boldsymbol{P} = \boldsymbol{MA}$ is adjusted such that $M_{ij} = M_{ij} - \frac{M_{ik} q_j}{q_k}$ for $j = 1, .., k-1$ and $P_i = P_i - \frac{M_{ik}}{q_k}$.

The system of equations is over–determined (i.e. more PF data as compared to the unknown ODF values) and direct inversion is not possible. Instead of following Barton et al. [68], the ODF is retrieved from the experimental PFs using least squares minimization as follows:

$$\boldsymbol{A} = \boldsymbol{CP} \tag{4.2}$$

where the coefficient matrix, $\boldsymbol{C} = (\boldsymbol{M^T M})^{-1} \boldsymbol{M^T}$, is the pseudo–inverse. The PF inversion equation is not unique. This equation defines an over-determined system and therefore multiple ODF solutions are possible. The fundamental idea that is

implemented here is to compute a set of ODFs, which can provide a PF data as close as to the experimental PF input. A popular way in the material community to compute these ODFs is to apply the least squares method, which is the same with the pseudo-inverse approach in this study. The least squares approach for computing the ODFs from the PF data was presented in more details by Barton et. al [68].

4.1.2 Uncertainties in EBSD data

In this work, the experimental EBSD scans for a Ti-7Al alloy are also considered to determine the uncertainties in ODF values and material properties. The variabilities in the ODFs are computed from 150 different EBSD samples drawn from the specimen. Some of the example EBSD samples are shown in Fig. 4.5. The ODFs are calculated from the EBSD data by binning the values at integration points. The ODF values at the independent nodal points are then obtained using the linear relation between nodal point and integration point ODFs. Readers are referred to Eq. 2.5 and Eq. 2.6 in Section 2.1.1 for computation of independent nodal point ODFs from the integration point ODFs.

The orientations from the EBSD data are binned pixel–by–pixel to the element containing the orientation, specifically to the integration point in the element. After binning is complete, the ODF value (A_i^{int}) at the integration point in an element i contains the total number of pixels in the EBSD image that have orientations lying within the element. The data is then normalized by $\boldsymbol{q}^{\boldsymbol{int^T}}\boldsymbol{A}^{\boldsymbol{int}}$. Let matrix $\boldsymbol{T}$ convert the integration point values $\boldsymbol{A}^{\boldsymbol{int}}$ to the independent nodal values $\boldsymbol{A}^{\boldsymbol{node}}$, i.e., $\boldsymbol{A}^{\boldsymbol{node}} = \boldsymbol{T}\boldsymbol{A}^{\boldsymbol{int}}$. Using one integration point, this matrix is defined as $T_{ij} = \delta_{ij}/f$ where δ_{ij} is one if node i (or its symmetric equivalent) is a vertex of element j and zero otherwise. The factor f is the number of elements with node i (or symmetric equivalent) as one of its vertices. This matrix is always positive and thus, $\boldsymbol{A}^{\boldsymbol{node}} \geq \boldsymbol{0}$. Vector containing the values of the ODF at $k-1$ independent nodal points is hereafter

referred to as $\boldsymbol{A}$. In order to account for the normalization constraint, the property vector $\boldsymbol{p}$ is adjusted such that $p_i = p_i - \frac{p_k q_i}{q_k}$ for $i = 1, .., k-1$ and the property is rewritten as $< \chi >= \sum_{i=1}^{k-1} p_i A_i + \frac{p_k}{q_k} = \boldsymbol{p^T A} + r$. Other properties may be derived from $< \chi >$. For example, the elastic modulus can be written as $E = \frac{1}{<S_{11}>}$ where $< S_{11} >$ is a component of the compliance matrix ($\boldsymbol{S}$) computed from the lower bound relation $< S >= \int_R S(\boldsymbol{r}) A(\boldsymbol{r}) dv$.

The histograms of the experimental variations are plotted and it is found that the variability in the ODFs can be modeled with a bell–shaped distribution - e.g. of the Gaussian type as shown in Fig. 4.6 for some of the integration point ODFs. The skewness of the integration point probability distributions are also calculated, and shown in Fig. 4.7 that they vary around zero, which is the skewness value of the Gaussian distribution. In Fig. 4.7, most of the skewness values are very close to zero, and the maximum absolute difference with the Gaussian skewness value is only around 0.15. This result also proves that the ODFs can be modeled with a Gaussian distribution since it shows that the probability distributions of the integration point ODFs have more of a symmetric characteristic rather than demonstrating a dominant positively or negatively skewed feature. The selection of the Gaussian distribution to model the integration point ODFs is finally checked with probability-probability (P-P) and quantile-quantile (Q-Q) plots [69]. The P-P plot depicts two cumulative distribution function (CDF) against each other, it is also being used as another measure to compare the skewness of different distributions. Here, the P-P plot is shown in Fig. 4.8 to compare the CDFs of the experimental samples and the analytical assumption with Gaussian distribution. The Q-Q plot, on the other hand, is a graphical technique to compare the probability distributions by plotting their quantiles against each other. Fig. 4.8 shows the P-P and Q-Q plots of the experimental samples and the Gaussian assumption for some of the example integration point ODFs (The other ODF distributions also represent very similar features). All the tests illustrated in

Fig. 4.6, 4.7 and 4.8 show that the variations of the integration point ODFs in the experimental samples agree well with a Gaussian distribution assumption.

The Gaussian approximation allows for development of analytical expressions while considering correlations between the various ODF values. The solution includes two basic steps: The first step is to find the statistical features of linear material properties, and the second step is to find the probability distributions of non-linear material properties using transformation of random variables. The solution procedure is also illustrated in Fig. 4.9.

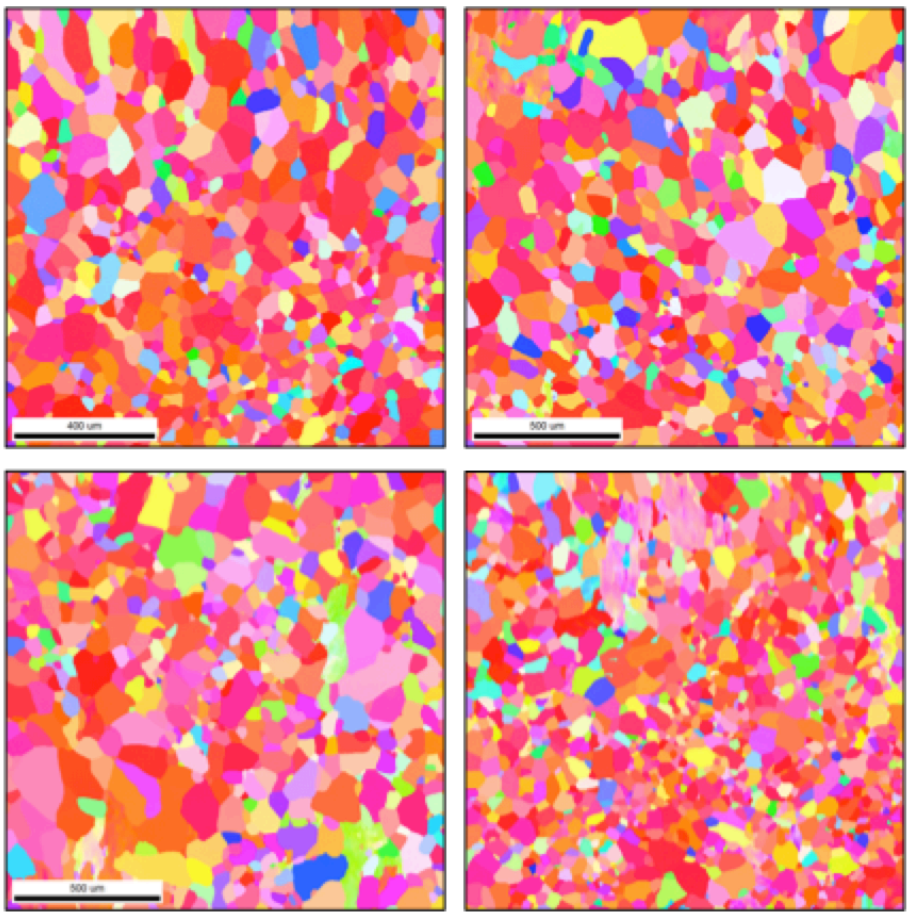

Figure 4.5: Some example EBSD samples

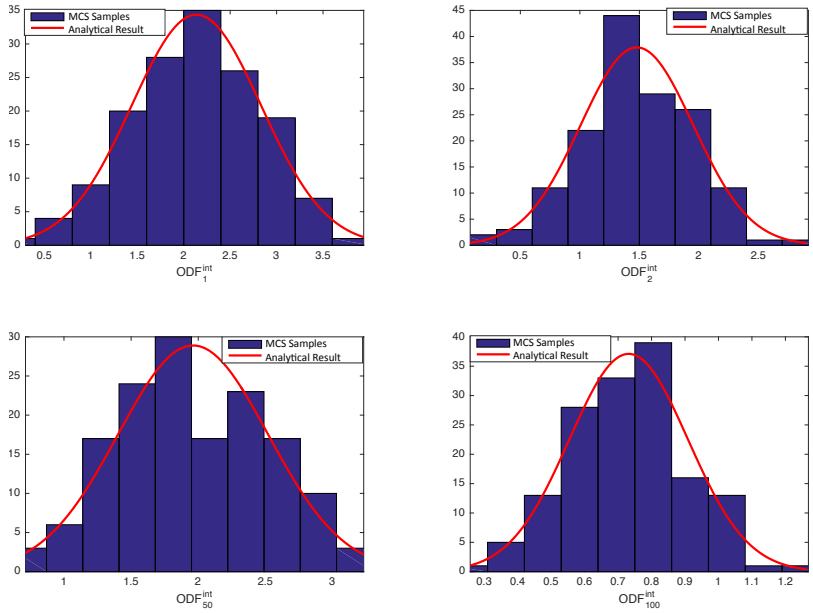

Figure 4.6: The ODFs at the integration points agree with the Gaussian distribution

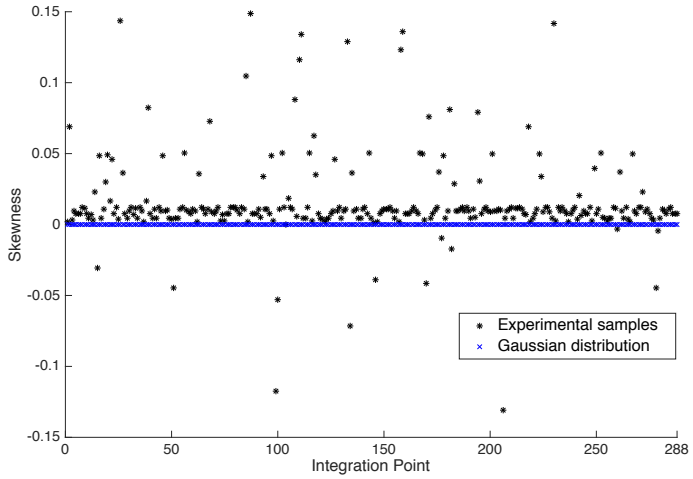

Figure 4.7: The skewness of the integration point ODF variations.

4.2 Analytical modeling for UQ

An analytical UQ technique is developed to capture the uncertainties in the ODF values, and linear and nonlinear material properties. Since the experimental data is represented with a Gaussian distribution the linear transformation feature of the distribution is implemented to calculate the probability distributions of the nodal point

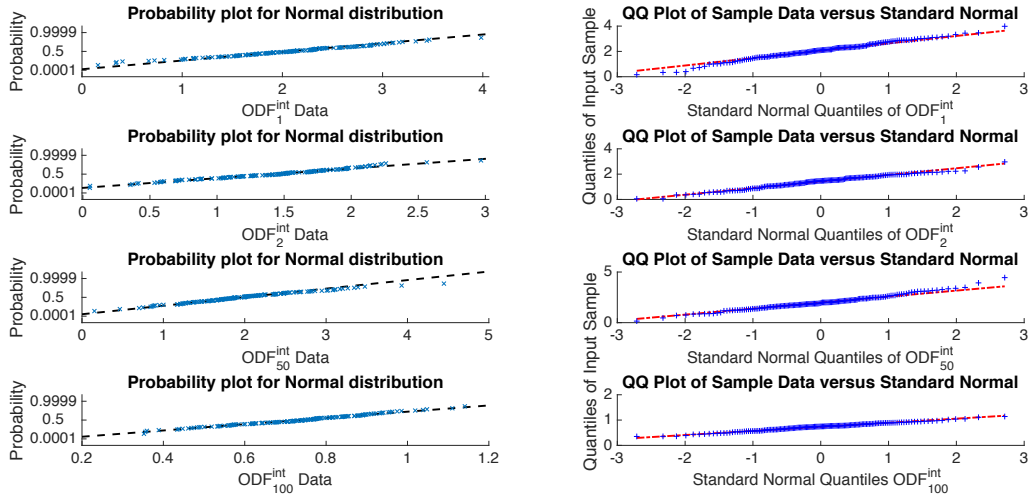

Figure 4.8: The P-P and Q-Q plots of the experimental samples and Gaussian assumption

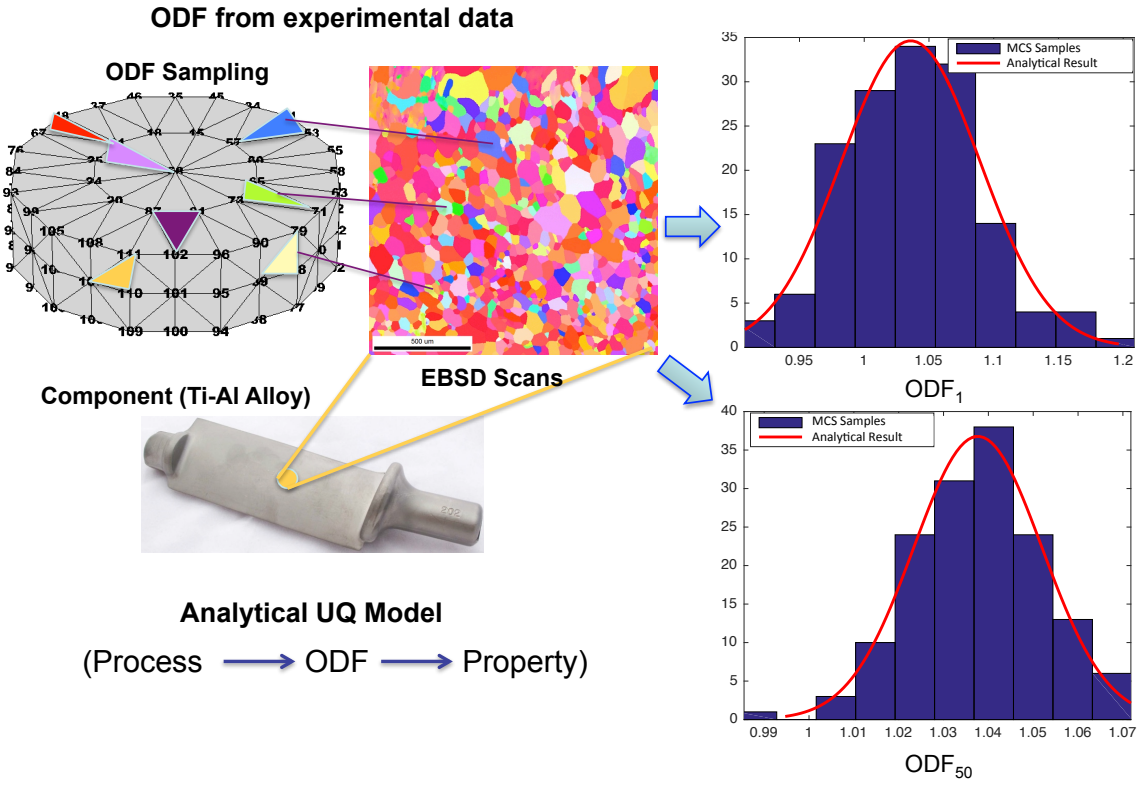

Figure 4.9: The solution procedure for UQ using EBSD sample data

ODFs due to the linear relations between the PF data and nodal point ODFs (when modeling PF uncertainties), and integration point ODFs and nodal point ODFs (when modeling EBSD uncertainties). The modeling of uncertainties in linear material properties has the same feature since these properties can be calculated with volume averaging equations which are linear in terms of the nodal point ODF values. The UQ of nonlinear material properties implements another analytical technique, transformation of random variables, to compute the probability density function (PDF) of the output variables when the PDF of input variables is given.

4.2.1 General features of Gaussian distributed correlated random variables

Assume a d-dimensional multivariate normal distribution: $\boldsymbol{X} \sim \boldsymbol{N_d(\mu, \Sigma)}$, where vector of mean values $\boldsymbol{\mu} = (\mu_1, ..., \mu_d)^T = E[\boldsymbol{X}]$ and covariance matrix $\Sigma_{jk} = cov(X_j, X_k) = E[(X_j - \mu_j)(X_k - \mu_k)], \quad j, k = 1, ..., d$ are known. The characteristic function for the Gaussian distributed variable, $\boldsymbol{X}$, is given by [70]:

$$\psi_X(t) = E[exp(i\boldsymbol{t^T X})] = exp(i\boldsymbol{t^T \mu_X} - \frac{1}{2}\boldsymbol{t^T \Sigma_X t}) = exp(i\sum_{j=1}^{d} t_j\mu_j - \frac{1}{2}\sum_{j=1}^{d}\sum_{k=1}^{d} t_j t_k \Sigma_{jk}) \tag{4.3}$$

For a one-dimensional Gaussian variable, $Y \sim N_1(\mu_y, {\sigma_y}^2)$:

$$\psi_Y(t) = exp(it^T\mu_y - \frac{1}{2}t^2{\sigma_y}^2) \tag{4.4}$$

Now define a new random variable,

$$Z = \boldsymbol{a^T X} = \sum_{j=1}^{d} a_j X_j \tag{4.5}$$

where $\boldsymbol{a}$ is a constant column vector. The characteristic function for Z is given

by:

$$\psi_Z(t) = E[exp(itZ)] = E[exp(it\boldsymbol{a^T X})] = \psi_X(t\boldsymbol{a}) \tag{4.6}$$

$$\psi_Z(t) = exp(it\sum_{j=1}^{d} a_j\mu_j - \frac{1}{2}t^2\sum_{j=1}^{d}\sum_{k=1}^{d} a_j a_k \Sigma_{jk}) \tag{4.7}$$

The comparison of this new characteristic function, $\psi_Z(t)$, with the characteristic function for the one-dimensional variable, $\psi_Y(t)$, shows that they are almost equivalent, except μ_y is replaced by $\mu_z = \sum_{j=1}^{d} a_j\mu_j = \boldsymbol{a^T\mu_X}$, and ${\sigma_y}^2$ is replaced by ${\sigma_z}^2 = \sum_{j=1}^{d}\sum_{k=1}^{d} a_j a_k \Sigma_{jk} = \boldsymbol{a^T\Sigma_X a}$. Since the characteristic function of $\boldsymbol{Z}$ is equivalent to the characteristic function of Y, the distributions must also be equal. Therefore, $\boldsymbol{Z}$ is also Gaussian distributed. The above derivation can be generalized to a matrix–vector product, $\boldsymbol{Z = AX}$. The characteristic function for vector $\boldsymbol{Z}$ is given by:

$$\psi_Z(t) = E[exp(it^T\boldsymbol{Z})] = E[exp(it^T\boldsymbol{AX})] = \psi_X(\boldsymbol{A}^T t) \tag{4.8}$$

$$\psi_Z(t) = exp(i\boldsymbol{t^T A\mu_X} - \frac{1}{2}\boldsymbol{t^T A\Sigma_X A^T t}) \tag{4.9}$$

Here, the mean and covariance of vector $\boldsymbol{Z}$ is given by:

$$\boldsymbol{\mu_Z = A\mu_X} \tag{4.10}$$

$$\boldsymbol{\Sigma_Z = A\Sigma_X A^T} \tag{4.11}$$

4.2.2 UQ in ODF values using Gaussian distributed correlated variables

The statistical parameters of the ODFs can be identified using the features of Gaussian distribution with the PF uncertainties. From Eq. 4.2, the ODF is retrieved

from the equation $\boldsymbol{A} = \boldsymbol{CP}$. From the known mean vector ($\boldsymbol{\mu_P}$) and covariance matrix ($\boldsymbol{\Sigma_P}$) of the pole density vector $\boldsymbol{P}$ obtained from experiments, the mean and covariance matrix of the ODF $\boldsymbol{A}$ can be computed using Eq. 4.10 and Eq. 4.11 as $\boldsymbol{\mu_A} = \boldsymbol{C\mu_P}$ and $\boldsymbol{\Sigma_A} = \boldsymbol{C\Sigma_P C^T}$. These expressions give the mean values and covariance matrix of the first $k-1$ independent ODF values. The PDF of the k^{th} ODF value is then computed using the normalization constraint. Knowing the volume density of the first $k-1$ nodes, the volume density of the k^{th} node can be found as:

$$A_k = \sum_{i=1}^{k-1} c_i A_i + \frac{1}{q_k}, \text{ where } c_i = -\frac{q_i}{q_k} \tag{4.12}$$

This is similar to the linear equation (Eq. 4.5) with an added constant, and mean and variances can be obtained as $\mu_k = \boldsymbol{c^T \mu_A} + \frac{1}{q_k}$ and ${\sigma_k}^2 = \boldsymbol{c^T \Sigma_A c}$ respectively.

Remark: The full covariance matrix $\boldsymbol{\Sigma_A^*}$ of k independent nodes of the ODF can also be computed as a postprocessing step, but is not required for property analysis. The covariance matrix of the first $k-1$ independent ODF values $\boldsymbol{\Sigma_A}$ is a $(k-1)\times(k-1)$ square matrix. The full covariance matrix is a $k \times k$ square matrix given by:

$$\boldsymbol{\Sigma_A^*} = \begin{bmatrix} \boldsymbol{\Sigma_A} & \boldsymbol{S} \\ \boldsymbol{S}^T & {\sigma_k}^2 \end{bmatrix}$$

where, $\boldsymbol{S}$ is a column vector whose values are given by:

$$S_i = -\frac{1}{q_k} \sum_{j=1}^{k-1} q_j (\Sigma_A)_{ij} \tag{4.13}$$

The Gaussian approach, which can model all k correlated ODF nodal variables, is also used to represent the uncertainties in EBSD data. The Gaussian approach presented here can be modified accordingly to represent the variations in the nodal point ODFs since the variations in the integration point ODFs can directly be identified through the EBSD samples.

$$\boldsymbol{\mu_A} = \boldsymbol{T^*}\boldsymbol{\mu_{A^{int}}} \tag{4.14}$$

$$\boldsymbol{\Sigma_A} = \boldsymbol{T^*}\boldsymbol{\Sigma_{A^{int}}}\boldsymbol{T^{*T}} \tag{4.15}$$

where $\boldsymbol{\mu_A}$ and $\boldsymbol{\Sigma_A}$ are the mean and covariance of the ODF at $k-1$ independent nodal points, $\boldsymbol{T^*}$ is matrix $\boldsymbol{T}$ with the first $k-1$ rows/columns included. $\boldsymbol{\mu_{A^{int}}}$ and $\boldsymbol{\Sigma_{A^{int}}}$ are the mean and covariance of the ODFs at the integration points. The mean and variance of the k^{th} independent node may be computed from the mean and covariance of the $k-1$ nodes using the same methodology as discussed for the PF uncertainties.

4.2.3 UQ in linear properties using Gaussian distributed correlated variables

The next step is to identify the probability distributions of the material properties. Elements of the compliance matrix can be computed using an averaged linear relation in terms of the ODFs: $< S_{11} >= \int S_{11}\boldsymbol{A}dV$ which can also be written in the form $S_{11} = \boldsymbol{p^T A} + r$ (r term comes due to contribution of the k^{th} ODF). Since the ODFs are already identified as Gaussian distributed, these linear relations imply that the probability distributions of compliance components, such as $< S_{11} >$ and $< S_{66} >$, are also Gaussian, and their mean values and standard deviations can be computed as $\mu_{S_{11}} = \boldsymbol{p^T}\boldsymbol{\mu_A} + r$, and ${\sigma_{S_{11}}}^2 = \boldsymbol{p^T}\boldsymbol{\Sigma_A}\boldsymbol{p}$ using Eq. 4.7.

4.2.4 UQ in nonlinear properties using transformation of random variables

When the representation of a property is not linear in the ODF, the PDF can still be computed using transformation of random variables. Given the input parameter,

x, and the output parameter, y, it is assumed that the relation between x and y can be identified using $y = h(x)$, and can be inverted as $x = u(y)$. This method computes a Jacobian value, J, based on this explicit relation (where $J = du/dy$), and finds the PDF of the output variable as a product of input PDF and the Jacobian. Eq. 4.16 shows the computation of output PDF:

$$f_y(y) = f_x[u(y)] \times |J| \tag{4.16}$$

where f_x and f_y are the PDFs of input and output variables respectively. Since the input PDF, f_x, and inverted function, $u(y)$ are already known, the output PDF, f_y, can be computed using this method. Then, the expected value, $E[y]$, and variance, $Var(y)$, of the output parameter can be calculated using Eq. 4.17 and 4.18 respectively [71]:

$$E[y] = \int_{y_{min}}^{y_{max}} y f_y(y) dy \tag{4.17}$$

$$Var(y) = E[(y - E[y])^2] \tag{4.18}$$

where y_{min} and y_{max} are the minimum and maximum values of the output variable, y, can take. These values can be computed since the explicit relation, $y = h(x)$, is known. The approach is first demonstrated in the next section for computing the PDF of the homogenized elastic modulus $E_1 = 1/S_{11}$ and shear modulus $G_{12} = 1/S_{66}$. The same method is then used to compute the PDFs of the first torsion and bending natural frequencies of a cantilever beam. The cantilever beam problem is the same as the problem in Chapter 3 and Chapter 6. However, this time the beam material is a Ti-7Al alloy instead of Galfenol. The same geometrical properties of the beam are considered for the analysis.

4.3 UQ in microstructural parameters and material properties

This section discusses the UQ results for ODF parameters and material properties given the input experimental uncertainties quantified with the PF and EBSD samples.

4.3.1 Quantification and propagation of experimental uncertainties using PF data

Using method of characteristic functions, the mean values and standard deviations of the ODFs are identified. The probability distributions of the 49 ODF values are solved first, and then the probability distribution of the last ODF, ODF_{50}, is computed by using the normalization constraint. The histograms for some of the ODFs, including the last ODF (ODF_{50}) are shown in Fig. 4.10. ODF_{50}, in particular, has a low standard deviation due to the strict normalization constraint. The statistical properties of the ODF distributions (mean values, standard deviations and coefficient of variations of the ODFs) are plotted on the mesh in Fig. 4.11. It is observed that some of the ODF values with high mean values also have higher standard deviations. Thus, the coefficient of variation (ratio of standard deviation to mean) of the ODFs is more uniform than the mean or standard deviations as indicated by Fig. 4.11.

The uncertainties in the ODFs and material properties are also quantified using MCS to verify the proposed analytical model. In this approach, the aforementioned 100 experimental PF sets are used and the ODFs are directly computed from each set (using Eq. 4.2 and the normalization constraint). Then, 100 sets of material properties (S_{11}, E_1, etc.) are computed from these ODFs using the homogenization relations. Histograms of these ODFs and properties are directly compared to the Gaussian analytical solution. The analytical solution is much faster, the solution times are 7 seconds for analytical model and 15 minutes for MCS on the same com-

putational platform. However, MCS provides exact solutions since no Gaussian PDF approximations are made, and they use the exact experimental data samples. The MCS results for the probability distributions of ODF_{50}, S_{11}, S_{66}, E_1 and G_{12} are shown together with the analytical model results in Fig. 4.10, 4.12 and 4.13.

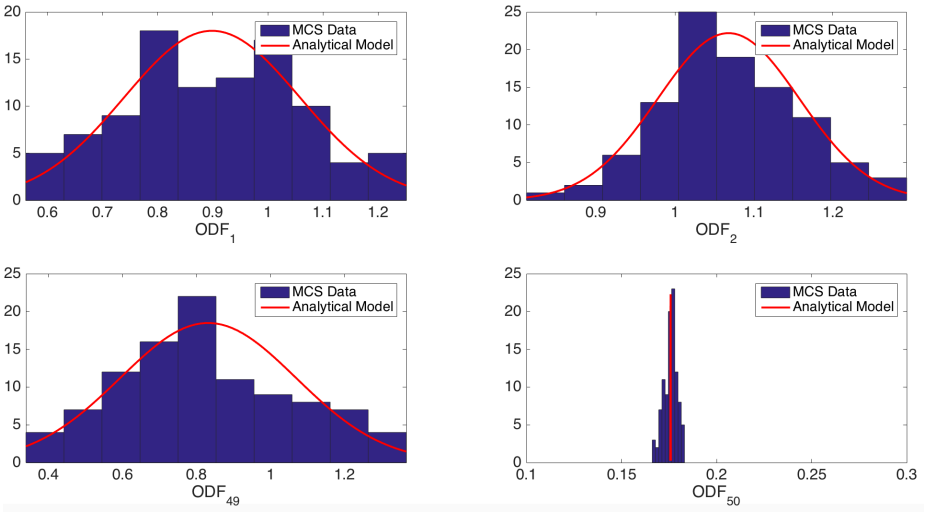

Figure 4.10: Probability histograms of the ODFs

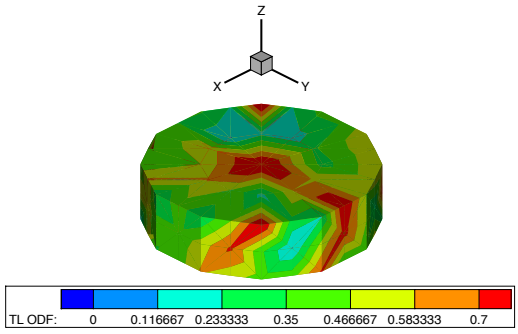

(a) Difference of mean values and standard deviations of the ODFs

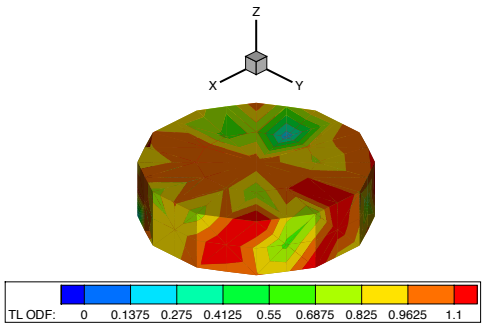

(b) Mean values of the ODFs

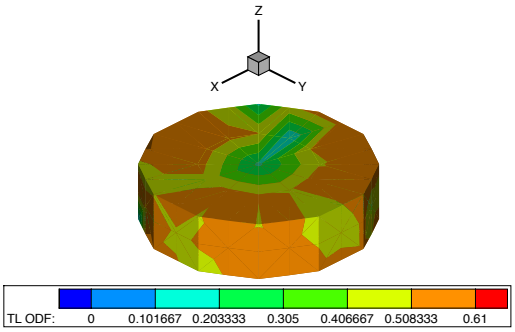

(c) Standard deviations of the ODFs

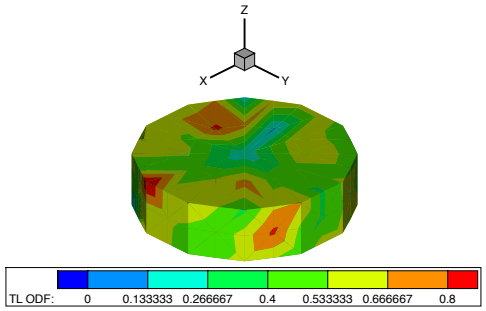

(d) Coefficient of variations of the ODFs

Figure 4.11: Statistical features of the ODF probability distributions

Knowing the uncertainty in the ODF, the uncertainties in the homogenized properties are quantified. The compliance elements, S_{11} and S_{66}, are computed using the lower bound approximation. The elastic constants of the single crystals are considered for 750 ^{o}C [72], and the values are taken as: $C_{11} = 125.3$ GPa, $C_{12} = 99.4$ GPa, $C_{13} = 68.8$ GPa, $C_{33} = 154.5$ GPa and $C_{55} = 31.6$ GPa. The mean values and variances are computed using method of characteristic functions due to the linear relations of compliance elements with the ODFs. The probability distributions of S_{11} and S_{66} are shown in Fig. 4.12.

The next step computes the PDFs of the in-plane Young's Modulus, E_1, and shear modulus, G_{12}. Even though the probability distributions of S_{11} and S_{66} are identified as Gaussian, the probability distributions of E_1 and G_{12} are not Gaussian due to

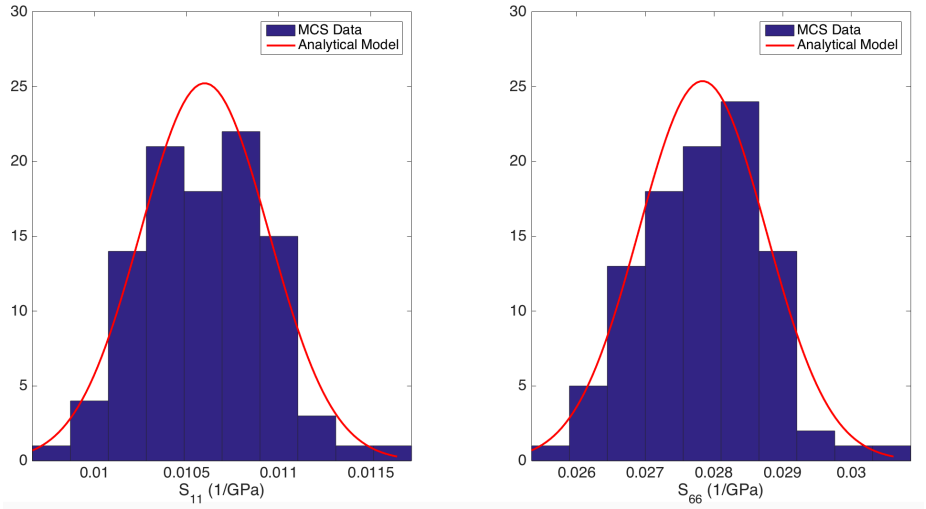

Figure 4.12: Probability histograms of S_{11} and S_{66}

their inverse relations ($E_1 = 1/S_{11}$ and $G_{12} = 1/S_{66}$). The PDFs of E_1 and G_{12} are determined using transformation of random variables (Eq. 4.16) in Section 4.2.4. To compute these PDFs, the transformation function can be identified as $u(y) = 1/y$ according to relations between E_1 and S_{11}, and G_{12} and S_{66}. Then the expected values and the variances are calculated using Eq. 4.17 and 4.18. The probability distributions of E_1 and G_{12} are shown in Fig. 4.13.

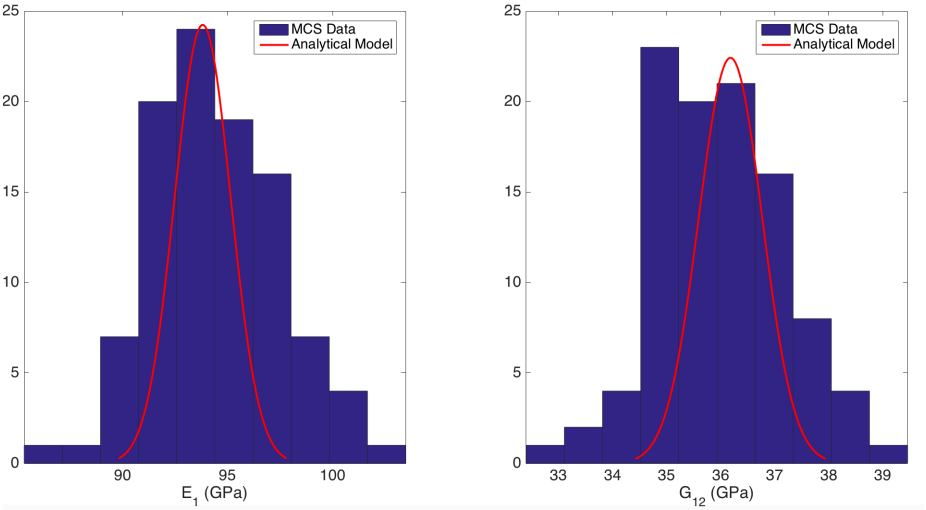

Figure 4.13: Probability histograms of E_1 and G_{12}

The MCS and analytical model results shown in Fig. 4.10, Fig. 4.12 and Fig. 4.13 indicate that the UQ with the analytical approach provides an accurate representation for microstructural variations and property uncertainties. However, the variances in the MCS results are higher compared to the results with the analytical algorithm. This is because the first $k-1$ ODFs are modeled as uncorrelated variables in this section. The variance values are expected to converge to the MCS results when all the ODFs are modeled as correlated variables as presented in Section 4.3.2.

4.3.2 Quantification and propagation of experimental uncertainties using EBSD data

A total of 150 small scans are generated from the EBSD experimental data to represent the statistical features of the ODFs sufficiently. Using the experimental EBSD scans the ODFs are obtained by binning to the elements. Using multiple scan data, a histogram of ODF values at the integration points is obtained. The histograms are found to be consistent with a Gaussian distribution. The mean and covariance of the ODFs at the 49 independent nodes are then computed applying the Gaussian approach. The probability distribution of the last ODF, ODF_{50}, is computed by using the volume fraction normalization constraint. The histograms for some of the ODFs, including the last ODF (ODF_{50}) are shown in Fig. 4.14. ODF_{50}, in particular, has again a lower standard deviation due to the normalization constraint. The statistical properties of the ODF distributions (mean values, standard deviations and coefficient of variations of the ODFs) are plotted on the mesh in Fig. 4.15. It is found that some of the ODF values with high mean values also have higher standard deviations but still there are some other ODFs with high standard deviations and relatively lower mean values because of the larger experimental variations for those nodes. Thus, the coefficient of variation (ratio of standard deviation to mean) of the ODFs is not entirely uniform since the higher density areas indicate the ODFs with relatively

higher standard deviations compared to their mean values.

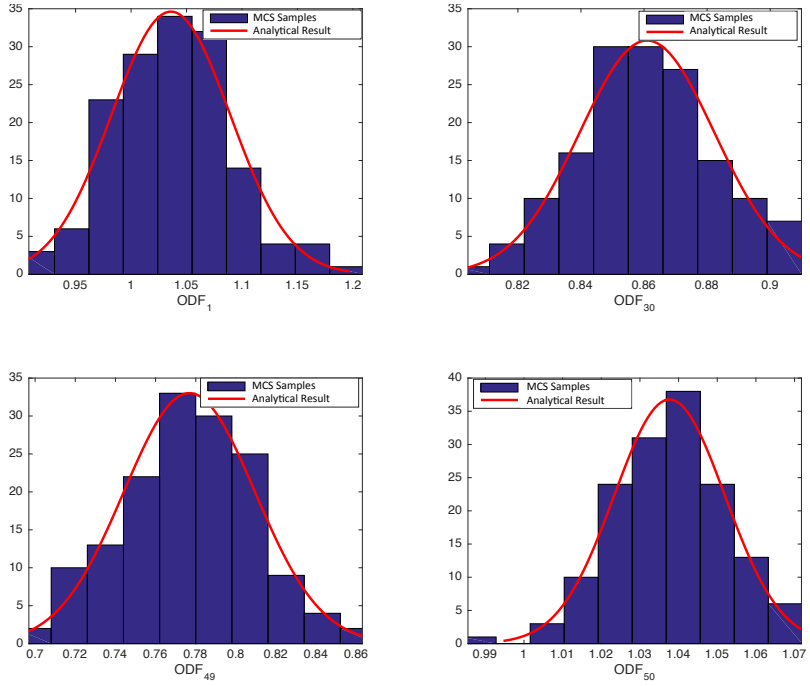

Figure 4.14: Probability histograms of the ODFs

The uncertainties in the ODFs and material properties are quantified using MCS and a Gaussian distribution model to compare the results of the analytical model. In the MCS approach, the aforementioned 150 experimental samples are used to directly compute the ODFs from each set. Then, 150 sets of material properties (S_{11}, E_1, etc.) are computed from these ODFs using the homogenization relation. Histograms of these ODFs and properties are directly compared to the Gaussian analytical solution. The analytical solution is again much faster even though all the ODFs are modeled as correlated variables. The solution times are around 7 seconds for analytical models and 20 minutes for MCS on the same computational platform. However, MCS provides exact solutions since no Gaussian PDF approximation is made. Since the Gaussian analytical solution models all the ODF values as correlated variables a full covariance matrix is used to represent the variations of the ODFs. The MCS results for the probability distributions of S_{11}, S_{66}, E_1, G_{12}, ω_{1t} and ω_{1b} are

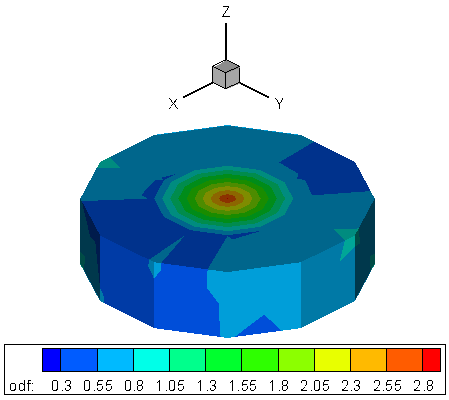

(a) Difference of mean values and standard deviations of the ODFs

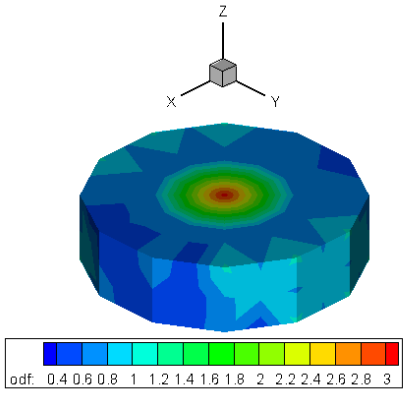

(b) Mean values of the ODFs

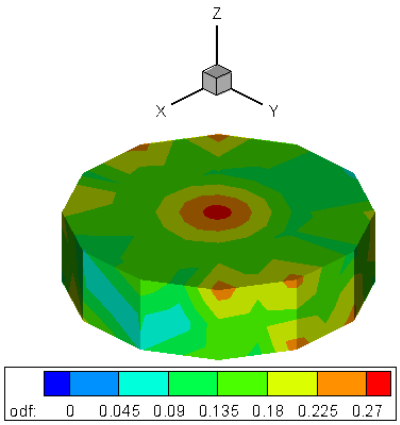

(c) Standard deviations of the ODFs

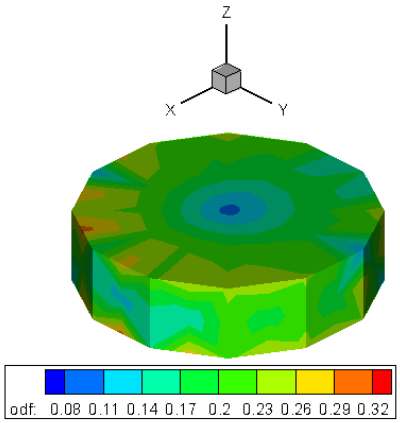

(d) Coefficient of variations of the ODFs

Figure 4.15: Statistical features of the ODF probability distributions

shown together with the analytical model results in Fig. 4.16. Similarly, the PDFs of the first torsion and bending natural frequencies are computed using a transformation function $u(y) = a\sqrt{y}$, where a is a constant, due to the relations between G_{12} and ω_{1t}, and E_1 and ω_{1b}.

From the presented MCS analysis, it is seen that the probability distributions computed with MCS are in very good agreement with the distributions of the analytical model for the ODF and properties in Fig. 4.14 and Fig. 4.16. However, the variances represented by MCS are slightly larger than those from the analytical solution due to the differences between the actual EBSD histograms and the Gaussian

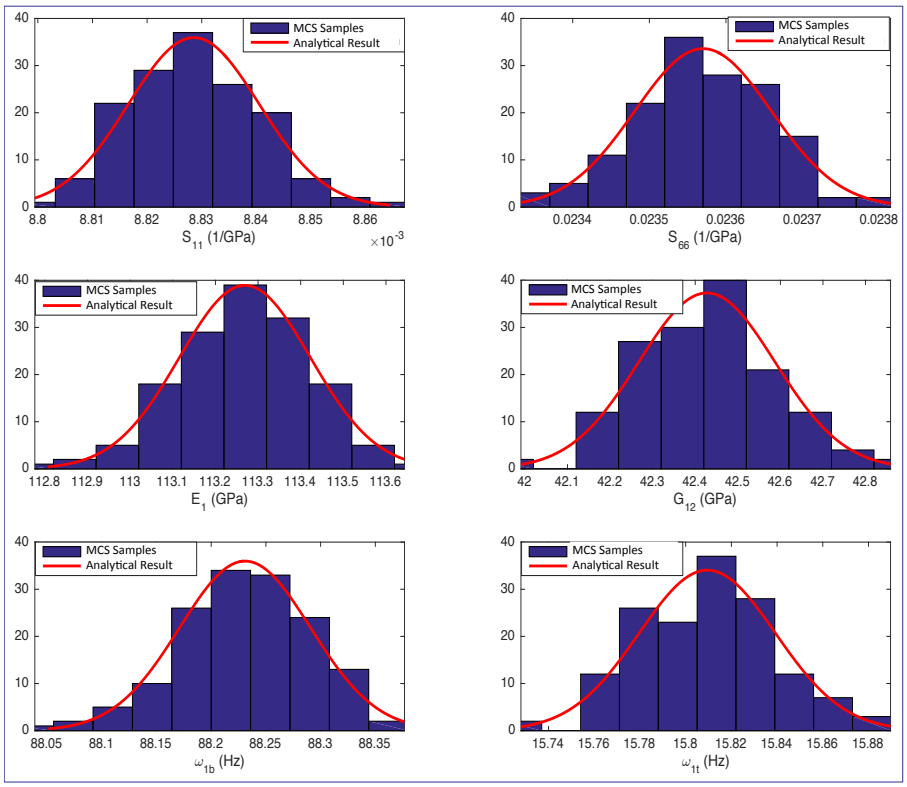

Figure 4.16: Probability histograms of S_{11}, S_{66}, E_1, G_{12}, ω_{1t} and ω_{1b}

approximation as seen in Fig. 4.14. However, analytical methods are much faster, which is important when stochastic ODFs are employed in multi-scale formulations of thermomechanical processes [73].

4.4 Conclusion

An analytical model is developed for quantification of experimental uncertainties and their propagations on microstructural features and material properties using volume averaged homogenization relationships. The uncertainties in experimental PF and EBSD scans are identified using Ti-7Al alloy specimens that were obtained identically through the same process. The uncertainties in the PFs are quantified using 100 equally sized diffraction samples while the EBSD data is analyzed with 150 equally sized samples, and they are fitted to a Gaussian distribution. The probability

distribution of the last ODF parameter is computed using volume fraction normalization constraint. The probability distributions of the linear properties, including the last ODF and the compliance parameters, are calculated using the linear homogenization equations. The mathematical model for the probability distributions of nonlinear properties is identified using transformation of random variables. Using this approach, the uncertainty bounds for the Young's modulus, shear modulus, the first torsion and bending natural frequencies of the Ti-Al alloy specimen are calculated. These derivations are important for development of an ICME toolbox for computing the uncertainty in multi-scale homogenization models due to input uncertainties. The overall analysis is fully analytical when using the Gaussian distribution. However, a drawback of Gaussian distribution is that it allows for negative variables. All the variables considered here, i.e. ODFs, EBSD, PFs, and the properties are all positive. PDFs with positive variables can instead be considered. Examples of such PDFs include log–normal, exponential, gamma, Weibull and Rayleigh distributions. Exact analytical treatment of linear system of equations of correlated random variables (e.g. Eq. 4.2) is not available in literature. Some analytical approximations are available for independent random variables [74]. However, it is important to note that the pole density functions are highly correlated, as modeled here, and cannot be assumed to be independent. This can be seen from the fact that all pole density functions are derived from the same underlying ODF. The only useful analytical result that could be found in literature was the case of correlated sum of Gamma distribution variables with a constant size parameter [75]. Extension of the approach for a linear system of equations of correlated gamma variables could be pursued in the future. Even so, a gamma distribution has an infinite support. In contrast, the properties have a finite support and are constrained within the extremal values of single crystals [76]. Although a point in the fundamental region can take any value in the positive real axis $(0, \infty)$, numerically the ODF is also modeled to have compact support when

the fundamental region is discretized. That is, the values of A_i range from $(0, 1/q_i)$. Thus, even with the positive PDFs, there have been issues with exceeding the support space of the modeled variables - similar to the case of a Gaussian distribution. Thus, going beyond Gaussian distributions, one needs to also pursue numerical methods such as MCS and collocation techniques for exact UQ. However, the analytical methods provide a considerable reduction in computational times compared to the available numerical techniques. Thus, it is recommended that the Gaussian approach presented here to be used as a first step to verify more advanced UQ models. Future effort in this direction includes development of (i) improved methods for building ODFs from crystal aggregate data (using microdiffraction), (ii) methods for modeling linear systems of correlated PDFs with positive support space and (iii) methods for finding PDFs for highly nonlinear homogenization relationships. Another interesting UQ problem is the inverse (or materials design) problem of finding the ODF and its uncertainty bounds in order to achieve a set of desired property PDFs, as discussed in Chapter 5.

CHAPTER 5

Stochastic Design Optimization of Microstructures

Microstructural uncertainties arise from variations in manufacturing process conditions and can affect the performance of metallic materials in aerospace components. This is an aleatoric uncertainty, which is unavoidable and naturally present in metallic systems. Chapter 5 focuses on the effect of aleatoric uncertainties in microstructure modeling and inverse design of stochastic microstructural features to achieve a prescribed statistical range of engineering properties. Current state of the art only addresses the direct UQ problem (effect of uncertain microstructures on properties) and the stochastic inverse problem has not been addressed to the best of author's knowledge. The direct problem has been generally addressed using computational techniques such as MCS, collocation and spectral decomposition methods. In Chapter 5, the analytical formulation based on a Gaussian distribution approach to represent the variations of the random parameters is employed to solve a stochastic design optimization problem for the Galfenol beam vibration tuning application. Some of the details about the optimization results presented in this chapter can also be found in [39]. The variations of in-plane Young's modulus (E_1) and shear modulus (G_{12}) are assumed to be provided by the manufacturer, and consistent with the Gaussian distribution. Then the probability distributions of the ODFs are computed by solving an inverse problem. The variations in the compliance parameters, S_{11} and S_{66}, are

found first with transformation of random variables rule using input variations in E_1 and G_{12}. The compliance parameters are calculated first since they can be represented with linear equations in terms of the ODFs. The probability distributions of the compliance parameters are also assumed to be modeled with a Gaussian approach despite their nonlinear relation to E_1 and G_{12} since the input uncertainties are very small. Then the inverse problem to find the statistical properties of the ODFs is defined as an LP problem. A global stochastic optimization approach is implemented to this analytical solution framework to maximize the yield stress under vibration tuning constraints defined for the first bending and torsion natural frequencies of the cantilever beam. The optimization variables are defined as the in-plane Young's modulus (E_1) and shear modulus (G_{12}) of the Galfenol material, and each design sample is assumed to have the same level of uncertainty. The stochastic design optimization framework is also illustrated in Fig. 5.1.

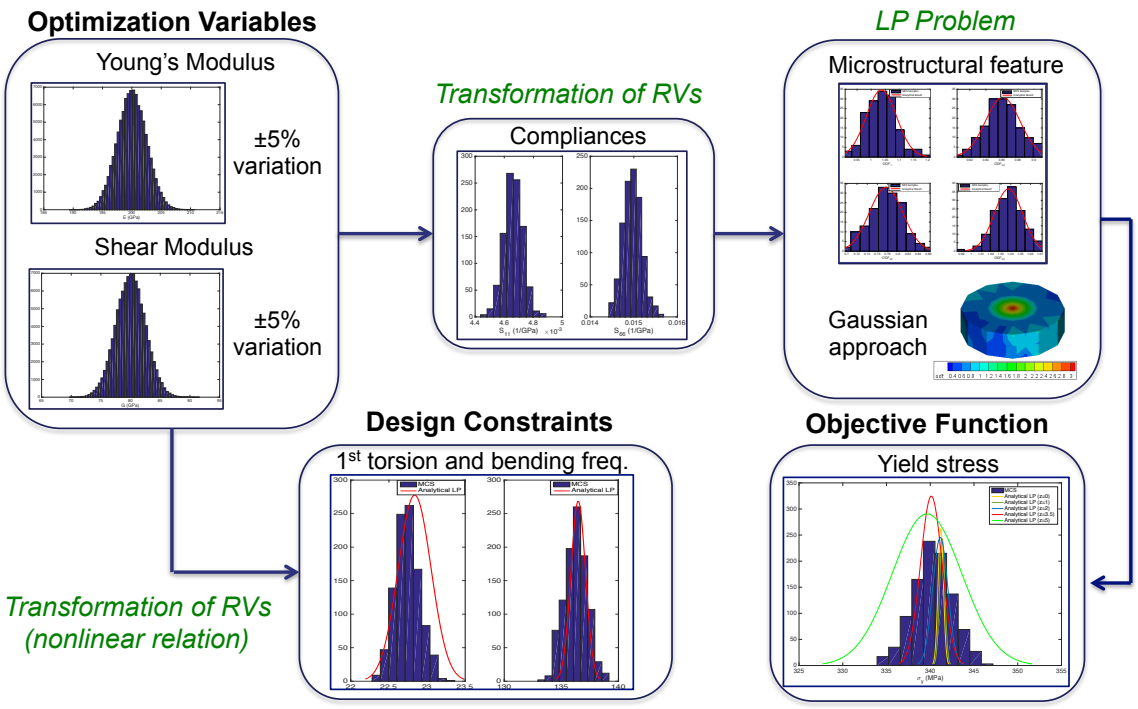

Figure 5.1: The stochastic optimization scheme for the Galfenol beam vibration tuning problem

The LP problem approach has been studied before to find the optimal processing route to produce an optimum microstructure design for the same vibration tuning problem [40]. However, this LP approach was employed to find the ODF solution of a deterministic system [38, 40, 77]. In this chapter, the LP solution methodology is extended to identify the statistical parameters of the ODFs in case of uncertainties in material properties. To the best of the author's knowledge this is the first analytical effort in literature for quantification of microstructural stochasticity given the desired statistical range in properties, in effect, a stochastic inverse problem for microstructure design [39]. The same analytical UQ algorithm is used to solve the stochastic optimization problem. However, since the inverse LP problem requires the solution of the statistical parameters of the joint probability distribution of the ODFs, the ODF values are first assumed to be independent variables for simplicity. Then the inverse analytical approach is extended to solve the statistical parameters when the ODFs are fully correlated. The optimization results are also compared to the results of computational methods which employ MCS to quantify the uncertainties. The analytical algorithm is able to compute the same optimum variables and a very close objective function value to the MCS solution, and decrease the computational time by almost two orders of magnitude. Once the optimum ODFs are achieved, then the multiple solution directions are identified using the direct linear solver. The effect of uncertainties on the design objective is discussed at the end by comparing the optimum results with the deterministic solution for maximum yield stress. The organization of the chapter is as follows: Section 5.1 discusses the development and results of the stochastic optimization problem for the Galfenol beam when the ODFs are modeled as uncorrelated variables in the LP approach. The analytical LP solution methodology is extended in Section 5.2 to model the ODFs as correlated variables. The stochastic optimization problem is also defined accordingly when the ODFs are correlated in Section 5.2. A summary of the chapter with potential future applications

is presented in Section 5.3.

5.1 Stochastic design optimization for the Galfenol beam with uncorrelated ODFs

This section addresses the inverse LP approach to determine the statistical parameters of the ODFs given the probability distributions of the material properties. The inverse LP problem first models the ODFs as uncorrelated variables (the first $k-1$ ODFs are independent and the k^{th} ODF is dependent due to the volume fraction normalization constraint) to reduce the number of unknowns in the problem for simplicity. The same vibration tuning problem for the Galfenol beam is considered. However, the numerical values defined in the design constraints for the first bending and torsion natural frequencies are different in this case since the introduction of the stochasticity violates the feasibility of the deterministic constraints in Chapter 3 and Chapter 6. Therefore the deterministic optimum results presented at the end of Section 5.1 are different than the results in Chapter 3.

5.1.1 LP approach for inverse design

The statistical properties of the ODF values are identified by solving the inverse design problem as an LP problem. The first assumption of the stochastic optimization scheme is that the probability distributions of E_1 and G_{12} are provided, and these distributions are Gaussian with a ± 5 % of variation around the mean values. It is also assumed that the variation is always ± 5 % even though the mean values change (The mean values can change since they are global design variables of the stochastic optimization problem.). The PDFs of S_{11} and S_{66} can be computed using the transformation of random variables rule given in Eq. 4.17 and Eq. 4.18. The variations in these parameters can be assumed to agree with the Gaussian distribution

due to small variations in the input parameters, E_1 and G_{12}. With this assumption the ODF values can be determined by solving an LP problem. A general formulation of an LP problem is given as follows:

$$\begin{aligned} \min \quad & \boldsymbol{f^T x} \\ \text{such that} \quad & \boldsymbol{A_{eq} x = b_{eq}} \\ & \boldsymbol{Ax \leq b} \\ & \boldsymbol{lb \leq x \leq ub} \end{aligned}$$

The unknown vector, $\boldsymbol{x}$, of this LP problem includes the mean values and variances of the first $k-1$ ODF values: $\boldsymbol{\mu_A}$ and $\boldsymbol{\sigma_A{}^2}$. The mean and variance terms related to the k^{th} ODF value can then be obtained using the definitions for $\boldsymbol{\mu_A}$ and $\boldsymbol{\sigma_A{}^2}$ in the volume fraction normalization constraint equation. The equality constraints are derived by using the homogenized linear equations for the mean values (Eq. 5.1 and Eq. 5.2) and variances (Eq. 5.3 and Eq. 5.4):

$$\boldsymbol{p_1^T \mu_A = \mu_{S_{11}}} \tag{5.1}$$

$$\boldsymbol{p_6^T \mu_A = \mu_{S_{66}}} \tag{5.2}$$

$$\boldsymbol{p_1 \Sigma_A p_1^T = \sigma_{S_{11}}{}^2} \tag{5.3}$$

$$\boldsymbol{p_6 \Sigma_A p_6^T = \sigma_{S_{66}}{}^2} \tag{5.4}$$

In these equations, $\boldsymbol{p_1}$ and $\boldsymbol{p_6}$ are the vectors of length k including single crystal coefficient values for S_{11} and S_{66} respectively, $\mu_{S_{11}}$ and $\mu_{S_{66}}$ are the mean values, and ${\sigma_{S_{11}}}^2$ and ${\sigma_{S_{66}}}^2$ are variances of S_{11} and S_{66}. Accounting for the normalization

constraint, only the first $k-1$ ODF values are solved. The augmented system of the equality constraints for the first $k-1$ ODF values can be derived as:

$$\begin{bmatrix} [\boldsymbol{p_1}^T - \frac{p_1(k)}{q_k}\boldsymbol{q^T}]_{(1\times k-1)} & \mathbf{0}_{(1\times k-1)} \\ [\boldsymbol{p_6}^T - \frac{p_6(k)}{q_k}\boldsymbol{q^T}]]_{(1\times k-1)} & \mathbf{0}_{(1\times k-1)} \\ \mathbf{0}_{(1\times k-1)} & \boldsymbol{P_1^*}_{(1\times k-1)} \\ \mathbf{0}_{(1\times k-1)} & \boldsymbol{P_6^*}_{(1\times k-1)} \end{bmatrix} \begin{bmatrix} \boldsymbol{\mu_A}_{(k-1)\times 1} \\ \boldsymbol{\sigma_A^2}_{(k-1)\times 1} \end{bmatrix} = \begin{bmatrix} \mu_{S_{11}} - \frac{p_1(k)}{q_k} \\ \mu_{S_{66}} - \frac{p_6(k)}{q_k} \\ {\sigma_{S_{11}}}^2 \\ {\sigma_{S_{66}}}^2 \end{bmatrix}$$

where $\mathbf{0}_{1\times(k-1)}$ is a row vector of zeros with a length of $k-1$. The elements of the row vectors, $\boldsymbol{P_1^*}$ and $\boldsymbol{P_6^*}$, can be calculated as below by using Eq. 5.3 and Eq. 5.4 with the definition for $\boldsymbol{\Sigma_A}$ $(i = 1, 2, ..., k-1)$:

$$P_1^*(i) = [p_1^2(i) + (p_1(k)+1)(p_1(i)c(i)) + (p_1^2(k)c^2(i))] \tag{5.5}$$

$$P_6^*(i) = [p_6^2(i) + (p_6(k)+1)(p_6(i)c(i)) + (p_6^2(k)c^2(i))] \tag{5.6}$$

where $c(i) = -\frac{q(i)}{q(k)}$ $(i = 1, 2, .., k-1)$.

The first inequality equation is derived for the lower boundary of the k^{th} ODF value such that the first $k-1$ ODFs should satisfy the constraint, $\boldsymbol{q^T\mu_A} \leq \mathbf{1}$, to guarantee that the unit volume normalization constraint is satisfied with a non-negative k^{th} ODF value ($\boldsymbol{q} > \mathbf{0}$ and $q_k > 0$). Since the compliance parameters are assumed to agree with the Gaussian approach the ODF values have the same distribution because of their linear relation. The following inequalities are used to ensure that the probability distributions of the ODFs always satisfy the non-negativity condition: $\boldsymbol{-\mu_A + z\sigma_A^2} \leq \mathbf{0}$ and $-\mu_{A_k} + z{\sigma_{A_k}}^2 \leq 0$ where z is a constant to be determined. In these inequality equations the standard deviation parameter is approximated by the variance since the variances are the unknowns in the LP problem definition. The

standard deviation can be replaced with the variance since the standard deviation and variance values of the compliances are in the same order, and the ODFs are assumed to follow the same trend. However, the variances are controlled with the constant parameter, z, rather than directly considering the traditional 3.5σ assumption for Gaussian distribution. The inequality equation for the variation of the k^{th} ODF can be manipulated further by using the definitions for μ_{A_k} and ${\sigma_{A_k}}^2$. The final form of the inequality equations is given in Eq. 5.7, 5.8 and 5.9:

$$\boldsymbol{q^T \mu_A} \leq 1 \tag{5.7}$$

$$-\mu_A + z{\sigma_A}^2 \leq 0 \tag{5.8}$$

$$-\frac{1}{q_k}\boldsymbol{q^T \mu_A} + z\boldsymbol{C^* {\sigma_A}^2} \leq \frac{1}{q_k} \tag{5.9}$$

where $\boldsymbol{q}$ is a vector containing the first $k-1$ values of normalization vector and the elements of the $\boldsymbol{C^*}$ vector are: $C^*(i) = c(i)^2$. Using Eq. 5.7, 5.8 and 5.9 the augmented system for the inequality constraints can be derived as below:

$$\begin{bmatrix} \boldsymbol{q^T}_{(1\times k-1)} & \boldsymbol{0}_{(1\times k-1)} \\ -[\boldsymbol{I}]_{(k-1\times k-1)} & z[\boldsymbol{I}]_{(k-1\times k-1)} \\ \frac{1}{q_k}\boldsymbol{q^T}_{(1\times k-1)} & z\boldsymbol{C^*}_{(1\times k-1)} \end{bmatrix} \begin{bmatrix} \boldsymbol{\mu_A}_{(k-1\times 1)} \\ \boldsymbol{{\sigma_A}^2}_{(k-1\times 1)} \end{bmatrix} \leq \begin{bmatrix} 1 \\ \boldsymbol{0}_{(k-1\times 1)} \\ \frac{1}{q_k} \end{bmatrix}$$

where $[\boldsymbol{I}]$ is the identity matrix, and $\boldsymbol{q}$ vector includes the volume fraction values for the first $k-1$ ODFs.

The objective of the stochastic optimization problem is to maximize the mean yield stress value of the beam. Since the standard LP problem defines the objective function for minimization instead of maximization the negative of the yield stress value, $-\sigma_y$, is minimized. This objective function is also linear in the ODFs such

that: $-\sigma_y = (-\boldsymbol{y^T} + (\frac{y_k}{q_k})\boldsymbol{q^T})\boldsymbol{\mu_A} - \frac{y_k}{q_k}$ where $\boldsymbol{y}$ is the vector of yield stress coefficients for the first $k-1$ single crystals and y_k is the same coefficient value for the k^{th} single crystal. The objective function, f is defined as: $f = (-\boldsymbol{y^T} + (\frac{y_k}{q_k})q^T)\boldsymbol{\mu_A}$ and therefore: $-\sigma_y = f - \frac{y_k}{q_k}$. The objective function of the LP problem for min $\boldsymbol{f^T x}$, can be written as:

$$\boldsymbol{f} = [\boldsymbol{y^{*T}}_{1\times(k-1)}\mathbf{0}_{1\times(k-1)}]^T \tag{5.10}$$

where $\boldsymbol{y^{*T}}$ is defined as: $\boldsymbol{y^{*T}} = -\boldsymbol{y^T} + (\frac{y_k}{q_k})\boldsymbol{q^T}$. In the final step, the lower and upper bounds are determined considering the non-negativity conditions for the ODFs. The unknowns of the LP problem, the mean values and on-diagonal variance terms of the ODF parameters, have a zero value lower bound. An ODF, A_i, can have the value of $1/q_i$ as an upper bound. This is also true for the mean values, μ_{A_i}. However, the variances are known to be lower than the mean values in this problem. Therefore defining the same upper bound values for the corresponding variance terms is mathematically possible. The lower and upper bound vectors for this problem are then defined as: $\boldsymbol{lb} = [\mathbf{0}_{1\times 2(k-1)}]$ and $\boldsymbol{ub} = [1/q_i \;\; 1/q_i]$, where $i = 1, 2, .., k-1$.

5.1.2 Definition of the stochastic optimization problem

The optimization starts with the global sampling for the input variables, μ_{E_1} and $\mu_{G_{12}}$, which are the mean values of E_1 and G_{12}. In the next step, the statistical properties of compliances, S_{11} and S_{66}, and natural frequencies, ω_{1t} and ω_{1b}, are calculated using the random variables transformation rule. The ODF solution satisfying the calculated statistical properties of the compliances and maximizing the mean yield stress value is identified by implementing the LP problem of Section 5.1.1 to the optimization algorithm. The mathematical formulation of the optimization problem is given below:

$$max \quad \mu_{\sigma_y} \tag{5.11}$$

$$subject\ to \quad P(20.25\ \text{Hz} \leq \omega_{1t} \leq 24.25\ \text{Hz}) = 1 \tag{5.12}$$

$$subject\ to \quad P(132.75\ \text{Hz} \leq \omega_{1b} \leq 139.75\ \text{Hz}) = 1 \tag{5.13}$$

$$\boldsymbol{s} = (\mu_{E_1}, \mu_{G_{12}}), \tag{5.14}$$

where the optimization variables are μ_{E_1} and $\mu_{G_{12}}$ in the global problem, and the means and variances of the first $k-1$ ODFs in the LP problem definition. Eq. 5.11 shows the objective function, which is determined as maximization of the mean yield stress value. The output variables have probability distributions based on their statistical properties. The constraint parameters are expected to satisfy the strict vibration tuning constraints in every point of their probability distribution. Therefore the probability of satisfying the design constraints is expected to be 1 as shown in Eq. 5.12 and Eq. 5.13. In the last row, $\boldsymbol{s}$ shows the vector of global optimization variables. The corresponding ODF solution to the optimum values of the global variables provides the optimum microstructure design of the problem. The non-negativity condition of the ODFs is considered as a lower bound in the LP problem. The volume normalization constraint is also considered through the definition of the k^{th} ODF and the inequality constraint in Eq. 5.7.

5.1.3 Results

The stochastic optimization is performed using ISF as the global sampling method for the input parameters, and NSGA-II as the optimization algorithm in Modefrontier software. However, the limits of the design constraints are different in this problem than the limits presented in Chapter 3 and Chapter 6 since the introduction of the stochasticity violates the deterministic constraints. In order to compare the effect of

uncertainty to the final design and material properties a deterministic optimization is also performed for the same problem. The constant parameter, z, of the analytical LP approach is considered as $z = 3.5$. In addition, another stochastic optimization, which uses MCS method to model the uncertainties, is performed. In this MCS technique, 10000 samples are used to generate the probability distributions for one set of global ISF sample points. The compliance values, S_{11} and S_{66}, are calculated using the exact equations in terms of the input parameters. Then the ODF solutions are identified by solving for 10000 separate LP problems per one global sample. These deterministic LP problems are simplified forms of the presented LP methodology since they do not consider the inequality constraints defined for the variations (Eq. 5.8 and Eq. 5.9). The MCS method, despite the use of the LP approach to solve the ODFs, is a computational burden compared to the required computational time to run the analytical solution. The optimum design parameters of stochastic optimization studies are given in Table 5.1. In all cases, the optimum parameters correspond to multiple optimum polycrystal designs with the implementation of the direct linear solver. The optimum deterministic parameters are also shown as the deterministic case (with no uncertainties) in Table 5.1 to indicate the significant impact of the uncertainties to the design objective. The significant difference between the computational times spent on the stochastic optimization studies is also pointed in the last row of Table 5.1.

Table 5.1: Stochastic optimization results for vibration tuning of the Galfenol beam

Deterministic	Stochastic (Analytical)	Stochastic (MCS)
$\sigma_y = 367.9385$ MPa	$\mu_{\sigma_y} = 340.1034$ MPa	$\mu_{\sigma_y} = 340.2584$ MPa
$\omega_{1t} = 22.7038$ Hz	$\mu_{\omega_{1t}} = 22.8272$ Hz	$\mu_{\omega_{1t}} = 22.7408$ Hz
$\omega_{1b} = 134.3167$ Hz	$\mu_{\omega_{1b}} = 136.4554$ Hz	$\mu_{\omega_{1b}} = 136.2892$ Hz
$E_1 = 262.5002$ GPa	$\mu_{E_1} = 270.3112$ GPa	$\mu_{E_1} = 270.3112$ GPa
$G_{12} = 87.5001$ GPa	$\mu_{G_{12}} = 87.8067$ GPa	$\mu_{G_{12}} = 87.8067$ GPa
$t = 5$ mins	$t = 20$ mins	$t = 44$ hours 35 mins

The difference between the optimum objective function values of the deterministic case and stochastic optimization (Table 5.1) implies the substantial impact of the input uncertainties to the engineering properties. One critical feature of the results is that both stochastic optimization applications are able to identify the same solution for the global input parameters, μ_{E_1} and $\mu_{G_{12}}$. However, the optimum design criteria and objective function values are slightly different due to the different solution approaches in the analytical model such as random variables transformation rule and extended LP problem implementation by consideration of the ODF variances in contrast to the exact solution formulas being used by the MCS method. The variations of the yield stress and vibration frequencies of the stochastic optimum designs are shown in Fig. 5.2. According to the results in Fig. 5.2 the analytical model is able to capture the mean values and variances of the optimum material properties.

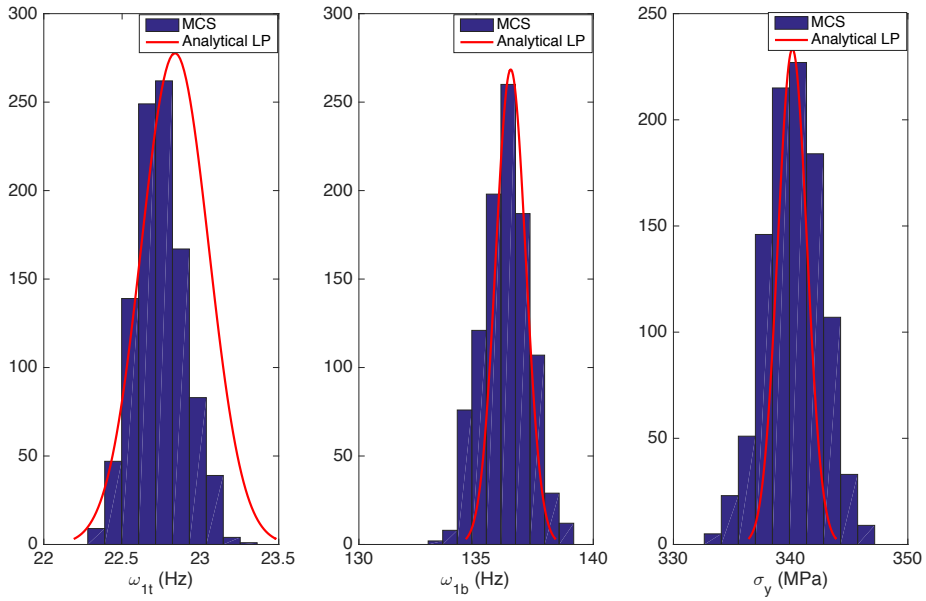

Figure 5.2: The variations of yield stress and vibration frequencies of the stochastic optimum designs

After identifying the optimum solutions to the stochastic problems the multiple polycrystal designs are also computed using the direct linear solution methodology with null space approach. Some of the multiple optimum solutions to the ODF

mean values obtained by the analytical model and MCS are shown in Fig. 5.3. The first microstructure design of both solutions is the optimum initial design identified with the global optimization. The other microstructures are obtained using the same independent null space vectors in the direct linear solver for both analytical and MCS solutions.

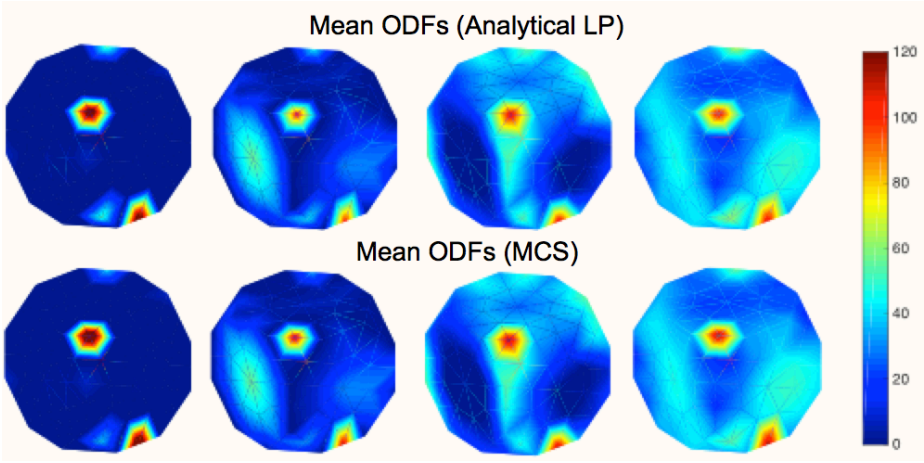

Figure 5.3: Examples for multiple optimum microstructures of the stochastic optimization problem

The small differences between the analytical model and MCS results in the final material properties shown in Fig. 5.2 and multiple optimum ODF solutions shown in Fig. 5.3 can be explained with two features of the analytical approach. First, the analytical solution assumes that the first $k-1$ ODFs are independent, and identifies only the on-diagonal variances for these ODFs. The system of equations in the LP problem already imply an underdetermined system, and the consideration of the non-diagonal terms can yield to infeasible or multiple solutions. However, the MCS method automatically considers the dependencies of the ODFs since it uses the exact solutions with direct sampling. The other reason is predicted to be the effect of the adjustable constant parameter, z, of the analytical solution, which represents the ODF variations. The condition, $z = 3.5$, is used in the results reported in Fig. 5.2 and Fig. 5.3. The effect of this parameter is further investigated by computing the

yield stress values of the optimum microstructure using different z values. The same analysis is not performed for the natural frequency parameters since they are directly related to the global variables, not to the LP problem, so the change in z parameter does not affect them. The yield stress distributions of the optimum microstructure design with varying z values in the analytical solution are shown in Fig. 5.4.

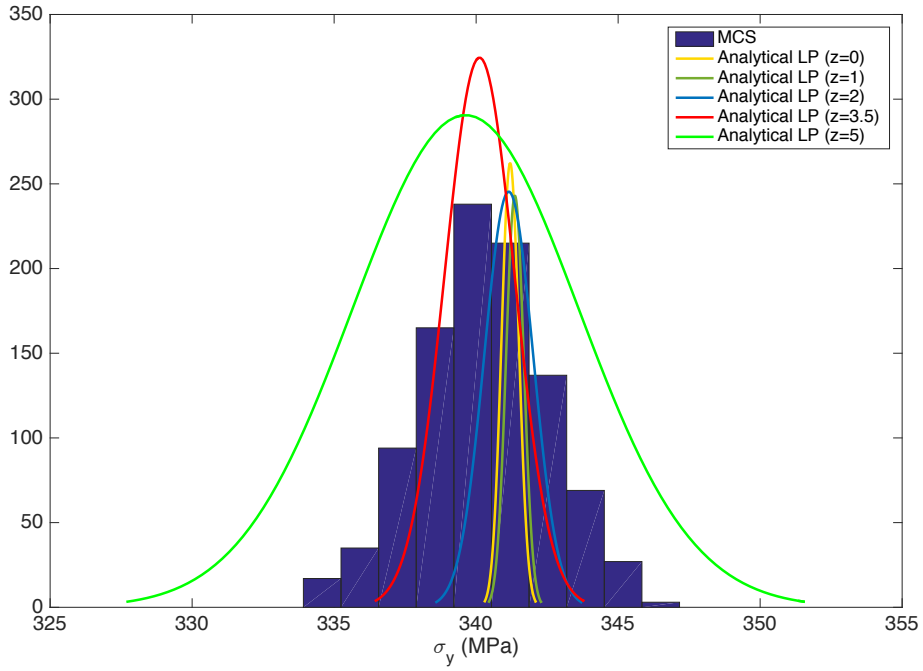

Figure 5.4: Yield stress distributions of the optimum microstructure design with varying z values in the analytical solution

Fig. 5.4 implies that the variations in the optimum yield stress parameter are smaller when z is smaller. This is an expected result since z represents the variations in the ODFs. Compared to the MCS samples the best matching analytical result is provided by $z = 3.5$ condition, which was also used in the stochastic optimization.

5.2 Stochastic design optimization with correlated ODFs

The analytical inverse LP formulation is advanced to compute the statistical parameters of the ODFs when all the ODFs are correlated. However, the number of

variables in the LP formulation greatly increases due to inclusion of the off-diagonal terms in the ODF covariance matrix. The Galfenol beam problem is a single-objective problem with two engineering design constraints. Even though the additional design criteria, such as the unit volume fraction normalization, increase the number of equations in the LP formulation the system of equations still implies a highly underdetermined system. Enforcing a solution to represent all the statistical quantities of the ODFs is not mathematically possible since some certain statistical parameters are required to satisfy the non-negativity condition as well. Therefore instead of solving the previous Galfenol problem the analytical modeling for representing the joint probability distribution of the correlated ODF variables is exercised in a new application problem. In this application problem it is assumed that the input uncertainties of 9 orthotropic stiffness parameters of the Galfenol material is provided. The problem has the same objective with the previous applications since the goal is to maximize the mean value of the yield stress. However, solving this problem for 76 independent ODF values still implies an underdetermined system. Therefore instead of using the previous mesh with 76 independent ODF values a coarser mesh with 10 ODFs is preferred to solve the stochastic optimization problem by modeling the ODFs as correlated variables.

5.2.1 LP problem derivation

The stochastic design optimization problem of this section assumes that all the ODF parameters are dependent. In this case the LP problem solves both diagonal and off-diagonal entries in the covariance matrix of the Gaussian joint probability distribution. Consideration of a full covariance matrix is expected to improve the accuracy in representing the uncertainties, however, it increases the problem dimensionality. Therefore a coarser mesh in Rodrigues domain is preferred. For this application it is assumed that the Gaussian joint probability distributions (mean values and full

covariance matrix) of 9 stiffness parameters of the Galfenol material with random texture are provided. The problem aims to find the ODF solutions which maximize the mean yield stress. The LP problem solves for mean values of these k ODF parameters and their full $(k \times k)$ symmetric covariance matrix, n number of unknowns totally. The equality constraints of the LP problem are derived using the homogenized equations for all stiffness parameters (C_{11}, C_{12}, C_{13}, C_{22}, C_{23}, C_{33}, C_{44}, C_{55} and C_{66}) considered in this application:

$$\boldsymbol{p_{11}^T \mu_A} = \mu_{C_{11}} \tag{5.15}$$

$$\boldsymbol{P \Sigma_A P^T} = \boldsymbol{\Sigma_C} \tag{5.16}$$

$$\boldsymbol{q \Sigma_A q^T} = \boldsymbol{0} \tag{5.17}$$

where Eq. 5.15 shows the formulation to obtain the mean value, $\mu_{C_{11}}$, of the stiffness parameter C_{11}. $\boldsymbol{p_{11}}$ is the vector of length k including single crystal coefficients for C_{11}. The computations of the mean values for the other stiffness parameters apply the same formulation. Eq. 5.16 shows the computation of the covariance matrix for the joint probability distribution of the stiffness parameters. In Eq. 5.16, $\boldsymbol{P}$ is a $(9 \times k)$ matrix including the k single crystal values for 9 stiffness coefficients, and $\boldsymbol{\Sigma_A}$ and $\boldsymbol{\Sigma_C}$ are the ODF and stiffness covariance matrices respectively. It is assumed that the mean values of the stiffness parameters ($\mu_{C_{11}}$, $\mu_{C_{12}}$, ..., $\mu_{C_{66}}$), and stiffness covariance matrix, $\boldsymbol{\Sigma_C}$ are provided. Note that the input stiffness covariance matrix is generated using 100000 design samples generated for the ODF values using MCS. In these samples the ODF values are varied according to a Gaussian distribution around the mean values which correspond to a random texture design. The stiffness values are computed with volume averaging equations for each design sample, and the semi

positive definite covariance matrices are generated accordingly. The unknowns of the problem are ODF mean values vector, $\boldsymbol{\mu_A}$, and ODF covariance matrix, $\boldsymbol{\Sigma_A}$. The ODF covariance matrix is expected to agree with the given relation in Eq. 5.17 since for any point drawn from the joint ODF probability distribution the normalization constraint ($\boldsymbol{q^T A = 1}$) should be satisfied. This constraint (Eq. 5.17) can be enforced strictly by using an equivalent formulation derived separately for all columns of the covariance matrix such that $\boldsymbol{q^T \Sigma_{A:,j} = 0}$ $(j = 1, 2, .., k)$. The new constraint will be shown as $\boldsymbol{\bar{Q}\Sigma_A = 0}$ hereafter. Note that the input covariance matrix of the ODFs which show the variations of the initial ODF samples generated by the MCS approach also satisfies this constraint.

In the previous application the problem was solved for $k-1$ independent ODF parameters by introducing the definition of the k^{th} ODF through volume normalization constraint. However in this problem the solution is already defined for all k ODFs directly and thus the volume normalization constraint (Eq. 5.18) should be included as an equality constraint:

$$\boldsymbol{q^T \mu_A} = 1 \tag{5.18}$$

Using the above formulation the augmented system of equality constraints for the ODFs can be derived as:

$$\begin{bmatrix} \boldsymbol{q^T}_{(1\times k)} & \mathbf{0}_{(1\times n-k)} \\ \boldsymbol{P}_{(9\times k)} & \mathbf{0}_{(9\times n-k)} \\ \mathbf{0}_{(9\times k)} & \bar{\boldsymbol{P}}_{(9\times k)} \\ \mathbf{0}_{(k\times k)} & \bar{\boldsymbol{Q}}_{(k\times n-k)} \end{bmatrix} \begin{bmatrix} \boldsymbol{\mu_A}_{(k\times 1)} \\ \boldsymbol{\Sigma_A}^{\boldsymbol{vec}}{}_{(n-k\times 1)} \end{bmatrix} = \begin{bmatrix} 1 \\ \boldsymbol{\mu_C}^{\boldsymbol{vec}}{}_{(k\times 1)} \\ \boldsymbol{\Sigma_C}^{\boldsymbol{vec}}{}_{(n-k\times 1)} \\ \mathbf{0}_{(k\times 1)} \end{bmatrix}$$

where $\boldsymbol{\mu_C}$ is the vector of stiffness mean values such that:
$\boldsymbol{\mu_C} = [\mu_{C_{11}}\ \mu_{C_{12}}\ \mu_{C_{13}}\ \mu_{C_{22}}\ \mu_{C_{23}}\ \mu_{C_{33}}\ \mu_{C_{44}}\ \mu_{C_{55}}\ \mu_{C_{66}}]^T$, and $\boldsymbol{\Sigma_C}^{\boldsymbol{vec}}$ is the vector containing the elements of stiffness covariance matrix, $\boldsymbol{\Sigma_C}$, such that:

$\boldsymbol{\Sigma_C}^{vec} = [\Sigma_{C11}\ \Sigma_{C12}\ \Sigma_{C13}\ \Sigma_{C22}\ \Sigma_{C23}\ \Sigma_{C33}\ \Sigma_{C44}\ \Sigma_{C55}\ \Sigma_{C66}]^T$. Similarly, the ODF covariance matrix elements are also included in $\boldsymbol{\Sigma_A}^{\boldsymbol{vec}}$ such that:
$\boldsymbol{\Sigma_A}^{vec} = [\Sigma_{A1,1}\ \Sigma_{A2,2}\ ...\ \Sigma_{Ak,k}\ \Sigma_{A1,2}\ ...\ \Sigma_{A1,k}\ ...\ \Sigma_{Ak-1,1}]^T$. $\bar{\boldsymbol{P}}$ is the coefficient matrix derived through the covariance relation in Eq. 5.16 to represent the ODF covariance matrix, $\boldsymbol{\Sigma_A}$, in the vector form, $\boldsymbol{\Sigma_A}^{\boldsymbol{vec}}$.

The inequality constraints are the same with the constraints in Eq. 5.7 and 5.8. Eq. 5.8 can be modified for the new problem to include the constraints for all the ODFs, therefore the constraint defined for the k^{th} ODF in the previous problem (Eq. 5.9) is not required. The augmented system for inequality equations is given below:

$$\begin{bmatrix} \boldsymbol{q^T}_{(1\times k-1)} & \boldsymbol{0}_{(1\times n-(k-1))} & \\ -[\boldsymbol{I}]_{(k\times k)} & z[\boldsymbol{I}]_{(k\times k)} & \boldsymbol{0}_{(k\times n-2k)} \end{bmatrix} \begin{bmatrix} \boldsymbol{\mu_A}^{\boldsymbol{vec}}{}_{(k\times 1)} \\ \boldsymbol{\Sigma_A}^{\boldsymbol{vec}}{}_{(n-k\times 1)} \end{bmatrix} \leq \begin{bmatrix} 1 \\ \boldsymbol{0}_{(k\times 1)} \end{bmatrix}$$

The objective of the problem is again to maximize the mean value of the yield stress. Therefore the objective function derivation is very similar to the previous problem. Since the unknowns of this application include the k^{th} ODF the objective function can directly be written as:

$$\boldsymbol{f} = [-\boldsymbol{y^T}_{(1\times k)}\ \ \boldsymbol{0}_{1\times n-k}]^T \tag{5.19}$$

The lower and upper bound vectors for this problem are then defined as: $\boldsymbol{lb} = [\boldsymbol{0}_{(1\times 2k)}\ \text{-}\boldsymbol{\infty}_{(1\times n-2k)}]$ and $\boldsymbol{ub} = [\frac{1}{\boldsymbol{q^T}}_{(1\times k)}\ \ +\boldsymbol{\infty}_{(1\times n-k)}]$. Here the mean values of the ODFs are bounded between 0 and $\frac{1}{q_i}$ (where $i = 1, 2, ..., k$). The on-diagonal covariance terms can vary in $[0, +\infty)$. The off-diagonal covariance terms can be any real value in $(-\infty, +\infty)$.

5.2.2 Optimization problem and results

The mathematical definition of the optimization problem is given below:

$$max \quad \mu_{\sigma_y} \tag{5.20}$$

$$\boldsymbol{s} = (\boldsymbol{\mu_A}, \boldsymbol{\Sigma_A}) \tag{5.21}$$

The optimization problem does not have any global design constraint this time, and the objective function is directly dependent on the optimization variables which are the unknowns of the LP problem. It is assumed that the stiffness parameters have some uncertainty around their mean values, and the mean values are obtained from the random texture design. It is also assumed that the stiffness covariance matrix is provided initially. The stochastic optimization problem is solved directly as an LP problem since global sampling is not required for this unconstrained problem. The optimum value of the objective function, $max\ \mu_{\sigma_y}$, is calculated as $max\ \mu_{\sigma_y} = 502.2867$ MPa for $z = 3.5$ case. This problem has a unique solution due to the use of all the elements in ODF and stiffness covariance matrices. Even though there are some other ODF solutions which can provide the same objective function value these solutions do not lead to the same stiffness covariance matrix. The unique ODF solution changes slightly when the problem is solved with different z values but all cases imply very similar textures. The initially provided probability distributions of the stiffness parameters were generated by assuming variations around a random texture design. Therefore the mean ODF values, which are calculated with the presented analytical formulation, are expected to correspond to similar textures, and eventually converge to the random texture. Fig. 5.5 shows the mean ODF solutions with different z values and random texture ODFs (The ODFs are the same in a random texture.). According to Fig. 5.5, all the ODF solutions provide very similar textures to random texture, however, starting with $z = 3.5$ case the ODF solutions converge even more

to the random texture. The effect of z parameter is also investigated for maximum yield stress in Fig. 5.6. The LP solutions with various z values are not compared to the MCS solution due to the uniqueness of the solution. According to Fig. 5.6, $z = 3.5$ and $z = 5$ cases provide similar variations. The variations in these cases can be considered sufficient for a reliable design since the ODFs converge to the expected values.

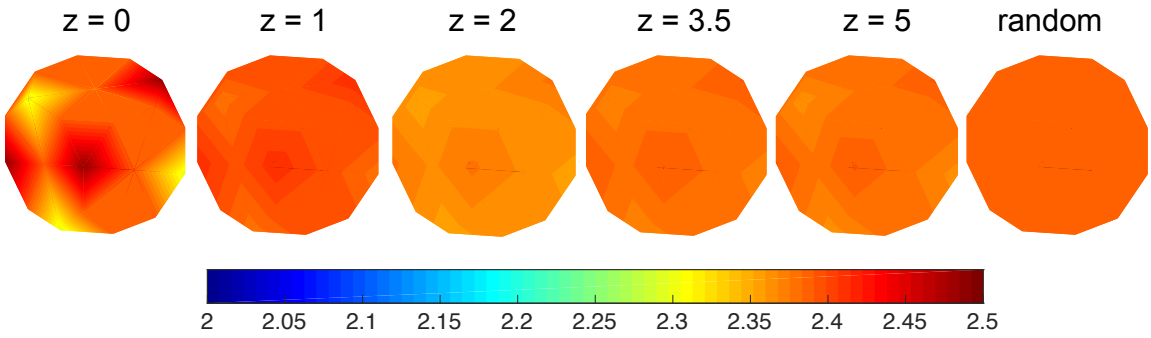

Figure 5.5: Comparison of ODF mean values with random texture

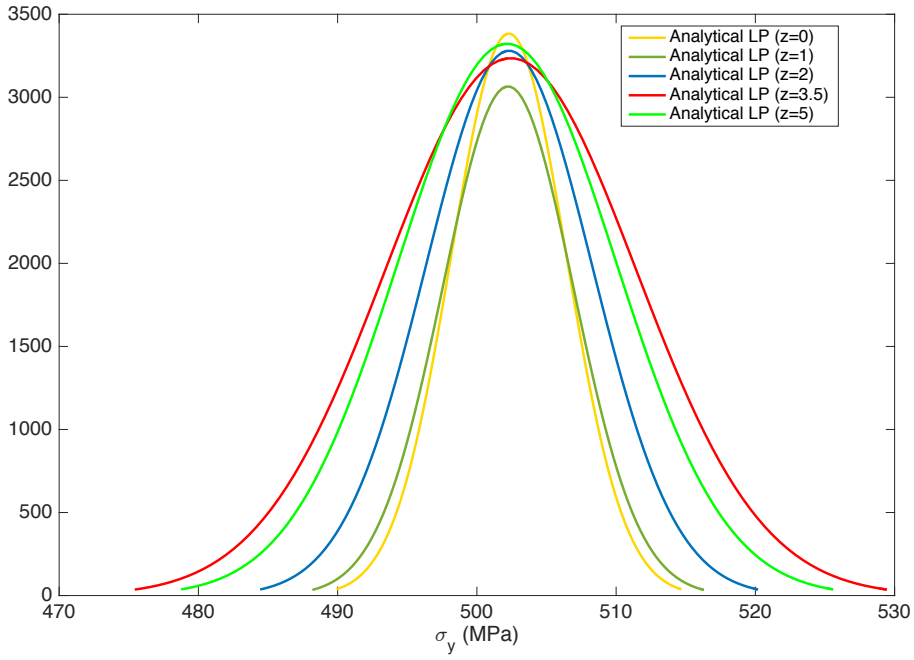

Figure 5.6: Yield stress distributions of the optimum microstructure design with varying z values in the analytical solution

We already saw in the previous chapters that the deterministic optimization problem results in multiple solutions due to the null space of the coefficient matrix. The stochastic optimization problem can also be understood in this context. The PDF of the ODF that results in a given set of properties is non–unique. There are several solutions to the mean value of the ODF that can result in the desired set of properties. In the formulation above, we aim to identify the Gaussian PDF around these mean solutions that will lead to the desired range of properties. However, the problem of maximizing the yield stress given a set of known properties (and its statistics) will result in a much more constrained solution. In effect, we are looking at the null space of the former problem and are identifying the small set of solutions that leads to the highest yield strength. Again, we have solved for the statistics around one of these solutions in this example.

5.3 Conclusion

Chapter 5 addresses a stochastic optimization problem which employs an analytical uncertainty modeling approach. The optimization problem is solved to maximize the mean value of the yield stress of the Galfenol beam under vibration tuning constraints defined for the first torsion and bending natural frequencies. It is initially assumed that the probability distributions of Young's modulus and shear modulus parameters (E_1 and G_{12}) were provided. The probability distributions of these input parameters are assumed to be Gaussian with ± 5 % variations around the mean values. For vibration tuning constraints the random variables transformation rule is applied to compute the probability distributions of the first torsion and bending natural frequencies of the beam. In order to compute the probability distributions of the ODF values the statistical properties of the compliances, S_{11} and S_{66}, are first computed using the same random variables transformation technique. It is assumed that the probability distributions of the compliance parameters can be modeled with

Gaussian approach since the input uncertainties are small. Next, an inverse problem is solved to identify the mean and variance values of the ODF parameters. The inverse design problem is solved by implementing an LP problem approach since the equations to compute the compliance parameters and yield stress are linear in terms of the ODFs. The values for the first $k-1$ ODF parameters are computed, and then the k^{th} ODF is identified through the implementation of the volume fraction normalization constraint to the LP problem. The stochastic optimization is performed on this analytical model to find the optimal ODF solution which maximizes the mean yield stress value. A stochastic optimization, which uses MCS method to model the uncertainties, is also performed to test the analytical results. The analytical solution for uncertainty modeling not only reduced the computational time requirement for the optimization but also provided the same optimum parameters with very slight differences in yield stress and frequency parameters compared to the MCS results. A deterministic optimization is also performed to compare the optimum results with and without the effect of uncertainties. The differences on the optimum solutions of the deterministic and stochastic cases imply the necessity of considering uncertainties when modeling the materials. The multiple optimal microstructure designs are also identified by using the direct linear solver. Next, a parametric study is performed to analyze the mathematical definition of the ODF variations in the LP problem and its effect to the optimum result. Finally the LP solution algorithm is extended by assuming that the ODFs are dependent. In this case, the mean values and covariance elements of the stiffness parameters are assumed to be provided, and they are obtained by considering variations around a random texture design. The LP problem is solved to identify the mean values and covariance elements of the ODFs. The parametric study for the ODF variations shows that the optimum ODF solutions are very similar to the random texture as expected. The future effort in this field may focus on derivation of analytical techniques to represent joint probability distributions of

nonlinear material properties.

CHAPTER 6

Process-Texture-Property Identification

One of the important problems in engineering is the identification of the optimal processing route of the materials with desired texture and/or material properties. Manufacturability defines a natural constraint in design optimization problems, and needs to be studied comprehensively in computational models. To this end, Chapter 6 focuses on the problem of identifying the optimal processing route/routes to produce materials with optimized texture/properties. The motivation is to find out which of the multiple optimum ODF solutions identified in Chapter 3 can be manufactured using a set of deformation processes. The optimum ODF solutions are represented in material plane using the mathematical form given in Eq. 3.6. The texture evolution in a single/or a sequence of deformation processes can be shown using the ROMs for the ODFs. In this chapter, the POD technique is used to characterize the ODF evolution during different deformation processes. Each set of individual deformation processes/or each set of a sequence of processes is associated with a separate ROM representation generated with the POD technique. The POD of the deformation process represents the ODF solutions in process plane. The ODF solutions in the process plane are then projected to the material plane to minimize the differences between the ODF solutions/or desired material property values in process and material planes. This projection corresponds to an LP problem for matching the textures

and/or desired material properties. Two approaches are implemented to the LP solution framework. The first case aims to minimize the difference between the textures through minimization of the differences of the ODF values. The optimum processing route is determined as the route which provides the minimum difference between the ODF solutions in material and process planes. The second approach aims to minimize the difference between the desired material properties. The material property values can also be calculated in the process plane using the volume averaging equations with the POD representation of the ODF values. The desired material property values in the process plane are projected to the material plane where the optimum material properties are previously obtained. The LP problem identifies the optimum processing route to produce a material with desired material property values. In both cases the LP solutions are identified for single deformation processes as well as a sequence of deformation processes (including two or three deformation processes in sequence). The summary of the two approaches (texture and material property matching) is illustrated in Fig. 6.1.

The remainder of this chapter is organized as follows. Section 6.1 addresses the ROM formulation to represent the texture evolution during deformation processes. The LP problem definitions for texture and property matching approaches are presented in Section 6.2. The results for optimum processing routes are reported in Section 6.3. A summary of the chapter is given in Section 6.4.

6.1 Reduced order model of the ODF

The discussion here follows the work in [76, 78, 79] where model reduction of crystal plasticity was first introduced using the technique of POD. Model reduction involves generation of basis functions for representing ODFs obtained from a process path. Using such basis functions, any ODF, $A(r,t)$, from the time-history of ODF evolution in a given process can be approximated as follows:

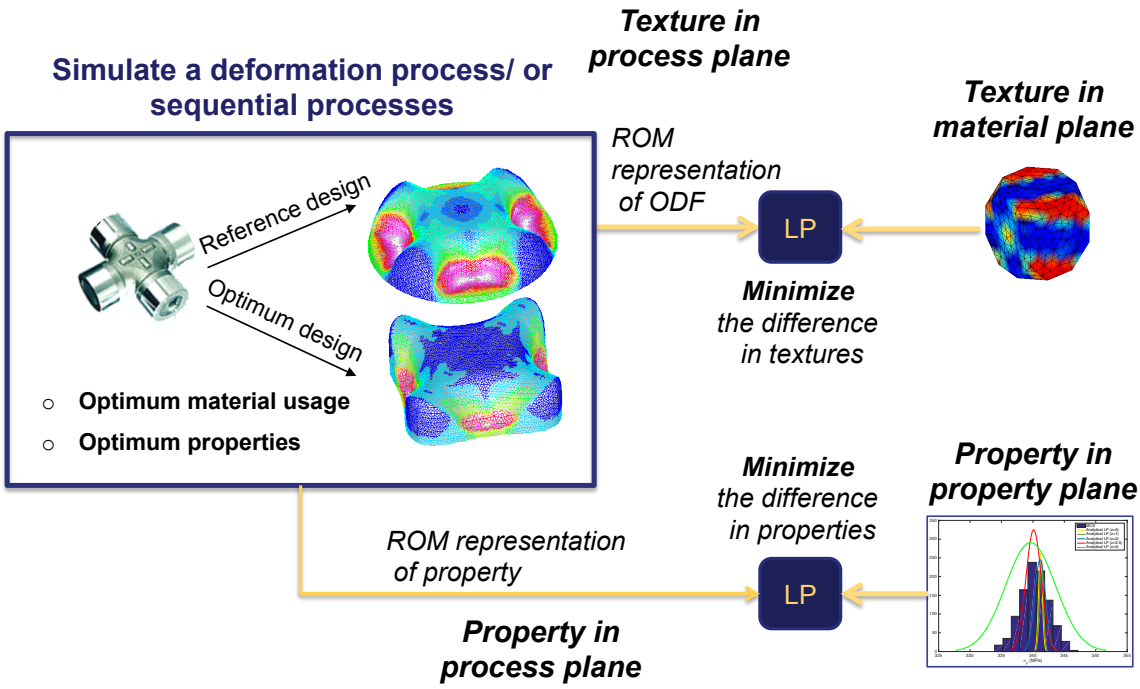

Figure 6.1: Optimum deformation process identification as an LP problem

$$A(r,t) = \sum_{m=1}^{b} a_m(t)\phi_m(r) \tag{6.1}$$

In the above equation ϕ_m represents 'b' basis functions (independent of time) and $a_m(t)$ denotes the corresponding time-dependent coefficients. Once such basis functions ϕ_m are computed, time-dependent coefficients can be used to reconstruct the textures arising from the process path. Readers are referred to [78] where texture evolution is computed by using the Eq. 6.1. Texture evolution can also be computed across a set of extrapolatory regimes of the process (i.e. conditions deviating from those used to generate the basis functions) using the same set of basis functions.

The 'method of snapshots' is an efficient technique of obtaining basis functions from an ensemble of ODF data, $A(r,t)_{i=1}^{\mathcal{N}}$, consisting of ODFs at various times during texture evolution over a deformation path. Here, the basis functions ϕ take the form [78]:

$$\phi_m = \sum_{i=1}^{\mathcal{N}} u_i^m A^i \tag{6.2}$$

where A^i represent textures from the ensemble, and u_i^m is determined by solving the following linear eigenvalue problem:

$$\boldsymbol{CU} = \boldsymbol{\Lambda U} \tag{6.3}$$

where $\boldsymbol{C}$ is the spatial correlation matrix defined as:

$$C_{ij} = \frac{1}{\mathcal{N}} \int_{\mathcal{R}} A^i(r) A^j(r) dv \tag{6.4}$$

$\boldsymbol{\Lambda}$ and $\boldsymbol{U}$ comprise of the eigenvalues and the eigenvectors of the system, respectively. To determine a suitable basis size, b, one must ensure that the eigen-modes selected capture as much 'system energy' as possible. This is possible by selecting the basis functions that correspond to the largest eigenvalues in $\boldsymbol{\Lambda}$. Once the modes have been evaluated, the optimal basis is generated from Eq. 6.2. The coefficients, a, corresponding to any ODF in a deformation path can be retrieved from:

$$a_m = \int_{\mathcal{R}} A(r) \phi_m dv \tag{6.5}$$

The space of reduced coefficients is called the process plane and satisfies the normalization and positiveness constraints of the ODF. The ODFs in a deformation path follow a curve in the space of reduced coefficients, a. The success of the technique for representing texture evolution was shown in [76, 78, 80] where just three basis functions were found to be sufficient for capturing most features of the evolving ODF in any given process or set of processes. Basis functions are obtained for different processing modes using a 448 element discretization of the fundamental region. Basis used in the examples consist of modes generated from an ensemble of data obtained

for tension, compression, shear and rotation processes up to time of 0.1 s when deformed with a strain rate of 1 s^{-1} using a time step of $\Delta t = 0.01$ s. The basis depends upon the initial texture $A(r, t = 0)$ that is used in the solution of ODF evolution. However, the strength of POD analysis used here lies in the fact that the reduced basis works in extrapolatory modes to represent texturing under various deviations in the initial texture. As a result, ODFs resulting from processing to a different strain or processing a starting texture that deviates from the one used to build the basis are well approximated using the same set of basis functions.

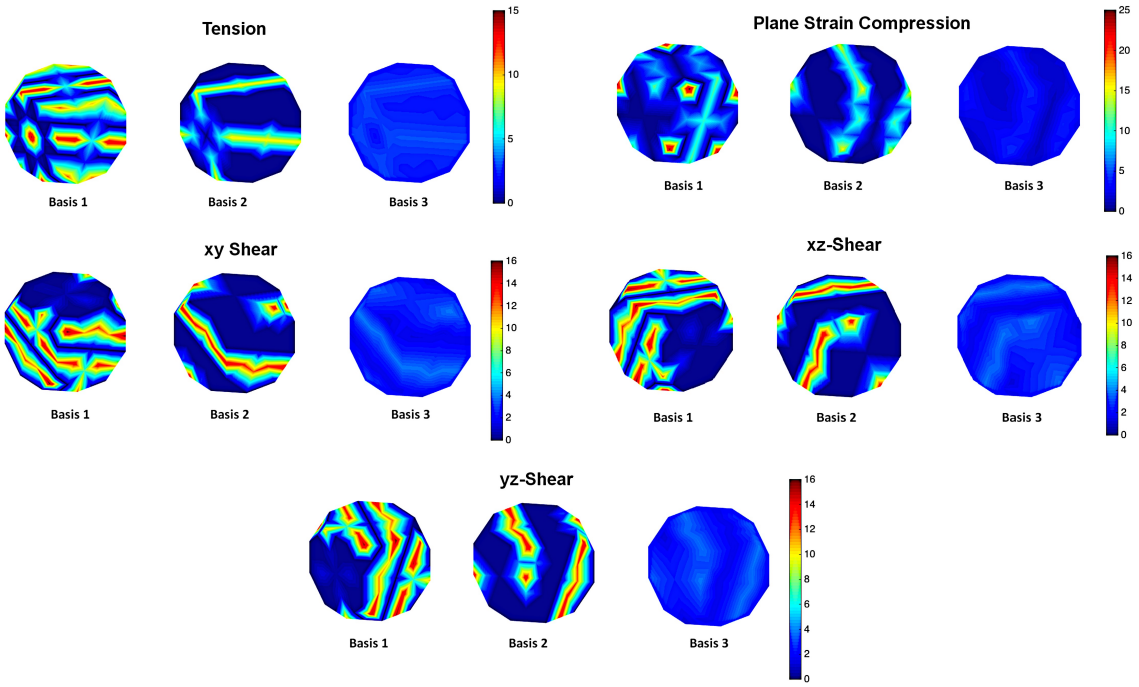

Figure 6.2: Basis functions of different deformation processes

Different basis functions are generated to simulate different process sequences [80]. Snapshots, which show the ODF values at different time steps, are taken to generate the POD representations. One POD representation is used to represent the texture evolution during a sequence of processes with two and three deformation processes. In this case, the initial texture of the second and third deformation processes are identified with the crystal plasticity simulations. The reduced models used to represent

the deformation paths are different, for example, when modeling tension process on a rolled specimen compared to a process of tension acting on an annealed specimen with random texture. The basis functions for the tension, plane strain compression and shear processes are shown in Fig. 6.2. The process planes for these processes are shown in Fig. 6.3 colored by a property (yield stress of the cantilever Galfenol beam). The POD representations of each of the deformation processes shown in Fig. 6.2 are developed using 10 snapshots with 3 basis functions. In addition to these deformation processes, xy-rotation, xz-rotation and yz-rotation deformation processes are also considered to generate the POD representations of sequential deformation processes. However, the inclusion of rotation processes is constrained in such a way that it is assumed that the rotations cannot be the first deformation process, and a rotation cannot be followed by any rotation.

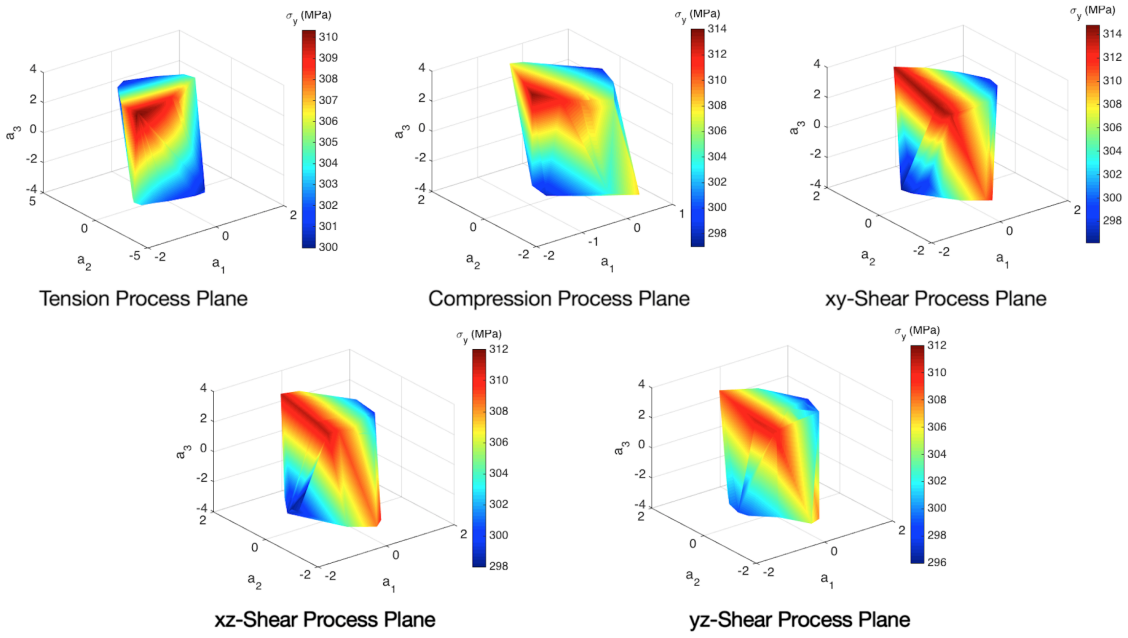

Figure 6.3: Property closures of different deformation processes

6.2 LP problem formulation for optimum deformation process identification

The LP problems which are solved to identify the optimum deformation processing route are categorized to two approaches. The first case identifies the deformation process which provides the closest texture match to the optimum design. The second approach finds the optimum deformation process which provides the closest values to the optimum material properties. The problem of process identification is solved using these two approaches by modeling the single or sequence of deformation processes with the POD. The same vibration tuning problem for a cantilever Galfenol beam, which is discussed in Chapter 3, is considered. The first LP problem is solved to identify the optimum processing route to provide a material design as close as to one of the multiple optimum designs of this Galfenol problem. The second LP problem determines the optimum processing route which can provide material property values as close as to the optimum values. The material properties considered in the LP problem are the 9 stiffness coefficients of the orthotropic beam as well as the yield stress.

6.2.1 Identification of the ODFs closest to an optimum ODF in the material plane

Five different processes are considered in this work. The ODFs from these processes are obtained using a specific macro-velocity gradient ($\boldsymbol{L}$) in the crystal plasticity solver [80] corresponding to these deformation processes. For example, the x–axis tension process is based on the following velocity gradient [80]:

$$\mathbf{L} = \alpha_1 \begin{bmatrix} 1 & 0 & 0 \\ 0 & -0.5 & 0 \\ 0 & 0 & -0.5 \end{bmatrix} \tag{6.6}$$

The location of optimal ODFs on the material plane does not convey information on how to realize such ODFs in practice. There may be several processing solutions to this problem. Here, a particular processing path is chosen and checked if it can closely produce one of the optimum textures. The optimum ODF from the material plane is assumed to be given by a perturbation, $\boldsymbol{r}$, to an ODF in the process plane. The perturbation is minimized in some sense such that an ODF from the process plane is as close as possible to the optimum ODF in the material plane. In this work, the optimum ODFs on the material plane are the optimum ODF values found for Galfenol vibration tuning problem in Chapter 3.

The optimum ODF in the process plane is written as $\boldsymbol{A_{opt}} = \sum_{m=1}^{b} a_m \phi_m + \boldsymbol{r} > \boldsymbol{0}$, where $\boldsymbol{A} = \sum_{m=1}^{b} a_m \phi_m$ provides the closest solution in the basis $\boldsymbol{\phi}$ and $\boldsymbol{r}$ is the perturbation (or error) between the optimum ODF in the material plane ($\boldsymbol{A_i} = \boldsymbol{A_1} + \lambda_i \boldsymbol{V_i}$) and the optimum ODF in the process plane. The normalization constraint is given as $\boldsymbol{q^T A_i} = 1$, and $\boldsymbol{q^T A} = 1$. The bound in the value of the solution ODF from the given ODF, $r_0 \geq 0$, is minimized. The problem is posed as $\min_a r_0$ such that $\sum_{m=1}^{b} a_m \phi_m + \boldsymbol{r} - \sum_{i=1}^{n} \lambda_i \boldsymbol{V_i} = \boldsymbol{A_1}$. Positivity of the optimal ODF dictates the constraints $\boldsymbol{A} \geq \boldsymbol{0}$ and $\boldsymbol{A_i} \geq \boldsymbol{0}$. In the solution procedure, the basis ($\boldsymbol{\phi_m}$) and the error ($\boldsymbol{r}$) are represented as a vector containing values at independent nodes (set of nodes representing distinct orientations while accounting for crystal symmetries). The ODFs in the process and material planes also require the positivity constraints: $\sum_{m=1}^{b} a_m \phi_m \geq 0$ and $\boldsymbol{A_1} + \sum_{i=1}^{n} \lambda_i \boldsymbol{V_i} \geq 0$. The additional constraint on the bound in the value of the solution ODF from the given ODF is defined as $|r_i| \leq r_0$ equivalent to pairs of linear inequalities: $-r_i - r_0 \leq 0$ and $r_i - r_0 \leq 0$, $i = 1, \ldots, N$, where N is the number of independent nodes. This problem uses $\boldsymbol{x} = [r_1, \ldots, r_N, \lambda_1, \ldots, \lambda_n, a_1, \ldots, a_b, r_0]^T$ as the variables to be identified. The error (r_i) from the nodal values of the optimum ODF is allowed to be of either sign. The implementation of the augmented system to the LP problem is given in details

below:

1. *Equality Constraints*

$$\sum_{m=1}^{b} a_m \phi_m + \boldsymbol{r} - \sum_{i=1}^{n} \lambda_i \boldsymbol{V_i} = \boldsymbol{A_1}$$
$$\boldsymbol{q^T}(\sum_{m=1}^{b} a_m \phi_m) = 1$$
$$\boldsymbol{q^T}(\sum_{i=1}^{n} \lambda_i \boldsymbol{V_i}) = 1 - \boldsymbol{q^T A_1} \tag{6.7}$$

Three basis functions $\boldsymbol{\phi_1}, \boldsymbol{\phi_2}$ and $\boldsymbol{\phi_3}$ with corresponding coefficients a_1, a_2 and a_3 are used to fully represent the ODFs during a particular process.

2. *Augmented System Combining the Equality Constraints*

The unknowns in the LP tableau are then written as:

$\boldsymbol{x} = [r_1, \ldots, r_N, \lambda_1, \ldots, \lambda_n, a_1, a_2, a_3, r_0]^T$. Thus, the augmented system combining the constraints in Eq. (6.7) can be written as $\boldsymbol{P_{aug}x = b}$ where $\boldsymbol{b} = [\boldsymbol{A_1^T},\ 1,\ 1 - \boldsymbol{q^T A_1}]^T$ and:

$$[\boldsymbol{P_{aug}}] = \begin{bmatrix} \boldsymbol{I_{N\times N}} & -\boldsymbol{V_1} & \ldots & -\boldsymbol{V_n} & \boldsymbol{\phi_1} & \boldsymbol{\phi_2} & \boldsymbol{\phi_3} & \boldsymbol{0_{N\times 1}} \\ \boldsymbol{0_{1\times N}} & 0 & \ldots & 0 & \boldsymbol{q^T\phi_1} & \boldsymbol{q^T\phi_2} & \boldsymbol{q^T\phi_3} & 0 \\ \boldsymbol{0_{1\times N}} & \boldsymbol{q^T V_1} & \ldots & \boldsymbol{q^T V_n} & 0 & 0 & 0 & 0 \end{bmatrix}$$

where $\boldsymbol{I_{N\times N}}$ is an $N\times N$ identity matrix. The notation of $\boldsymbol{0_{N\times 1}}$ and $\boldsymbol{0_{1\times N}}$ indicates row and column vectors of zeros respectively.

3. *Inequality Constraints*

Similar augmentations are performed for the inequality constraints for the prob-

lem given as:

$$\begin{aligned} -r_i - r_0 &\leq 0 \\ r_i - r_0 &\leq 0 \\ \sum_{m=1}^{b} a_m \phi_m &\geq 0 \\ \boldsymbol{A_1} + \sum_{i=1}^{n} \lambda_i \boldsymbol{V_i} &\geq 0 \end{aligned} \tag{6.8}$$

4. *Augmented System Combining the Inequality Constraints*

   The augmented system combining the constraints in Eq. (6.8) can be written as $\boldsymbol{M_{aug}x} \leq \boldsymbol{c}$ where $\boldsymbol{c} = [\boldsymbol{0_{1\times N}},\ \boldsymbol{0_{1\times N}},\ \boldsymbol{0_{1\times N}},\ \boldsymbol{A_1^T}]^T$, and each row of $\boldsymbol{M_{aug}}$ corresponds to the inequalities in Eq. (6.8) as indicated below:

$$[\boldsymbol{M_{aug}}] = \begin{bmatrix} -\boldsymbol{I_{N\times N}} & 0 & \dots & 0 & 0 & 0 & 0 & -\boldsymbol{1_{N\times 1}} \\ \boldsymbol{I_{N\times N}} & 0 & \dots & 0 & 0 & 0 & 0 & -\boldsymbol{1_{N\times 1}} \\ \boldsymbol{0_{N\times 1}} & 0 & \dots & 0 & -\boldsymbol{\phi_1} & -\boldsymbol{\phi_2} & -\boldsymbol{\phi_3} & 0 \\ \boldsymbol{0_{n\times N}} & -\boldsymbol{V_1} & \dots & -\boldsymbol{V_n} & 0 & 0 & 0 & 0 \end{bmatrix}$$

   The notation $\boldsymbol{1_{N\times 1}}$ indicates a vector of ones. The objective is to minimize the bound on the error $\boldsymbol{r}$ given by r_0. The objective is given as $\boldsymbol{f^T x}$ where:

$$\boldsymbol{f} = \begin{bmatrix} \boldsymbol{0_{1\times N}} & \boldsymbol{0_{1\times n}} & \boldsymbol{0_{1\times 3}} & 1 \end{bmatrix}^T$$

5. *Final LP Problem*

   Thus, the final LP problem reduces to the solution of the following problem:

$$\min_{a} \boldsymbol{f^T x} \text{ satisfying the constraints}$$

$$\boldsymbol{P_{aug} x = b}$$

$$\boldsymbol{M_{aug} x \leq c}$$

6.2.2 Identification of the ODFs to obtain material properties closest to a desired set of properties

Similar to the optimization problem described in Section 6.2.1 where the process plane ODFs closest to the optimum ODFs in the material plane are identified, another optimization problem can be posed where the objective is to identify the ODFs in the process plane that closely reproduce a desired set of properties. The optimization problem in this case is posed so as to identify the ODFs in the process plane whose properties are closest to a desired set of properties in some sense. This approach is beneficial since the optimum ODFs in the process plane will provide the closest match to the desired property values produced by the optimum ODF solution in the material plane. Even though the problem definition does not provide any control on the ODF values of the material plane, there is still a good possibility of matching the textures in the material and process planes due to matching multiple properties. The objective is to minimize the bound ($e_0 \geq 0$) on the absolute value of error from a desired property: $\min_{a} e_0$ such that $\sum_{m=1}^{b} \boldsymbol{p^T} \phi_m a_m + \boldsymbol{p^T e} = \boldsymbol{d}$, where $\boldsymbol{d}$ is the desired set of properties. The normalization constraint is given as $\sum_{m=1}^{b} \boldsymbol{q^T} \phi_m a_m = 1$. Positivity of the ODF dictates the constraint $\sum_{m=1}^{b} \phi_m a_m \geq 0$. Bound on the absolute value of error is defined as $|e_i| \leq e_0$. This is equivalent to pairs of linear inequalities: $-e_i - e_0 \leq 0$ and $e_i - e_0 \leq 0$, where $i = 1, \ldots, n_p$, where n_p denotes the number of properties to be optimized. This problem uses $\boldsymbol{x} = [e_1, \ldots, e_{n_p}, a_1, \ldots, a_b, e_0]^T$ as the variable to be identified. The error, $\boldsymbol{e_i}$, is allowed to be of either sign. The

initial desired properties are the design objective (yield stress) and design constraints (natural frequencies) of the Galfenol vibration tuning optimization problem. The computation of natural frequencies is not linear but it is dependent on the stiffness values. Thus the stiffness parameters, which are calculated with averaging equations, are considered as the representative linear quantities of the design constraints. So, the final desired properties are selected as optimum values of the yield stress and 9 independent orthotropic stiffness elements of the vibration tuning problem. The implementation of the augmented system to the LP problem is given in details below:

1. *Equality Constraints*

$$\begin{aligned} \boldsymbol{p^T}(\sum_{m=1}^{b} a_m\phi_m + \boldsymbol{e}) &= \boldsymbol{d} \\ \boldsymbol{q^T}\sum_{m=1}^{b} a_m\phi_m &= 1 \end{aligned} \tag{6.9}$$

   Three basis functions $\boldsymbol{\phi_1}, \boldsymbol{\phi_2}$ and $\boldsymbol{\phi_3}$ with corresponding coefficients a_1, a_2 and a_3 are used to fully represent the ODFs during a particular process.

2. *Augmented System Combining the Equality Constraints*

   The unknowns in the LP tableau are then written as $\boldsymbol{x} = [e_1, \ldots, e_{n_p}, a_1, a_2, a_3, e_0]^T$. Thus, the augmented system combining the constraints in Eq. (6.9) can be written as $\boldsymbol{P_{aug}x = b}$ where $\boldsymbol{b} = [\boldsymbol{d}, \ \ 1]^T$ and:

$$[\boldsymbol{P_{aug}}] = \begin{bmatrix} \boldsymbol{p^T} & \boldsymbol{p^T\phi_1} & \boldsymbol{p^T\phi_2} & \boldsymbol{p^T\phi_3} & 0 \\ \boldsymbol{0^T_{n_p\times 1}} & \boldsymbol{q^T\phi_1} & \boldsymbol{q^T\phi_2} & \boldsymbol{q^T\phi_3} & 0 \end{bmatrix}$$

3. *Inequality Constraints*

   Similar augmentations are performed for the inequality constraints for the prob-

lem given as:

$$\begin{aligned} -e_i - e_0 &\leq 0 \\ e_i - e_0 &\leq 0 \\ \sum_{m=1}^{b} a_m \phi_m &\geq 0 \end{aligned} \tag{6.10}$$

4. *Augmented System Combining the Inequality Constraints*

   The augmented system combining the constraints in Eq. (6.10) can be written as $\boldsymbol{M_{aug}x} \leq \boldsymbol{0}$ where each row of $\boldsymbol{M_{aug}}$ corresponds to the inequalities in Eq. (6.10) as indicated below:

$$[\boldsymbol{M_{aug}}] = \begin{bmatrix} -\boldsymbol{I_{n_p \times n_p}} & \boldsymbol{0_{n_p \times 1}} & \boldsymbol{0_{n_p \times 1}} & \boldsymbol{0_{n_p \times 1}} & -\boldsymbol{1_{n_p \times 1}} \\ \boldsymbol{I_{n_p \times n_p}} & \boldsymbol{0_{n_p \times 1}} & \boldsymbol{0_{n_p \times 1}} & \boldsymbol{0_{n_p \times 1}} & -\boldsymbol{1_{n_p \times 1}} \\ \boldsymbol{0_{n_p \times n_p}} & -\boldsymbol{\phi_1} & -\boldsymbol{\phi_2} & -\boldsymbol{\phi_3} & \boldsymbol{0_{n_p \times 1}} \end{bmatrix}$$

   The objective is to minimize the bound on the error $\boldsymbol{e}$ given by e_0. The objective is given as $\boldsymbol{f^T x}$ where:

$$\boldsymbol{f} = \begin{bmatrix} \boldsymbol{0_{1 \times N}} & \boldsymbol{0_{1 \times 3}} & 1 \end{bmatrix}^T$$

5. *Final LP Problem*

   Thus, the final LP problem reduces to the solution of the following problem:

$$\begin{aligned} \min_{a} \boldsymbol{f^T x} \text{ satisfying the constraints} \\ \boldsymbol{P_{aug} x} &= \boldsymbol{b} \\ \boldsymbol{M_{aug} x} &\leq 0 \end{aligned}$$

6.3 Results

This section reports the results for the optimum process identification problems which are posed to find the closest texture and material properties using a single deformation process or a sequence of two or three deformation processes. The problems are also implemented to a global optimization framework, which utilizes the NSGA-II algorithm, to identify the optimum maximum strain rates of the processes. In the cases where a sequence of deformation processes is considered the order of these processes requires another optimization sub-problem, which is solved with a simple integer optimization method through assigning different integer values to different deformation processes.

6.3.1 Results for the closest ODF identification problem

The objective is to identify the location $\{a_1, a_2, a_3\}$ on the process plane which best represents the optimum ODFs on the 'material plane' computed for the Galfenol beam vibration tuning problem. Tension, plane strain compression and shear are selected as the particular processes when optimizing for the single processes while additional rotation deformation processes are also considered to identify the optimum route of the sequential deformation processes. The basis functions are computed to represent the ODF evolution in these processes. The augmented LP problem is solved for each of these individual processes to identify the closest ODFs on each process plane to the optimum ODFs on the material plane. The values of the objective functions of the LP problems, $min\ r_0$ and $max\ \sigma_y$, are compared for optimum single process and optimum sequence of processes in Table 6.1. It should be noted that the optimum ODF of the vibration tuning problem provided a yield stress value of 308.4456 MPa as shown in Table 3.3, and the ODFs on the process plane are expected to provide a close value to the optimum yield stress value.

The results in Table 6.1 indicate that the ODFs can provide similar values to the

Table 6.1: LP problem results for ODF matching on material and process planes

Process number	Process order	r_0	σ_y (MPa)
1	Tension	0.4689	300.0880
2	Compression - Tension	0.3802	299.2848
3	Tension - yz-Rotation - Tension	0.4249	299.6211

highest yield strength when a single or a sequence of deformation processes is applied. The objective, $min\ r_0$, shows the maximum error value among all the ODF value differences in the process and material planes. Thus, the other error values are less than the objective function value. Since the main objective of this section is to find the best match for the optimal ODF, tension is the optimum single deformation process to produce the desired texture owing to its smallest r_0 value among all the single deformation processes. The implementation of a sequence of deformation processes increases the variability in texture, and hence the probability of matching. Therefore the sequence of deformation processes provides smaller r_0 values compared to the single deformation process solutions. However, the error on the optimum objective function values increases when a sequence of deformation processes is considered. The reason of this is the fact that the LP problem here is posed to match the textures, and it does not have any design criteria on the property matching. The optimum material property value should be expected to be closer in the property matching approach where the results will be reported in the next section. The closest microstructure designs on the process plane with this approach (ODF matching) to the optimum microstructure on the material plane are shown in Fig. 6.4. In Fig. 6.4, Rate represents the optimum maximum strain rate parameter obtained with NSGA-II. The microstructure design in Fig. 6.4 shows a similar ODF distribution pattern compared to tension process basis functions in Fig. 6.2. Thus, this microstructure design via tension deformation process ensures the possibility of manufacturing a very similar ODF to one of the optimum solutions to the Galfenol beam vibration tuning problem.

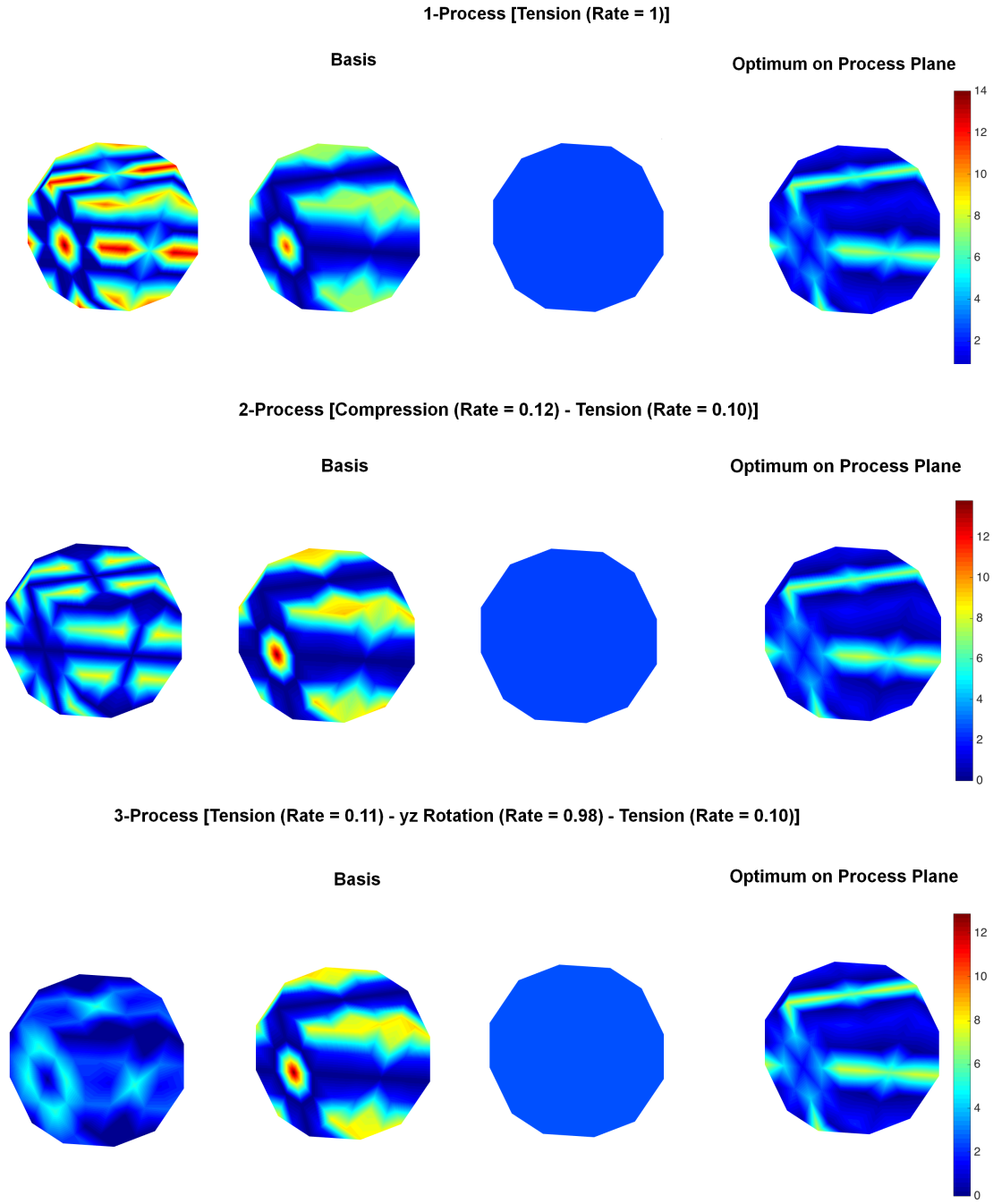

Figure 6.4: Optimum microstructures on process planes identified with ODF matching approach

6.3.2 Results for the closest material properties identification problem

The problem is to identify the point on a process plane that best represents optimum ODFs in the material plane with desired stiffness properties (C_{11} = 281.5559 GPa, C_{12} = 137.3222 GPa, C_{13} = 139.5597 GPa, C_{22} = 296.9677 GPa, C_{23} = 124.1479 GPa, C_{33} = 294.7302 GPa, C_{44} = 70.3946 GPa, C_{55} = 85.8063 GPa, C_{66} = 94.2138 GPa) and yield stress (σ_y = 308.4456 MPa) of the optimum design. The objective function of the LP problem is a measure of the maximum error between the desired property values in the material and process planes. The problem is solved for single and sequence of deformation processes. The optimum results for the objective functions of the LP problems ($min\ e_0$ and $max\ \sigma_y$) are shown in Table 6.2.

Table 6.2: LP Problem results for desired properties matching on material and process planes

Process number	Process order	e_0	σ_y (MPa)
1	xz-Shear	1.93388	309.0784
2	xz-Shear - xz-Shear	1.9336	308.6296
3	xy-Shear - yz-Rotation - xz-Shear	1.9213	308.4964

The selection of the optimum processing route, which provides the closest desired material property values, does not depend on the minimum value of e_0 this time since the sensitivity of stiffness parameters to the problem objective is different, and all e_0 values are close to each other. The optimum process is chosen according to the optimum yield stress value matching. According to this criterion, xz-Shear is the optimum single process for this problem. The increase in variability in textures with the introduction of the sequence of deformation processes also provides a better match for the optimum yield stress value. However, all the results, including the optimum single deformation process case, indicate a good match with the desired property values compared to the results for the ODF matching problem in the previous section. This is because the optimum process identification problem for the

optimum properties does not have any restriction on the texture, which leads to a less complicated LP problem with less number of variables. Both ODF and property matching LP problems are underdetermined problems due to the number of the ODF values to represent the Galfenol problem. Therefore the use of less number of variables leads to better solutions for the property matching problem. The difference in problem definitions also leads to different optimum solutions for both approaches. The closest microstructure designs on the process plane with this approach (property matching) to the optimum microstructure on the material plane are shown in Fig 6.5. In Fig. 6.5, Rate represents the optimum maximum strain rate parameter obtained with NSGA-II.

6.4 Conclusion

In this chapter, an optimization methodology for processing route identification is developed for structural problems with a set of macroscale engineering design objectives. An approach to identify the microstructures which can be manufactured using a known set of deformation processes is presented. The ODFs during a particular deformation process or a sequence of deformation processes are represented using the POD technique with method of snapshots. The optimum processing route is determined by minimizing the distance between any one of the optimum ODF solutions on the material plane and the ODF values on the process plane using an augmented linear solver. Another approach where the optimum set of material properties are directly projected onto the process plane is also developed. The methods are demonstrated on the application problem, which is previously discussed in Chapter 3 for the vibration tuning of a Galfenol beam. The maximum strain rates of the deformation processes are also optimized through the implementation of a genetic algorithm. An integer based sub-optimization problem is solved to identify the optimum order of the deformation processes for the sequential process optimization. The sequence of

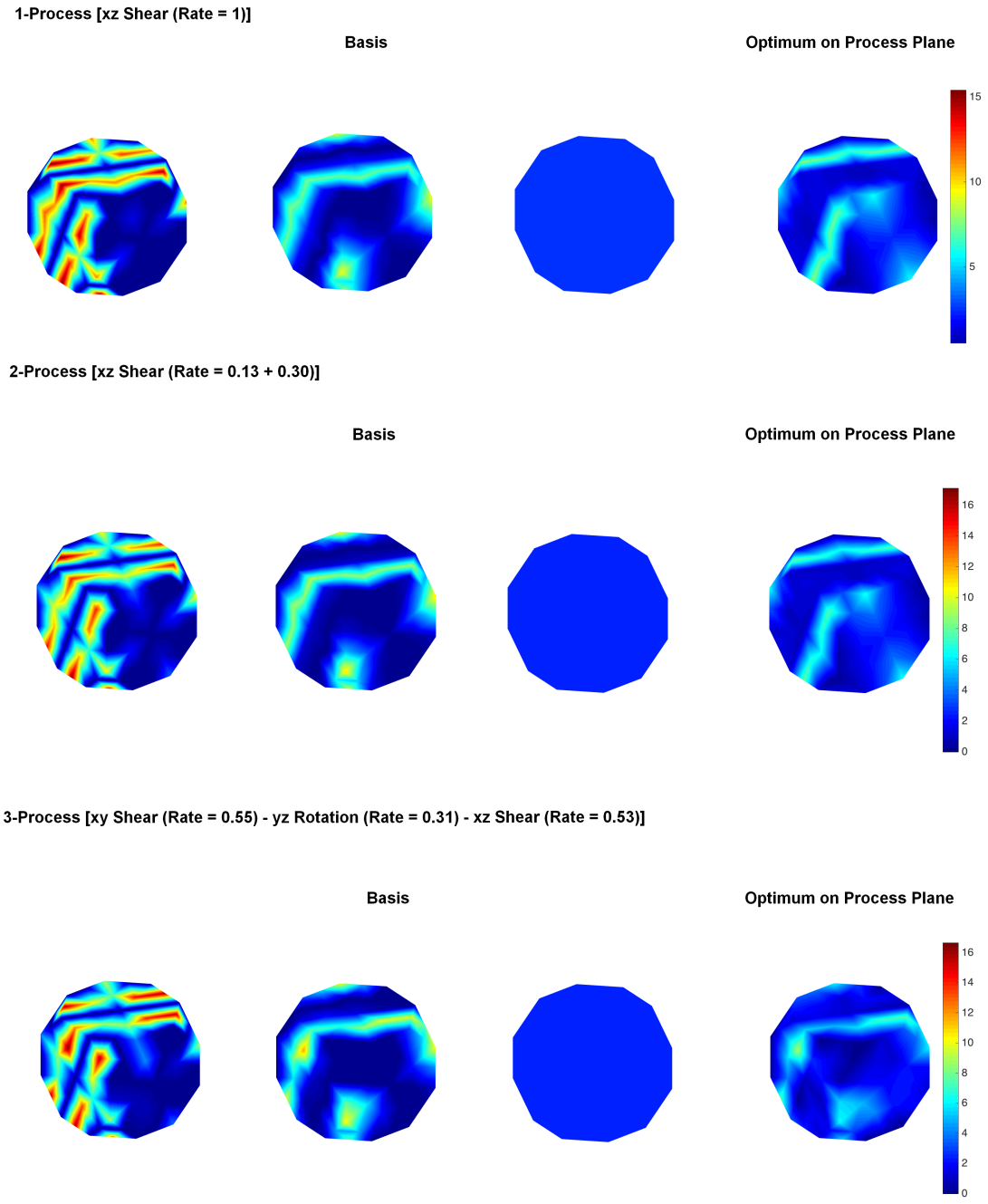

Figure 6.5: Optimum microstructures on process planes identified with property matching approach

deformation processes is observed to increase the variability in texture, and therefore leads to better matches in both approaches. However, the results in both cases

provide good matches for the property matching problem compared to the texture matching owing to the problem definition with less number of design variables.

CHAPTER 7

Future Directions on Multi-Scale Modeling of Microstructures

Prediction and control of texture evolution in a deformation process are important for the purposes of material design. Some of the modeling efforts concentrate on discrete aggregate models based on FE analysis [81, 82, 83, 84, 85]. However, some of the other studies, model texture evolution by quantifying the microstructure with probability descriptors [38, 40, 77, 80]. The microstructure modeling in the present work is also based on the quantification of the microstructure using a probabilistic descriptor, ODF. The ODF representation is extremely compact in comparison to discretized microstructures used in CPFE, leading to significant speed up in microstructure analysis. However, the ODF representation does not contain information about the local neighborhood of crystals. Thus, equilibrium across grain boundaries cannot be captured and a Taylor assumption [81], where all crystals deform identically, is used. Such a constraint leads to a stiff upper bound stress response, textures that are sharper than measured and texture components that cannot be captured [8]. To improve upon the microstructure description, higher order descriptors that can capture the statistics of crystal neighborhood are required [86, 87, 88, 89, 90]. The next level of descriptors, the two-point orientation correlation function (OCF), $\boldsymbol{F(g', g, r)}$, gives the probability density of finding orientations $\boldsymbol{g'}$ and $\boldsymbol{g}$ at the end points of a randomly

placed vector, $\boldsymbol{r}$, within the microstructure. This descriptor contains neighborhood information and holds the promise of modeling grain equilibrium, thereby relaxing the Taylor assumption. Representations of the OCF in the form of global approximations (exponentially decaying functions based on the Corson's model [91, 92] and Fourier space representations [93]) and local approximations (based on FEs, [94]) have been studied in the past. However, the two-point measure is high dimensional (e.g. OCF for a 3D polycrystal is 9-dimensional) and there is still a significant need for reduced representations. Considerable improvements in OCF representation can be realized by including the physics of deformation processes. For example, in viscoplastic self consistent (VPSC) schemes, a Green's function models the interaction between crystals [84, 95]. The function decays with distance and can be used to estimate a cut-off radius beyond which correlation information is redundant [94]. However, this radius may encompass several grains and storage requirements are still significant. In this chapter, a two-point OCF type of probabilistic technique, the NNOCF, is exercised to capture the higher order features of the texture using the input of time snapshots taken from the phase field simulations of a α-Ti material. The NNOCF is a conditional OCF truncated to the nearest neighbors. The descriptor is extremely compact and it can be used to locally enforce equilibrium (in an average sense) for each orientation using a novel finite differencing scheme. In this study, only deformation processes are studied. Another issue is to model heat treatment processes, which are traditionally done using phase field methods. ODF descriptor can be mapped to phase field outputs. There are some similar studies in literature focusing on the quantification of the microstructure with two-point statistics using CPFE and phase field simulations. For example, Paulson et. al [96] analyzed the two-point statistics of the microstructures through implementing the Principal Component Analysis (PCA) scheme to generate the reduced basis to represent the CPFE simulations of α-Ti material. Yabansu et. al [97] extended this study by applying the PCA to extract the

microstructural data from the phase field simulations. Considering the computationally expensive nature of the phase field simulations as well as the large variations in the microstructural texture during the simulations, the ROM techniques, such as PCA or POD, are not found to be efficient in the application problem of this study discussed in Section 7.1. The first reason is that neither one-point nor two-point statistics are completely accurate to represent the changes in all the grain structures over time (the snapshots used in this work usually have over 800 grains). Another reason is that the ROM techniques require a great amount of snapshots to accurately generate a surrogate for the actual texture evolution. The surrogate model can be generated using less number of snapshots either by satisfying a lower accuracy level, or if the changes in the microstructural texture are small. However, phase field simulations can model significant changes in different grain structures, and therefore the PCA representations are not computationally efficient. In this section, we present a preliminary study of using NNOCF to model phase field outputs. Here, the ODF and NNOCF values are calculated using 9 discrete snapshots, and the overall stress-strain curve of the α-Ti material is predicted using these discrete snapshots, and compared to the FE results. The future focus should be on implementation of a multi-fidelity modeling approach to represent the microstructure (inputting experimental data or phase field simulations) using different techniques depending on the sensitivity level. Considering the requirement for modeling the epistemic uncertainties introduced by the use of the point statistical methods to quantify the microstructure, multi-fidelity modeling will be beneficial in large variety of applications in ICME.

Another important future topic in materials engineering is multi-scale modeling of composite materials. The microstructure modeling methodology discussed in this work has particularly applied to the design problems with metals and metallic alloys. However, the extension of these techniques to the modeling and design of composite materials is important considering the growing use of composites in different areas

including aircrafts. Therefore the multi-scale modeling and design optimization of composite materials using the probabilistic descriptor based approaches are suggested as a research direction which should be pursued in future. The multi-scale modeling can be extended in future to study the atomistic level features, which will be beneficial to the design of nano-composites. The design framework can employ the proposed multi-fidelity approach which implements one-point or two-point statistics interchangeably to satisfy the accuracy and computational efficiency expectations. The modeling of uncertainties through the multi-scale analysis is also necessary to satisfy the performance needs of engineering structures. The analytical UQ algorithm, developed in this work, can be used to study the quantification and propagation of the uncertainties in composite materials. However, this methodology can further be advanced, or some numerical techniques can be implemented to compute the uncertainty propagation for more complex design criteria. The ultimate goal for future research in multi-scale design of materials should focus on automated 3D multi-scale modeling, design and optimization strategies for different materials (such as metals, metallic alloys, composites, ceramics, etc.) through the mixed use of probabilistic descriptor based approaches and FE by accounting for aleatoric and epistemic uncertainties. The proposed future research areas are discussed in more details in the following sections.

7.1 Higher order probabilistic features and multi-fidelity design approach

The accuracy needs for challenging material design problems brings about another question: which modeling algorithm to choose? Not only the accuracy expectation but also the computational time limitations have a significant effect on the selection of the appropriate solution strategy. One example application for this accuracy need

can be the modeling of microstructural features after an advanced manufacturing technique is applied to the material. The deformation processes, which were modeled in Chapter 6, are classical techniques. Going beyond these classical manufacturing techniques one may need to use more advanced algorithms to capture the features of the microstructural texture better. An example EBSD data, which is taken after an additive manufacturing technique, known as Laser Engineered Net Shaping (LENS), is applied to a representative microstructure, is shown in Fig. 7.1 [98]:

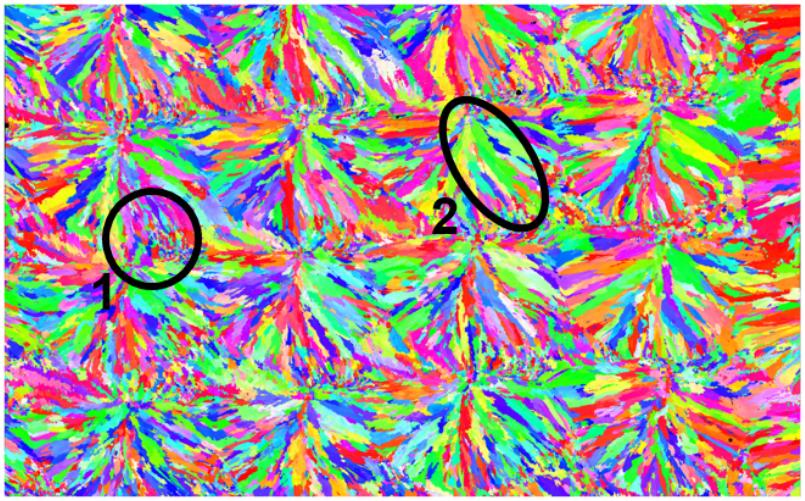

Figure 7.1: A representative EBSD plot for the LENS microstructure [98]

As represented by Fig. 7.1, the EBSD data, which indicates the texture information of the microstructure after an additive manufacturing technique is applied, is more complicated than the EBSD data previously illustrated in Chapter 4. The quantification of the microstructural texture here needs a more accurate representation for the properties. Here, one higher order approach can be the NNOCF. The NNOCF, $F(\boldsymbol{g'}|(\boldsymbol{g},\boldsymbol{r}))$, gives the probability density of occurrence of an orientation $\boldsymbol{g'}$ at the end point of a vector $\boldsymbol{r}$ (of one pixel length) emanating from a given orientation $\boldsymbol{g}$. Fig. 7.2 [99] illustrates the NNOCF calculation scheme for a microstructure. The NNOCF is also represented in the FE discretized fundamental region (called mesh $M_{g'|g,r}$) in Fig. 7.2 [99]. In a 2D model of the microstructure, four such meshes are

needed at every node point in M_g corresponding to the four nearest neighbor pixels.

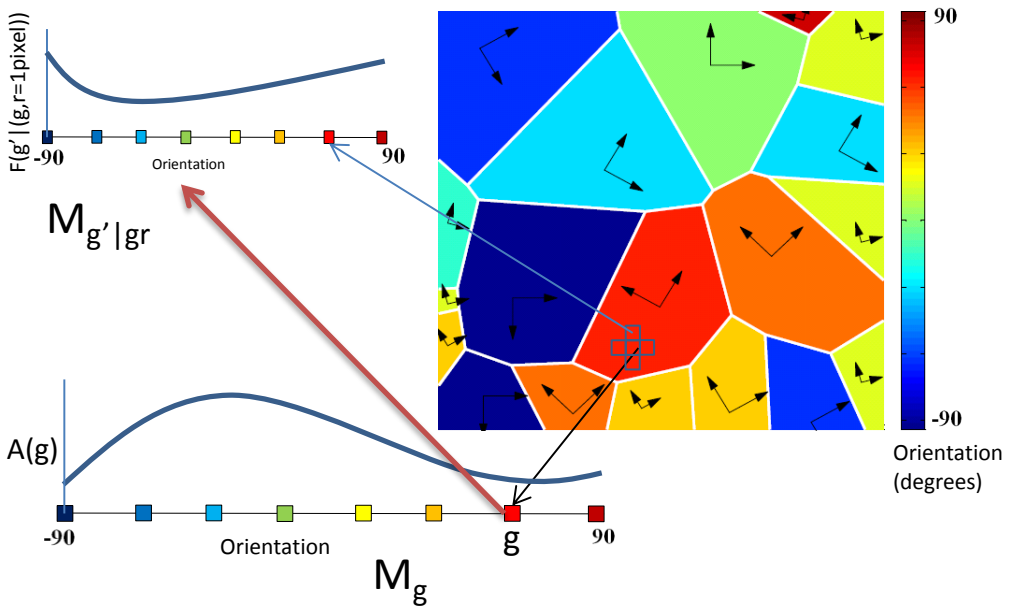

Figure 7.2: The NNOCF sampling from a microstructure (color coded based on grain orientation). The FE mesh M_g represents the volume density of each orientation (color). The volume density of each orientation (color) is represented by the NNOCF mesh $M_{g'|gr}$ attached to a node g in mesh M_g for the nearest neighbor pixels of g [99]

The NNOCF and ODF satisfy the following conservation equations at all times during deformation respectively:

$$\int F(\boldsymbol{g'}|(\boldsymbol{g},\boldsymbol{r}))d\boldsymbol{g'} = 1, \quad F(\boldsymbol{g'}|(\boldsymbol{g},\boldsymbol{r}))d\boldsymbol{g'} \geq 0 \tag{7.1}$$

$$\int A(\boldsymbol{g'})d\boldsymbol{g'} = 1, \quad A(\boldsymbol{g'}) \geq 0 \tag{7.2}$$

In addition to the above constraints, the orientation space corresponding to all possible $\boldsymbol{g}$'s must satisfy the crystallographic symmetries of the chosen system and the switching symmetry of the two-point measure, given as:

$$F(\boldsymbol{g}|(\boldsymbol{g'},\boldsymbol{r}))P(\boldsymbol{r}|\boldsymbol{g'})A(\boldsymbol{g'}) = F(\boldsymbol{g'}|(\boldsymbol{g},\boldsymbol{r}))P(\boldsymbol{r}|\boldsymbol{g})A(\boldsymbol{g}) \tag{7.3}$$

where $P(\boldsymbol{r}|\boldsymbol{g})$ gives the probability density of occurrence of vector $\boldsymbol{r}$ from a location with orientation $\boldsymbol{g}$, which accounts for the finite size of the sampled microstructure [94]. The details about the NNOCF approach such as the algorithm, probability update and constitutive modeling can be found in details in [12, 17, 81, 82, 100, 101, 102, 103, 104, 105, 106, 107, 108, 109, 110]. An example application is discussed here to compare the accuracy of the NNOCF approach to the ODF and FE techniques. For this application, the time snapshots showing the temporal evolution of the α-Ti microstructure are taken during the phase field simulations for cylindrical grains. The ODF and NNOCF representations are shown for each snapshot of each case. For this introductory study 10 independent ODF values and the corresponding 10×10 NNOCF matrix are used to model the texture. The evolution of the grains for different cases is illustrated through the evolution of the values in the ODF vector and NNOCF matrix. The global stress-strain curve is also computed for different grain structures using the Taylor assumption for the ODF and NNOCF representations, and FE to compare the results of the probabilistic modeling schemes.

7.1.1 Cylindirical grains

The evolution of the microstructure having cylindrical grain structure during the phase field simulations is shown in Fig. 7.3 and 7.4.

The ODF and NNOCF snapshots, shown in Fig. 7.3 and 7.4, depict similar features for microstructures evolution during the phase field simulations.

7.1.2 Discussion

The change in grain structure also affects the global material parameters. This effect is analyzed by calculating the global stress-strain curve of the microstructure during the phase field simulations. The stress-strain curve is calculated for the final time snapshot using the ODF, NNOCF and FE representations in Fig. 7.5. The

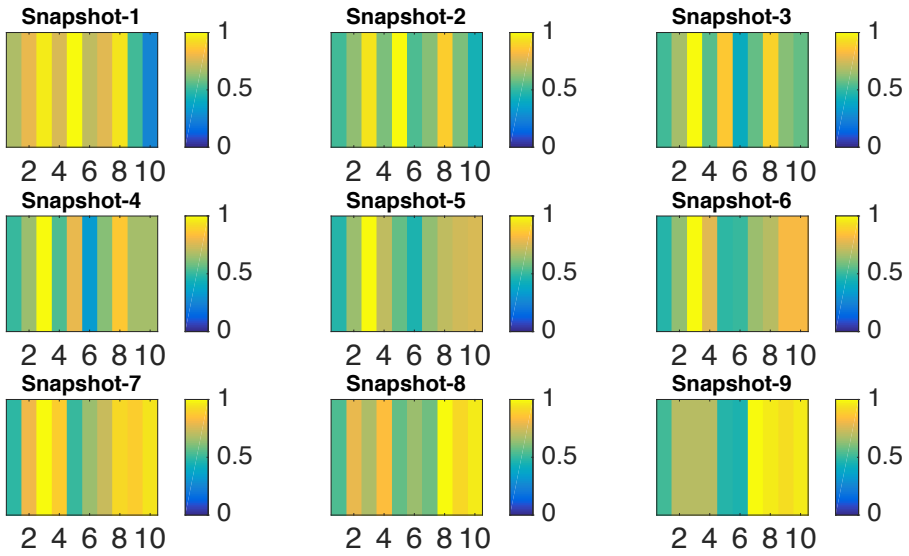

Figure 7.3: The ODF representation for the texture evolution of a microstructure with cylindrical grains during phase field simulation

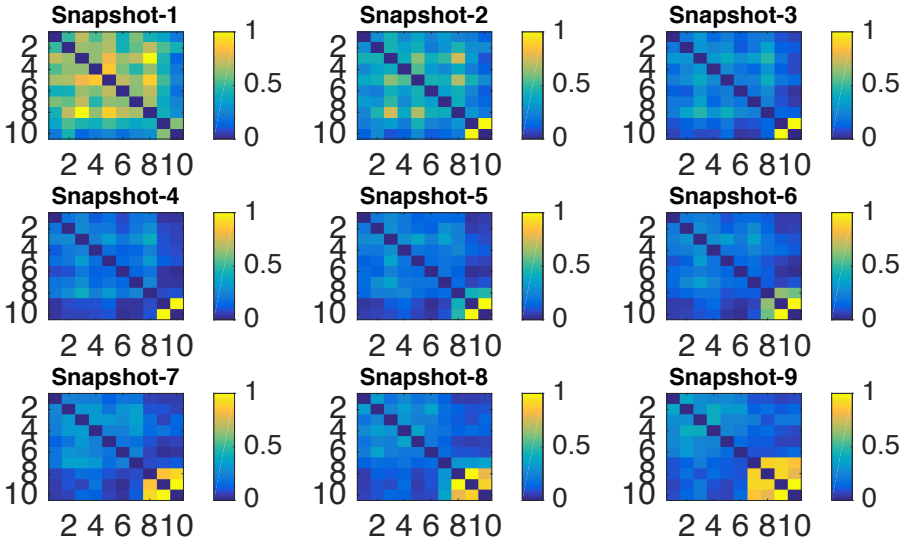

Figure 7.4: The NNOCF representation for the texture evolution of a microstructure with cylindrical grains during phase field simulation (only the cross-diagonal terms in the NNOCF matrix)

methods are available in another paper [99], and only the effect of adding neighborhood information is shown. FE analysis is taken to be the ground truth, as it models the complete microstructure.

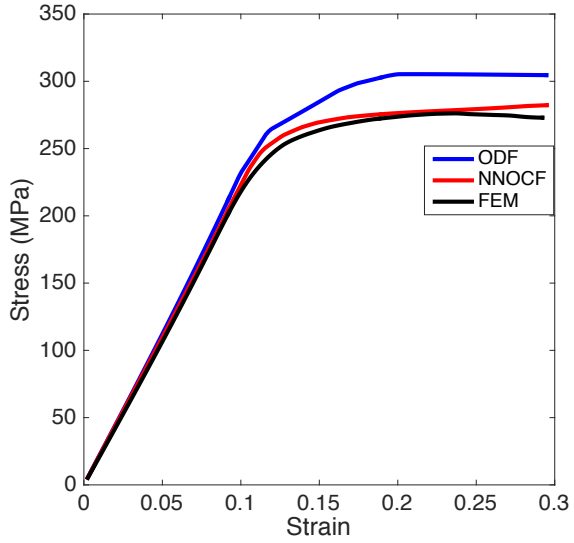

Figure 7.5: The stress-strain curves predicted using the ODF, NNOCF and FE representations

The NNOCF representation includes higher order terms compared to the ODF approach to model the correlations. Therefore it is expected to be more accurate (as indicated in Fig. 7.5) in terms of calculating properties. Hence, it should be more preferable to the ODF modeling when the major concern is the accuracy. On the other hand, one needs to implement the classical FE to investigate the grain shape effects more realistically, especially in grain level. However, not only the classical FE but also the higher order probabilistic descriptors, such as the NNOCF, is at least one order of magnitude slower than the ODF approach. Acknowledging the satisfactory results of the ODF it is still the most preferable technique in many applications as a result of its computational efficiency. Considering the high performance computing applications which are required for materials design, such as optimization and UQ, one better approach that should be implemented in future, is to use these lower and higher order models interchangeably to balance the needs for accuracy and computational time efficiency. This methodology is known as "multi-fidelity modeling", and it has been studied extensively in different disciplines such as fluid mechanics

[111, 112, 113] and solid mechanics [114, 115, 116, 117]. However, its application area has not been extended to materials modeling, especially to microstructural level. Considering the most common application areas of multi-fidelity modeling, which are observed as UQ, optimization and optimization under uncertainty respectively [118], it is a certain requirement to implement this modeling approach to materials design problems to satisfy the accuracy and computational time constraints at the same time. A detailed review of the multi-fidelity modeling techniques is presented in [118]. They observed that the multi-fidelity modeling approach in solid mechanics problems usually considers the analytical techniques as the low fidelity approach. One example can be found in [119], where the authors addresses multi-fidelity modeling of interfacial load transfer for discontinuously reinforced polymer/carbon nano composites. The low fidelity model is chosen as a simple analytical technique whereas a 3D FE analysis is used as the high-fidelity approach. However, the multi-fidelity modeling approach can be used for more than two fidelity levels [113, 120, 121, 122]. Therefore the lower fidelity approaches do not necessarily represent an inaccurate approximation according to the definition given in [123], where it is defined as the model with outputs less accurate than the higher fidelity models. In the view of such information, the ODF, NNOCF and FE approaches can be defined using different fidelity levels. In high performance computing applications, such as optimization and UQ, the most appropriate fidelity level can be selected depending on the sensitivity of the design parameters by using the numerical techniques which are available for multi-fidelity analysis. The implementation of the multi-fidelity modeling strategy to the materials design problems will enable the use of higher order modeling techniques when they are actually needed as well as elimination of the redundant computations.

7.2 Multi-scale modeling of composite materials

The multi-scale modeling methodology presented in this study focuses on applications for metals and metallic alloys. However, an important future direction should include the extension of the same computational scheme to the modeling of composite materials. The multi-scale modeling and optimization starting from the microstructural features allows the control of macro engineering material properties. It can lead to design of engineering structures having heterogeneous material parameters depending on the application and performance needs. This concept also works in harmony with the new generation additive manufacturing techniques. Considering the growing application areas of the composite materials there is a definite need for implementing the multi-scale modeling methodology for their design. The same probabilistic descriptor based modeling approach can also be extended to the smaller length scales such as molecular or atomistic level. This will enable the design of nano-composites and multi-functional materials through optimization of the atomistic structure. An example of the equivalence of our approach for nano-composites is shown in Fig. 7.6.

Even though the multi-scale modeling of polymer and epoxy-based composites has been studied in literature [124, 125, 126, 127, 128, 129, 130] using different numerical techniques, a design methodology, that is similar to the one presented in this study, has not been integrated to improve the material performance for engineering applications. The implementation of this multi-scale optimization approach to composite materials design will enhance the structural performance of many aerospace applications.

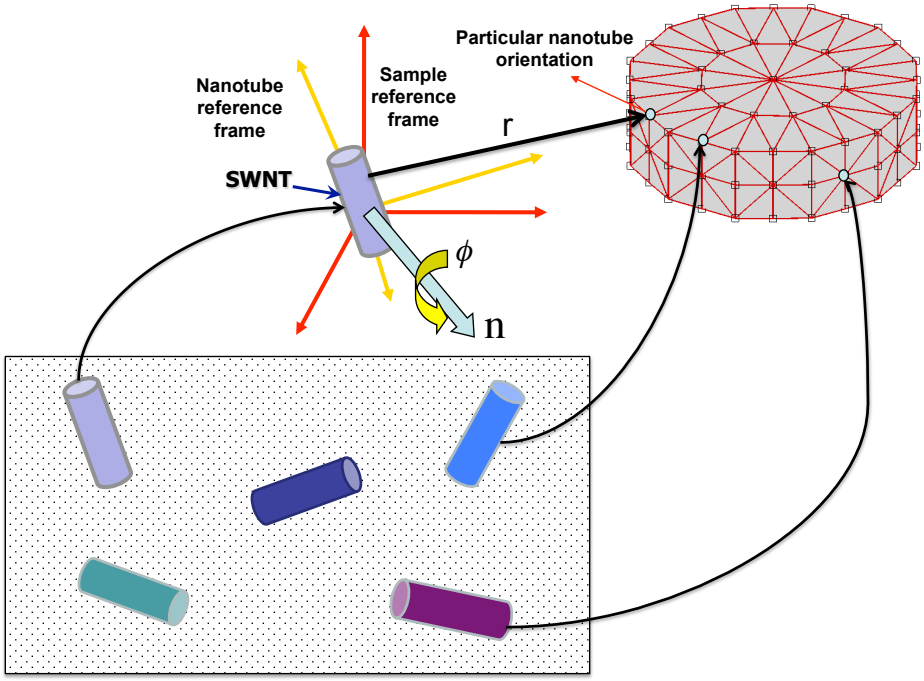

Figure 7.6: Multi-scale design of nano-composites

BIBLIOGRAPHY

[1] Ashby, M. F., Materials Selection in Mechanical Design, Pergamon, Tarrytown, NY, 1992.

[2] Fast, T., Knezevic, M. and Kalidindi, S. R., Application of microstructure sensitive design to structural components produced from hexagonal polycrystalline metals, *Computational Materials Science*. Vol. 43, No. 2, pp: 374–383, 2008.

[3] Kalidindi, S. R., Houskamp, J. R., Lyons, M. and Adams, B. L., Microstructure sensitive design of an orthotropic plate subjected to tensile load, *International Journal of Plasticity*, Vol. 20, No. 8-9, pp: 1561-1575, 2004.

[4] Olson, G. B., Computational Design of Hierarchically Structured Materials, *Science*, Vol. 277, No. 5330, pp:1237-1242, 1997.

[5] Sigmund, O., Torquato, S., Composites with extremal thermal expansion coefficients, *Applied Physics Letters*, Vol. 69, pp: 3203-3205, 1996.

[6] Lakes, R., Deformations in Extreme Matter, *Science*, Vol. 288, No. 5473, pp: 1976-1977, 2000.

[7] Bunge, H. J., Texture Analysis in Materials Science, Butterworths, London, 1982.

[8] Kocks, U. F., Tome, C. N., and Wenk, H. R., Texture and Anisotropy, Cambridge University Press, Cambridge, England, UK, 2000.

[9] Heinz, A. and Neumann, P., Representation of Orientation and Disorientation Data for Cubic, Hexagonal, Tetragonal and Orthorhombic Crystals, *Acta Crystallographica*, A47, pp: 780-789, 1991.

[10] Adams, B. L., Henrie, A., Henrie, B., Lyon, M., Kalidindi, S. R., and Garmestani H., Microstructure-Sensitive Design of a Compliant Beam, *Journal of Mechanics and Physics of Solids*, Vol. 49, No. 8, pp: 1639-1663, 2001.

[11] Kalidindi, S. R., Houskamp, J., Lyons, M., and Adams, B. L., Microstructure Sensitive Design of an Orthotropic Plate Subjected to Tensile Load, *International Journal of Plasticity*, Vol. 20, pp: 1561-1575, 2004.

[12] Kumar A., and Dawson P. R., Computational Modeling of F.C.C. Deformation Textures over Rodrigues' Space, *Acta Materialia*, Vol. 48, No. 10, pp: 2719-2736, 2000.

[13] Kumar A., and Dawson P. R., Modeling Crystallographic Texture Evolution with Finite Elements over Neo-Eulerian Orientation Spaces, *Computational Methods in Applied Mechanics and Engineering*, Vol. 153, No. 3-4, pp: 259-302, 2000.

[14] R. Liu, A. Kumar, Z. Chen, A. Agrawal, V. Sundararaghavan and A. Choudhary, A predictive machine learning approach for microstructure optimization and materials design, *Nature Scientific Reports*, 5 (11551), 2015.

[15] Fast, T., Knezevic, M., and Kalidindi, S. R., Application of microstructure sensitive design to structural components produced from hexagonal polycrystalline metals, *Computational Materials Science*, Vol. 43, No. 2, pp: 374-383, 2008.

[16] Acar, P., and Sundararaghavan, V., Utilization of a Linear Solver for Multiscale Design and Optimization of Microstructures, *AIAA Journal*, Vol. 54, No. 5, pp: 1751–1759, 2016.

[17] Anand, L. and Kothari, M., A computational procedure for rate-independent crystal plasticity, *Journal of the Mechanics and Physics of Solids*, Vol. 44, pp: 525–558, 1996.

[18] Li, D. S., Garmestani, H., and Adams, B. L., A texture evolution model in cubic-orthotropic polycrystalline system, *International Journal of Plasticity*, Vol. 21, No. 8, pp: 1591-1617, 2005.

[19] Sundararaghavan, V. and Zabaras, N., A dynamic material library for the representation of single phase polyhedral microstructures, *Acta Materialia*, Vol. 52, No. 14, pp: 4111-4119, 2004.

[20] Acar, P. and Sundararaghavan, V., A linear solution scheme for microstructure design with process constraints, *AIAA Journal*, Vol. 54, No. 12, pp: 4022-4031, 2016.

[21] Allison, J., Backman, D., and Christodoulou, L., Integrated Computational Materials Engineering: A New Paradigm for the Global Materials Profession, *Journal of the Minerals, Metals and Materials Society*, Vol. 58, No. 11, pp: 25–27, 2006.

[22] Panchal, J. H., Kalidindi, S. R. and McDowell, D. L., Key computational modeling issues in Integrated Computational Materials Engineering, *Computer-Aided Design*, Vol. 45, pp: 4-25, 2013.

[23] Chernatynskiy, A., Phillpot, S. R. and LeSar, R., Uncertainty Quantification in Multiscale Simulation of Materials: A Prospective, *Annual Review of Materials Research*, Vol. 43, pp:157-182, 2013.

[24] Creuziger, A., Syed, K. and Gnaupel-Herold, T., Measurement of uncertainty in orientation distribution function calculations, *Scripta Materialia*, Vol. 72-73, pp: 55–58, 2014.

[25] Juan, L., Liu, G., Wang, H. and Ullah, A., On the sampling of three-dimensional polycrystalline microstructures for distribution determination, *Journal of Microscopy*, Vol. 44, No. 2, pp: 214–222, 2011.

[26] Hiriyur, B., Waisman, H. and Deodatis, G., Uncertainty quantification in homogenization of heterogeneous microstructures modeled by XFEM, *International Journal for Numerical Methods in Engineering*, Vol. 88, No. 3, pp: 257–278, 2011.

[27] Savvas, D. and Stefanou, G., Assessment of the effect of microstructural uncertainty on the macroscopic properties of random composite materials, *Journal of Composite Materials*, in press, pp: 1-19, 2016.

[28] Kouchmeshky, B. and Zabaras, N., The effect of multiple sources of uncertainty on the convex hull of material properties of polycrystals, *Computational Materials Science*, Vol. 47, No. 2, pp: 342–352, 2009.

[29] Kouchmeshky, B. and Zabaras, N., Microstructure model reduction and uncertainty quantification in multiscale deformation processes, *Computational Materials Science*, Vol. 48, pp: 213-227, 2010.

[30] Madrid, P. J., Sulsky, D. and Lebensohn, R. A., Uncertainty Quantification in Prediction of the In-Plane Young's Modulus of Thin Films With Fiber Texture, *Journal of Microelectromechanical Systems*, Vol. 23, No. 2, pp: 380–390, 2014.

[31] Niezgoda, S. R., Yabansu, Y. and Kalidindi, S. R., Understanding and visualizing microstructure and microstructure variance as a stochastic process, *Acta Materialia*, Vol. 59, No. 16, pp: 6387–6400, 2011.

[32] Cai, G. and Mahadevan, S., Uncertainty Quantification of Manufacturing Process Effects on Macroscale Material Properties, *International Journal for Multiscale Computational Engineering*, Vol. 14, No. 3, pp: 191-213, 2016.

[33] Huyse, L. and Maes, M. A., Random Field Modeling of Elastic Properties Using Homogenization, *Journal of Engineering Mechanics*, Vol. 127, No. 1, pp: 27–36, 2001.

[34] Sakata, S., Ashida, F., Kojima, T. and Zako, M., Three-dimensional stochastic analysis using a perturbation-based homogenization method for elastic properties of composite material considering microscopic uncertainty, *International Journal of Solids and Structures*, Vol. 45, pp: 894–907, 2008.

[35] Sakata, S., Ashida, F. and Zako, M., Kriging-based approximate stochastic homogenization analysis for composite materials, *Computer methods in applied mechanics and engineering*, Vol. 197, pp: 1953–1964, 2008.

[36] Clement, A., Soize, C. and Yvonnet, J., Computational nonlinear stochastic homogenization using a nonconcurrent multiscale approach for hyperelastic heterogenous microstructure analysis, *International Journal for Numerical Methods in Engineering*, Vol. 91, pp: 799–824, 2012.

[37] Clement, A., Soize, C. and Yvonnet, J., Uncertainty quantification in computational stochastic multi-scale analysis of nonlinear elastic materials, *Computer Methods in Applied Mechanics and Engineering*, Vol. 254, pp: 61–82, 2013.

[38] Acar, P. and Sundararaghavan, V., Uncertainty Quantification of Microstructural Properties due to Variability in Measured Pole Figures, *Acta Materialia*, Vol. 124, pp: 100–108, 2017.

[39] Acar, P., Srivastava, S., and Sundararaghavan, V., Stochastic Design Optimization of Microstructures with Utilization of a Linear Solver, *AIAA Journal*, in press, 2017.

[40] Acar, P. and Sundararaghavan, V., Uncertainty Quantification of Microstructural Properties due to Experimental Variations, *AIAA Journal*, in press, 2017.

[41] Galan-Lopez, J., Naghdy, S., Verleysen, P., Kestens, L. A. I., Coghe, F., Rabet, L. and Degrieck, J., Mechanical behavior and texture prediction of Ti-6Al-4V based on elastic viscoplastic self-consistent modelling, *IOP Conf. Series: Materials Science and Engineering*, Vol. 82, 012027, 2015.

[42] Wu, Z.-H., Kou, H.-C., Tang, B., Shao, J., Han, F.-B. and Li, J.-S., Crystal Plasticity Finite-element Simulation of Ti-6Al-4V Alloy with 3D Polycrystalline Models, *2nd Annual International Conference on Advanced Material Engineering (AME 2016)*.

[43] Thomas, J., Groeber, M. and Ghosh, S., Image-based crystal plasticity FE framework for microstructure dependent properties of Ti-6Al-4V alloys, *Materials Science and Engineering A*, Vol. 553, pp: 164-175, 2012.

[44] Nervo, L., King, A., Fitzner, A., Ludwig, W. and Preuss, M., A study of deformation twinning in a titanium alloy by X-ray diffraction contrast tomography, *Acta Materialia*, Vol. 105, pp: 417-428, 2016.

[45] Balasubramanian, S., Application to Deformation Processing of Lightweight Metals, PhD Dissertation, Massachusetts Institute of Technology, February 1998.

[46] Williams, J. C., Baggerly, R. G. and Paton, N. E., Deformation Behavior of HCP Ti-Al Alloy Single Crystals, *Metallurgical and Materials Transactions A*, Vol. 33, No. 3, 837, 2002.

[47] Lienert, U., Brandes, M. C., Bernier, J. V., Weiss, J., Shastri, S. V., Mills, M. J. and Miller, M. P., In-situ single-grain peak profile measurements on Ti-7Al during tensile deformation, *Materials Science and Engineering: A*, Vol. 524, No. 1-2, pp: 46-54, 2009.

[48] Lutjering, G. and Williams, J., Introduction, in: Titanium, Second Ed., Springer, 2007.

[49] Paton, N. E., Baggerly, R. G. and Williams, J. C., Rockwell International. AFOSR Final Report, 1976. in: Khan, A. S., Kazmia, R., Farrokha, B. and Zupana, M., *International Journal of Plasticity*, Vol. 23, pp: 1105-1125, 2007.

[50] Fitzner, A. G., Effects of Alloying Elements on Twinning in alpha-Titanium Alloys, PhD Dissertation, University of Manchester, 2014.

[51] Fitzner, A. G., Prakash, D. G. L., Fonseca, J. Q., Thomas, M., Zhang, S., Kelleher, J., Manuel, P., Preuss, M., The effect of aluminum on twinning in binary alpha-Titanium, *Acta Materialia*, Vol. 103, pp: 341-351, 2016.

[52] Sha, W. and Malinov, S., Titanium alloys: modelling of microstructure, properties and applications, Elsevier, 2009.

[53] Deb, K., Pratap, A., Agarwal, S. and Meyarivan, T., A Fast Elitist Multiobjective Genetic Algorithm: NSGA-II, *IEEE Transactions on Evolutionary Computation*, Vol. 6, No. 2, pp: 182-197, 2002.

[54] Rigoni E., and Turco, A., Metamodels for fast Multi-Objective Optimization: Trading Off Global Exploration and Local Exploitation, *Proceedings of the SEAL 2010 LNCS 6457*, pp: 523-532, Kanpur, India, 2010.

[55] Salem, A. A., Kalidindi, S. R. and Semiatin, S. L., Strain hardening due to deformation twinning in α-titanium: Constitutive relations and crystal-plasticity modeling, *Acta Materialia*, Vol.53, No.12, pp: 3495-3502, 2005.

[56] McKay, M. D., Beckman, R. J. and Conover, W.J., A comparison of three methods for selecting values of input variables in the analysis of output from a computer code, *Technometrics*, Vol. 21, No. 2, pp: 239–245, 1979.

[57] Shahba, A. and Ghosh, S., Crystal plasticity FE modeling of Ti alloys for a range

of strain-rates. Part I: A unified constitutive model and flow rule, *International Journal of Plasticity*, Vol. 87, pp: 48–68, 2016.

[58] Timoshenko, S. P. and Gere, J. M., Theory of Elastic Stability, 2nd ed.,McGraw Hill, New York, 1961.

[59] Lopatin, A. V. and Korbut, Y. B., Buckling of Clamped Orthotropic Plate in Shear, Composite Structures, Vol. 76, No. 1-2, pp: 94-98, 2006.

[60] Lekhnitskii, S. G., Anisotropic Plates, Gordon and Breach Science Publishers, New York, 1968.

[61] Lin, C.-H., Lin. P.-L., A New Non-dominated Sorting Genetic Algorithm for Multi-Objective Optimization, *Modeling Simulation and Optimization - Focus on Applications*, Shkelzen Cakaj (Ed.), ISBN: 978-953-307-055-1, InTech, DOI: 10.5772/8961, 2010.

[62] Cheng, L. M., Nolting, A. E., Voyzelle, B. and Galvani, C., Deformation behavior of polycrystalline Galfenol at elevated temperatures, *Behavior and Mechanics of Multifunctional and Composite Materials*, Edited by Dapino, Marcelo J.. Proceedings of the SPIE, Volume 6526, pp. 65262N, 2007.

[63] Atulasimha, J., Flatau, A. B. and Summers, E., Characterization and energy-based model of the magnetomechanical behavior of polycrystalline irongallium alloys, *Smart Materials and Structures*, Vol. 16, pp: 1265-1276, 2007.

[64] Sundararaghavan, V. and Zabaras, N., Design of microstructure-sensitive properties in elasto-viscoplastic polycrystals using multi-scale homogenization, *International Journal of Plasticity*, Vol. 22, pp: 1799-1824, 2006.

[65] Sundararaghavan, V., Multiscale modeling of polycrystalline magnetostrictive

alloy Galfenol: Microstructural model, *1st World Congress on Integrated Computational Materials Engineering*, TMS 2011.

[66] Kumar, A. and Sundararaghavan, V., Simulation of magnetostrictive properties of Galfenol under thermomechanical deformation, *Finite Elements in Analysis and Design*, Vol. 127, pp: 1-5, 2017.

[67] Chantrasmi, T., Constantine, P., Etemadi, N., Iaccarino, G. and Wang, Q., Uncertainty quantification in simple linear and non-linear problems, *Center for Turbulence Research Annual Research Briefs*, 1:3 -16, 2006.

[68] Barton, N. R., Boyce, D. E. and Dawson, P. R., Pole figure inversion using finite elements over rodrigues space, *Textures and Microstructures*, Vol. 35, No. 2, pp: 113-144, 2002.

[69] Wilk, M. B. and Gnanadesikan, R., Probability plotting methods for the analysis of data, *Biometrika*, Vol. 55, No. 1, pp: 1–17, 1968.

[70] Gut, A., An Intermediate Course in Probability, Springer New York, 2009.

[71] Ross, S. M., Introduction to Probability Models: 10th Edition, *Elsevier*, 2010.

[72] Simmons, G. and Wang, H., Single Crystal Elastic Constants and Calculated Aggregate Properties, The M.I.T Press, 1971.

[73] Sundararaghavan, V. and Zabaras, N., A multi-length scale continuum sensitivity analysis for the control of texture-dependent properties in deformation processing, *International Journal of Plasticity*, Vol. 24, pp: 1581–1605, 2008.

[74] Nadarajah, S., A Review of Results on Sums of Random Variables, *Acta Applicandae Mathematicae*, Vol. 103, pp: 131-140, 2008.

[75] Alouini, M. S., Abdi, A. and Kaveh, M., Sum of gamma variates and performance of wireless communications systems over Nakagami fading channels, *IEEE Transactions on Vehicular Technology*, Vol. 50, pp: 1471-1480, 2001.

[76] Sundararaghavan, V. and Zabaras, N., Linear analysis of texture-property relationships using process-based representations of Rodrigues space, *Acta Materialia*, Vol. 55, pp: 1573-1587, 2007.

[77] Acar, P. and Sundararaghavan, V., Utilization of a Linear Solver for Multiscale Design and Optimization of Microstructures in an Airframe Panel Buckling Problem, *57th AIAA/ASCE/AHS/ASC Structures, Structural Dynamics, and Materials Conference*, 4-8 January 2016, San Diego, CA, USA.

[78] Acherjee, S., and Zabaras, N., A proper orthogonal decomposition approach to microstructure model reduction in Rodrigues space with applications to optimal control of microstructure-sensitive properties, *Acta Materialia*, Vol. 51, No. 18, pp: 5627-5646, 2003.

[79] Ganapathysubramanian, S., and Zabaras, N., Design across length scales: a reduced-order model of polycrystal plasticity for the control of microstructure-sensitive material properties, *Computer methods in applied mechanics and engineering*, Vol. 193, pp: 5017-5034, 2004.

[80] Sundararaghavan, V., and Zabaras, N., On the synergy between texture classification and deformation process sequence selection for the control of texture-dependent properties, *Acta Materialia*, Vol. 53, No. 4, pp: 1015-1027, 2005.

[81] Taylor, G., Plastic strain in metals, *Journal of the Institute for Metals*, Vol. 62, pp: 307–324, 1938.

[82] Asaro, R. J. and Needleman, A., Texture development and strain hardening in rate dependent polycrystals, *Acta Metallurgica*, Vol. 33, pp: 923–953, 1985.

[83] Canova, G. R., Kocks, U. F. and Jonas, J. J., Theory of torsion texture development, *Acta Metallurgica*, Vol. 32, No. 2, pp: 211–226, 1984.

[84] Molinari, A., Canova, G. R. and Ahzi, S., A self consistent approach of the large deformation polycrystal viscoplasticity, *Acta Metallurgica*, Vol. 35, No. 12, pp: 2983–2994, 1987.

[85] Tiem, S., Berveiller, M. and Canova, G. R., Grain shape effects on the slip system activity and on the lattice rotations, *Acta Metallurgica*, Vol. 34, No. 11, pp: 2139–2149, 1986.

[86] Sundararaghavan, V. and Zabaras, N., Classification and reconstruction of three-dimensional microstructures using support vector machines, *Computational Materials Science*, Vol. 32, No. 2, pp: 223-239, 2005.

[87] Acar, P. and Sundararaghavan, V., A Markov Random Field Approach for Modeling Spatio-Temporal Evolution of Microstructures, *Modelling and Simulation in Materials Science and Engineering*, 24, 075005 (15pp), 2016.

[88] Sundararaghavan, V., Reconstruction of three-dimensional anisotropic microstructures from two-dimensional micrographs imaged on orthogonal planes, *Integrating Materials and Manufacturing Innovation*, 3:19, pp: 1–11, 2014.

[89] Kumar, A., Sundararaghavan, V., De Graef, M. and Nguyen, L., A Markov Random Field Approach for Microstructure Synthesis, *Modelling Simul. Mater. Sci. Eng.*, 24 pp: 035015 (1-13), 2016.

[90] Sun, S. and Sundararaghavan, V., A probabilistic crystal plasticity model for modeling grain shape effects based on slip geometry, *Acta Materialia*, Vol .60, No. 13-14, pp: 5233–5244, 2012.

[91] Corson, P. B., Correlation functions for predicting properties of heterogeneous materials. II. Empirical construction of spatial correlation functions for two phase solids, *Journal of Applied Physics*, Vol. 45, pp: 3165-3170, 1976.

[92] Adams, B. L., Ahzi, S., Garmestani, H. and Lin, S., Statistical continuum theory for large plastic deformation of polycrystalline materials, *Journal of the Mechanics and Physics of Solids*, Vol. 49, pp: 589-607, 2001.

[93] Adams, B. L., Gao, X. and Kalidindi, S. R., Finite approximations to the second-order properties closure in single phase polycrystals, *Acta Materialia*, Vol. 53, pp: 3563-3577, 2005.

[94] Sundararaghavan, V., and Kumar, A., Probabilistic modeling of microstructure evolution using finite element representation of statistical correlation functions, *International Journal of Plasticity*, Vol. 30, pp: 62-80, 2012.

[95] Adams, B. L., Canova, G. R. and Molinari, A., A statistical formulation of viscoplastic behavior in heterogeneous polycrystals, *Textures and Microstructures*, Vol. 11, pp: 57-71, 1989.

[96] Paulson, N. H., Priddy, M. W., McDowell, D. L. and Kalidindi, S. R., Reduced-order structure-property linkages for polycrystalline microstructures based on 2-point statistics, *Acta Materialia*, Vol. 129, pp: 428–438, 2017.

[97] Yabansu, Y. C., Steinmetz, P., Hotter, J. and Kalidindi, S. R., Extraction of reduced-order process-structure linkages from phase-field simulations, *Acta Materialia*, Vol. 124, pp: 182–194, 2017.

[98] Dotsenko, A., Introduction to LENS Additive Manufacturing, retrieved from: http://materials-informatics-class-fall2015.github.io/MIC-LENS/2015/09/24/Intro_LENS, on 7 June 2017.

[99] Sundararaghavan, V., Kumar, A. and Sun, S., Crystal plasticity simulations using nearest neighbor orientation correlation function, *Acta Materialia*, Vol. 93, pp: 12–23, 2015

[100] Sun, S. and Sundararaghavan, V., A peridynamic implementation of crystal plasticity, *International Journal of Solids and Structures*, Vol. 51, pp: 3350–3360, 2014.

[101] Zabaras, N., Sundararaghavan, V. and Sankaran, S., An information theoretic approach for obtaining property PDFs from macro specifications of microstructural uncertainty *TMS Letters*, Vol 3 , No. 1, pp :1–3, 2006.

[102] Sundararaghavan V. and Zabaras, N., A statistical learning approach for the design of polycrystalline materials, *Statistical Analysis and Data Mining*, Vol. 1, No. 5, pp: 306–321, 2009.

[103] Mandel, J., Generalization de la theorie de la plasticite de W.T. Koiter, *International Journal for Solids and Structures*, Vol. 1, pp: 273–295, 1965.

[104] Rice, J. R., Inelastic constitutive relations for solids: an internal variable theory and its application to metal plasticity, *Journal of Mechanics and Physics of Solids*, Vol. 19, pp: 433–455, 1971.

[105] Mandel, J., Plasticite Classique et Viscoplasticite. *CISM Courses and Lectures* No. 97, Springer, Berlin, 1972.

[106] Hill, R., Continuum micro-mechanics of elastoplastic polycrystals, *Journal of Mechanics and Physics of Solids*, Vol. 13, pp: 89–101, 1965.

[107] Teodosiu, C. and Sidoroff, F., A theory of finite elastoviscoplasticity of single crystals, *International Journal of Engineering Sciences*, Vol. 14, pp: 165–176, 1976.

[108] Asaro, R. J., Micromechanics of Crystals and Polycrystals, *Advances in Applied Mechanics*, Vol. 23, pp: 1–115, 1983.

[109] Bronkhorst, C. A., Kalidindi, S. R. and Anand, L., Polycrystalline plasticity and the evolution of crystallographic texture in FCC metals, *Philosophical Transactions of the Royal Society of London A*, Vol. 341, pp: 443–477, 1992.

[110] Cuitino, A. M. and Ortiz, M., Computational modeling of single crystals, *Modelling and Simulation in Material Science and Engineering*, Vol. 1, pp: 225–263, 1992.

[111] Castro, J. P. J., Gray, G. A., Hough, P. D., and Giunta, A. A., Developing a computationally efficient dynamic multilevel hybrid optimization scheme using multifidelity model interactions, Technical report, SAND2005-7498, Sandia National Laboratories. Albuquerque, NM, 2005.

[112] Keane, A. J., Cokriging for robust design optimization, *AIAA Journal*, Vol. 50, No. 1, pp: 2351-2364, 2012.

[113] Forrester, A. I., Black-box calibration for complex-system simulation, *Philosophical Transactions of the Royal Society of London A: Mathematical, Physical and Engineering Sciences*, Vol. 368, No. 1924, pp: 3567-3579, 2010.

[114] Sharma, A., Gogu, C., Martinez, O. A., Sankar, B. V., and Haftka, R. T., Multi-fidelity design of an integrated thermal protection system for spacecraft reentry, *49th AIAA/ASME/ASCE/AHS/ASC Structures, Structural Dynamics, and Materials Conference*, Schauroburg, Illinois, USA, 2008.

[115] Venkataraman, S., Reliability optimization using probabilistic sufficiency factor and correction response surface, *Engineering Optimization*, Vol. 38, No. 6, pp: 671-685, 2006.

[116] Venkataraman, S., Haftka, R., and Johnson, T., Design of shell structures for buckling using correction response surface approximations, *7th AIAA/USAF/NASA/ISSMO Symposium on Multidisciplinary Analysis and Optimization*, St. Louis, MO, USA, 1998.

[117] Goldfeld, Y., Vervenne, K., Arbocz, J., and Van Keulen, F., Multi-fidelity optimization of laminated conical shells for buckling, *Structural and Multidisciplinary Optimization*, Vol. 30, No. 2, pp: 128-141, 2005.

[118] Fernandez-Godino, M. G., Park, C., Kim, N.-H., and Haftka, R. T., Review of multi-fidelity models, arXiv preprint arXiv:1609.07196, 2016.

[119] Kopp, R., Gardea, F., Glaz, B., and Smith, E. C., Multi-fidelity Modeling of Interfacial Micromechanics for Off-Aligned Polymer/Carbon Nanotube Nanocomposites, *58th AIAA/ASCE/AHS/ASC Structures, Structural Dynamics, and Materials Conference*, Grapevine, TX, USA, 2017.

[120] Huang, D., Allen, T., Notz, W., and Miller, R., Sequential kriging optimization using multiple-fidelity evaluations, *Structural and Multidisciplinary Optimization*, Vol. 32, No. 5, pp: 369-382, 2006.

[121] Le Gratiet, L., Bayesian analysis of hierarchical multifidelity codes, *SIAM/ASA Journal on Uncertainty Quantification*, Vol. 1, No. 1, pp: 244-269, 2013.

[122] Goh, J., Bingham, D., Holloway, J. P., Grosskopf, M. J., Kuranz, C. C., and Rutter, E., Prediction and computer model calibration using outputs from multifidelity simulators, *Technometrics*, Vol. 55, No. 4, pp: 501-512, 2013.

[123] Peherstorfer, B., Willcox, K., and Gunzburger, M., Survey of multifidelity methods in uncertainty propagation, inference, and optimization, ACDL Technical Report TR16-1, 2016.

[124] Zeng, Q. H., Yu, A. B. and Lu, G. Q., Multiscale modeling and simulation of polymer nanocomposites, *Progress in Polymer Science* , Vol. 33, pp: 191-269, 2008.

[125] Yu, S., Yang, S. and Cho, M., Multi-scale modeling of cross-linked epoxy nanocomposites, *Polymer*, Vol. 50, pp: 945-952, 2009.

[126] Fasanella, N. and Sundararaghavan, V., Atomistic Modeling of Thermal Conductivity of Epoxy Nanotube Composites, *JOM*, Vol. 68, No. 5, pp: 1396-1410, 2016.

[127] Fasanella, N. and Sundararaghavan, V., Atomistic modeling of thermomechanical properties of SWNT/Epoxy nanocomposites, *Modelling and Simulation in Materials Science*, 23, 065003 (16pp), 2015.

[128] Reddy, B. R. and Ramji, K., Modeling and Simulation of Nano and Multiscale Composites, *International Journal of Hybrid Information Technology*, Vol. 9, No. 3, pp: 133-144, 2016.

[129] Kumar, A. and Sundararaghavan, V., Molecular dynamics simulations of compressive yielding in cross-linked epoxies in the context of Argon theory,*International Journal of Plasticity*, Vol. 47, pp: 111–125, 2013.

[130] Kumar, A. and Sundararaghavan, V. and Browning, A. R., Study of temperature dependence of thermal conductivity in cross-linked epoxies using molecular dynamics simulations with long range interactions, *Modelling and Simulation in Materials Science and Engineering*, Vol. 22, No. 2, 025013, pp: 1-15, 2014.